A COMPUTATIONALLY EFFICIENT MODELLING OF LAMINAR SEPARATION BUBBLES

FINAL REPORT
for
NASA Grant NAG-1-778

Paolo Dini and Mark D. Maughmer

Department of Aerospace Engineering
The Pennsylvania State University
233 Hammond Building
University Park, PA 16802

July 1990

ABSTRACT

In predicting the aerodynamic characteristics of airfoils operating at low Reynolds numbers, it is often important to account for the effects of laminar (transitional) separation bubbles. Previous approaches to the modelling of this viscous phenomenon range from fast but sometimes unreliable empirical correlations for the length of the bubble and the associated increase in momentum thickness, to more accurate but significantly slower displacement-thickness iteration methods employing inverse boundary-layer formulations in the separated regions. Since the penalty in computational time associated with the more general methods is unacceptable for airfoil design applications, use of an accurate yet computationally efficient model is highly desirable. To this end, a semi-empirical bubble model has been developed and incorporated into the Eppler and Somers airfoil design and analysis program. The generality and the efficiency have been achieved by successfully approximating the local viscous/inviscid interaction, the transition location, and the turbulent reattachment process within the framework of an integral boundary-layer method. Comparisons of the predicted aerodynamic characteristics with experimental measurements for several airfoils show excellent and consistent agreement for Reynolds numbers from 2,000,000 down to 100,000.

TABLE OF CONTENTS

LIST OF FIGURES

Page

Page

Page

Page

LIST OF SYMBOLS

b	width of separated shear layer
c	airfoil chord
c_d	section drag coefficient
c_f	skin-friction coefficient
c_ℓ	section lift coefficient
c_m	section moment coefficient about quarter-chord point
f	disturbance frequency in Hertz
h	distance of separated shear layer from airfoil surface
h_T	height of dividing streamline at transition
ℓ_1	laminar length of the bubble
ℓ_2	turbulent length of the bubble
m	exponent of velocity distribution power law for Falkner-Skan flows
n	linear stability theory amplification factor, $\ln\left(\frac{A}{A_0}\right)$
p	static pressure
r	decay rate of dissipation coefficient function downstream of reattachment
s	streamwise coordinate from the stagnation point
u	streamwise velocity inside the boundary layer
u_1	streamwise velocity above turbulent shear layer
u_2	streamwise velocity below turbulent shear layer
u'	streamwise fluctuating velocity
u_*	friction velocity, $\sqrt{\frac{\tau_w}{\rho}}$
$-\rho\overline{u'v'}$	turbulent Reynolds stress
v'	normal fluctuating velocity
$\hat{v}$	amplitude of fluctuating velocity

x	distance along airfoil chord
y	normal distance from the surface
A_0	disturbance amplitude at neutral stability
A_1	amplitude of turbulent H_{32}-distribution upstream of reattachment
A_2	amplitude of turbulent H_{32}-distribution downstream of reattachment
B	van Ingen's separation angle constant, $= 17.5$
C_D	dissipation coefficient, $\frac{1}{1/2\rho U^3}\int_0^\infty (\mu\frac{\partial u}{\partial y} - \rho\overline{u'v'})\frac{\partial u}{\partial y}dy$
C_p	pressure coefficient, $\frac{p-p_\infty}{1/2\rho U^2}$
C_τ	maximum turbulent shear stress coefficient, $\frac{(-\overline{u'v'})_{max}}{U^2}$
DU	inviscid velocity decrease as $\ell_1 \rightarrow \infty$
F	reduced frequency, $\frac{2\pi f\nu}{U^2}$
G	amplitude of Coles's wake function in Green's profiles
G_t	turbulent modified shape parameter
H_{12}	boundary-layer shape factor, $\frac{\delta_1}{\delta_2}$
H_{32}	boundary-layer shape factor, $\frac{\delta_3}{\delta_2}$
P	Gaster's pressure gradient parameter, $\frac{(\delta_2)_S^2}{\nu}\frac{\Delta U}{\Delta s}$
R	chord Reynolds number, $\frac{U_\infty c}{\nu}$
R_{ℓ_1}	laminar length Reynolds number, $\frac{U_S \ell_1}{\nu}$
R_{δ_2}	momentum thickness Reynolds number, $\frac{U\delta_2}{\nu}$
SF	scaling factor to match curvature of H_{32}-distribution at reattachment
Tu	turbulence intensity
U	velocity at the edge of the boundary layer/inviscid velocity
U_∞	freestream velocity
α	angle of attack relative to the chord line
α^*	wavenumber of sinusoidal disturbance
β	Falkner-Skan laminar pressure gradient parameter, $\frac{\xi_{FS}^2}{\nu}\frac{dU}{ds}$

β_t	Clauser turbulent pressure gradient parameter, $\frac{\delta_1}{\tau_w}\frac{dp}{ds}$
γ	separation angle
δ	boundary-layer thickness
δ_1	boundary-layer displacement thickness, $\int_0^\infty \left(1-\frac{u}{U}\right) dy$
δ_2	boundary-layer momentum thickness, $\int_0^\infty \frac{u}{U}\left(1-\frac{u}{U}\right) dy$
δ_3	boundary-layer kinetic energy thickness, $\int_0^\infty \frac{u}{U}\left[1-\left(\frac{u}{U}\right)^2\right] dy$
θ	spreading angle of turbulent shear layer
λ	nondimensional velocity ratio of turbulent shear layer, $\frac{u_1-u_2}{u_1+u_2}$
μ	viscosity of air
ν	kinematic viscosity of air
ξ	dimensionless streamwise coordinate inside the bubble
ξ_{FS}	Falkner-Skan characteristic boundary-layer thickness
ρ	density of air
τ_w	wall shear stress
ω^*	radian frequency of sinusoidal disturbance
Δ	turbulent defect displacement thickness, $\int_0^\infty \frac{U-u}{u_*} dy$
$\Lambda_{\mathcal{R}}$	Horton's universal reattachment parameter, $\left(\frac{\delta_2}{U}\frac{dU}{ds}\right)_{\mathcal{R}}$

Subscripts:

∞	undisturbed flow condition
i	the imaginary part
r	the real part
$\mathcal{S}$	laminar separation point
$\mathcal{R}$	turbulent reattachment point
$\mathcal{T}$	transition point
TE	trailing edge

Chapter 1

INTRODUCTION

This thesis is concerned with a particular aspect of the overall task of estimating the aerodynamic performance of airfoils. Before a more precise statement of the problem can be made, it is necessary to describe its physical setting and to define some important terms.

Background and Definitions

The prediction of the aerodynamic performance of a two-dimensional airfoil can be obtained by letting the airfoil remain stationary while analyzing the flow of air over it. The speeds of interest here are usually sufficiently smaller than the local speed of sound of the air to justify an assumption of incompressible flow.

As the Reynolds number, defined as

$$R = \frac{U_\infty c}{\nu} \tag{1.1}$$

falls below approximately $R = 4 \times 10^6$, the laminar boundary layer may run out of momentum before transition on the surface occurs. Since the momentum of the outer flow cannot readily reach the stagnant fluid near the surface, the imposed adverse pressure gradient can only be balanced by a negative velocity of the flow. That is, the boundary layer separates leaving a thin region of reversed flow underneath it. In such cases, transition occurs in the free shear layer downstream of laminar separation and is usually followed by reattachment as a turbulent boundary layer, such that a small amount of fluid remains trapped between the shear layer and the surface. This pocket of fluid is called a laminar separation bubble.

Laminar separation bubbles on airfoils are observed over a large Reynolds number range. Due to the ability of the turbulent shear layer to reattach to the surface

of a streamlined shape such as an airfoil, the critical Reynolds number is approximately two orders of magnitude smaller than that at which laminar separation is first observed. In the flow over a circular cylinder, a large jump in drag coefficient is observed as the Reynolds number is decreased approximately below $R = 300,000$. At this value, in fact, the bubble cannot reattach immediately downstream of transition and massive laminar separation results. For airfoils, the critical Reynolds number depends on thickness and angle of attack but is usually between $R = 40,000$ and $200,000$. Unlike the case of a cylinder, a bubble that has burst due to a decrease in Reynolds number will usually reattach upstream of the trailing edge. In this state, it is called a long bubble and it causes a large decrease in lift and a large increase in drag. Bursting may also occur at high Reynolds numbers near the leading edge, downstream of the suction peak present on the upper surface at high angles of attack. The inability of the shear layer to reattach is ascribed in this case to the extreme values of the adverse pressure gradient.

In the first forty years since laminar separation bubbles were first observed by Melville Jones in 1933, leading-edge bubbles at high Reynolds numbers received most of the attention since their bursting is generally believed to be responsible for abrupt stall. In more recent years, the development of small remotely controlled aircraft (Remotely Piloted Vehicles) has shifted the Reynolds number range of interest to values below one million. In this range, due to the delayed transition, bubbles may form near the mid-chord causing significant increases in profile drag, depending on their length and thickness. The shift from leading-edge to mid-chord bubbles has been a fortunate one. Since the latter are usually an order of magnitude larger (although they appear to be very similar in internal flow structure), the greater ease of measuring pressure or flow variables has made it possible to make great progress toward full understanding of this phenomenon. This understanding,

however, is still not sufficient to establish a reliable bursting criterion.

Whether bursting occurs due to a decrease in Reynolds number or to an increase in pressure gradient, the resulting flowfield is characterized by a global strong interaction between the viscous and the inviscid regions and section properties cannot be obtained by means of simple approximations. Away from these limiting conditions, however, the viscous/inviscid interaction induced by the bubble is limited to its immediate vicinity, especially at low to moderate lift coefficients. Such bubbles have traditionally been called "short," although it may be more accurate to refer to them as "weakly interacting."

Problem Statement

The purpose of this study is to develop a model for weakly interacting laminar separation bubbles developing in the incompressible, two dimensional, viscous flow over airfoils that can accurately account for the increase in airfoil profile drag that accompanies them.

From the point of view of boundary-layer theory, the distinction between weak and strong viscous/inviscid interaction is made on the basis of the magnitude of the modification to the inviscid pressure distribution by the viscous flow. A weakly interacting bubble, therefore, is such only insofar as its effect on the *global* inviscid pressure distribution is concerned but is still characterized by a strong *local* interaction. In addition, when first confronted with the description of a region of recirculating flow between a separation and a reattachment point, it seems natural to assume that the flowfield is elliptic and that the boundary-layer approximations are not applicable. Given the very slow speeds of the recirculating flow and the thinness of the bubble, however, the boundary-layer approximations are usually assumed to be valid everywhere. Rather than within the recirculating flow, in fact, important signals are communicated upstream through the interaction with the

outer flow. A parabolic boundary-layer method is therefore adequate for analyzing laminar separation bubbles as long as it is coupled to the outer elliptic flow through at least a local interaction algorithm. This has been employed in the present model and, to maximize the computational efficiency, the boundary-layer development is calculated with an integral method.

In order to determine the increase in drag caused by a bubble, the shear layer development must be calculated through the different regions of the bubble as shown in Fig. 1-1. The formation of a bubble is initiated at point $\mathcal{S}$, shown in the figure, by the laminar boundary layer separating from the airfoil surface. Using integral boundary-layer methods, this point can be determined with sufficient accuracy for airfoil design work. Once separated, the free shear layer development must be tracked and the transition from laminar to turbulent flow, which occurs near the point $\mathcal{T}$, predicted. As shown in the figure, the separation bubble causes a plateau to form in the velocity distribution between the points corresponding to laminar separation and the end of the transition region. From this point, the turbulent part of the bubble encompasses a pressure recovery region which leads to the reattachment of the turbulent shear layer at point $\mathcal{R}$. As an additional pressure recovery always occurs downstream of a reattachment point [Green, 1966], the velocity distribution corresponding to the highly non-equilibrium, relaxing boundary layer downstream of reattachment usually "undershoots" the inviscid distribution. Eventually, the turbulent boundary layer reaches its fully developed state and the undershoot region merges smoothly from below with the inviscid velocity distribution. Clearly it is possible, especially at low Reynolds numbers, that the turbulent boundary layer does not reach equilibrium before the trailing edge of the airfoil.

Rather than describing the effect of the bubble on the pressure distribution, it is more informative to explain *why* such an effect is observed. This can be done

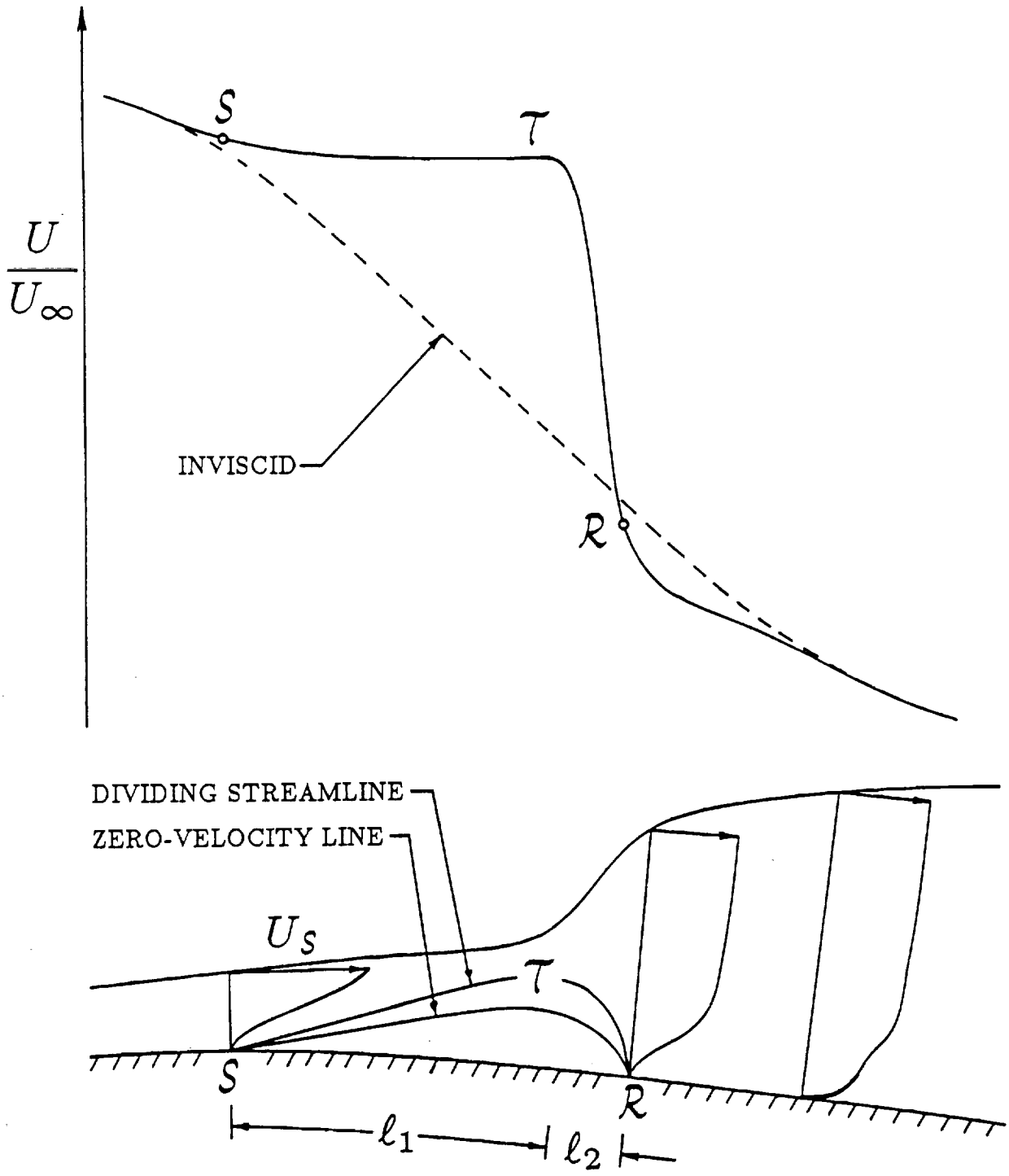

Fig. 1-1 Schematic of bubble and of its effect on the velocity distribution

by invoking two conservation laws, the conservation of mechanical energy and the conservation of linear momentum. In an inviscid incompressible flow, the conservation of mechanical energy is simply Bernoulli's equation. While inside the boundary layer the total pressure is continually and unevenly being dissipated by the shear stresses, static pressure rise is still achieved by trading for it the available kinetic energy inside the boundary layer. Once the boundary layer runs out of kinetic energy shortly downstream of separation, since conservation of energy is a scalar law and energy is a positive-definite quantity, no more pressure can be recovered. Conservation of linear momentum, on the other hand, is a vector law such that, once the boundary layer runs out of momentum, it has no difficulty allowing it to become negative to balance the imposed inviscid adverse pressure gradient. As soon as this happens, however, the presence of the reverse flow, felt by the outer flow as a modification of the airfoil surface, effectively decreases this same inviscid pressure gradient. As the pressure gradient decreases, it, in turn, induces a lesser growth of reverse flow. In the limit, a bounded growth of reverse flow at constant pressure results. This new distribution of static pressure matches what the energy equation allows.

While the momentum present in a laminar boundary layer is strictly dependent on what is "handed down" by the upstream development, the efficient cross-stream transfer of momentum by the Reynolds stresses that appear downstream of transition in the bubble brings the momentum of the outer flow near the wall. This allows the reverse flow to be accelerated and near-inviscid pressure to be recovered by the reattachment point. This loss of outer flow momentum is observed, by definition, as a rapid boundary-layer growth in the turbulent part of the bubble. Within the context of an integral method, the momentum lost by the flow results in the large growth in momentum thickness measured in this part of the bubble and can result

in a significant increase in airfoil drag.

Previous Models

Previous attempts at modelling this flow phenomenon range from very crude empirical correlations for the transition length from laminar separation and subsequent reattachment behavior to full simulations of the Reynolds-averaged turbulent Navier-Stokes equations. This variety of approaches is partly caused by the long time-span over which this problem has been studied. In the early years, several empirical models or empirical correlations for particular bubble characteristics were proposed. Von Doenhoff [1938] assumed that the dividing streamline is straight and tangent to the airfoil surface at the separation point. He determined the transition location by assuming a constant transition Reynolds number, formed with the velocity at separation and the distance between separation and transition along the dividing streamline. The distance to reattachment is then determined using a constant spreading angle of the turbulent shear layer of 15° measured from the direction of the dividing streamline. Interestingly, the present model resembles this initial configuration more than many others that have followed in the next fifty years. Crabtree [1957] proposed a coefficient of pressure rise in the turbulent part of the bubble equal to

$$\sigma = \frac{p_{\mathcal{R}} - p_{\mathcal{T}}}{(1/2)\rho U_{\mathcal{T}}^2} \tag{1.2}$$

This coefficient has been used mainly to monitor bubble bursting, which would happen for values of $\sigma > 0.35$. These early results, measurements, and hypotheses are discussed extensively in review papers by Ward [1963] and Tani [1964].

Gaster [1967] investigated bubble bursting with decreasing Reynolds number. He characterizes the bubble by the values of the momentum thickness Reynolds

number at separation,

$$(R_{\delta_2})_S = \frac{U_S(\delta_2)_S}{\nu} \tag{1.3}$$

and a pressure gradient parameter,

$$P = \frac{(\delta_2)_S^2}{\nu}\frac{\Delta U}{\Delta s} \tag{1.4}$$

where the velocity gradient in Gaster's parameter refers to the mean inviscid gradient between the separation and reattachment points. With varying conditions, for instance decreasing Reynolds number, a locus of points corresponding to the bubble evolution can be traced on a plot whose axes measure variations in these two parameters. He found that bursting would occur always along the same line on this plot. Although bursting is not modelled in this study, these same two parameters play a fundamental role in the present model. Horton [1967] proposed a semi-empirical model where the governing integral boundary-layer equations are coarsely approximated inside the bubble. This model will be discussed in more detail in Chapter 2. Van Ingen [1975] and Van Ingen et al. [1980, 1986] studied the bubble problem for many years. Their model is distinguished by a good approximation to the pressure distribution in the bubble region and of the transition process. The shear layer growth along the bubble, however, is not adequately approximated. These methods are usually not sufficiently accurate or general, their main shortcoming being an inability to account for the local ellipticity of the bubble flowfield.

Since approximately 1970, advances in computer technology have prompted a number of more detailed viscous simulations by finite-difference methods. Briley and McDonald [1975] developed a local Navier-Stokes solution for the bubble region which is matched with the steady boundary-layer equations upstream and downstream of the bubble and with the inviscid outer flow. Their predictions match Gault's [1955] measurements to an acceptable degree of accuracy but comparisons

with airfoil drag data are not given. Davis and Carter [1984] developed an interacting method based on a perturbation of the outer inviscid flow by a source distribution representing the bubble and a finite-difference boundary-layer method for the bubble flowfield and boundary layer. By properly accounting for the local flow direction, their method is able to resolve rather interesting details about the flow inside the bubble. For instance, there appear to be three different vortices: one in the laminar part, one in the turbulent part, and one in between, next to the wall and rotating in the opposite sense. While the bubble characteristics predicted by this method compare well with the experimental data presented in their report [Gault, 1955], low Reynolds number cases and the effect of the bubble on airfoil drag are not considered. Cebeci and Schimke [1983], Cebeci [1989], and Kwon and Pletcher [1979] follow similar formulations, where a finite-difference boundary-layer method interacts with the outer flow. These methods are limited by the generality of the turbulence model they employ and, for the present time, are much too inefficient computationally to be used routinely.

Over the same period of time, approaches that can be considered of an intermediate degree of complexity have flourished: interactive methods that use an integral formulation for the boundary-layer development. Crimi and Reeves [1976], Drela and Giles [1987], Drela [1989], and Gleyzes et al. [1983] are of this type. The advantage of such methods is that they combine a relative computational efficiency with a potential for sufficient accuracy and generality.

A Model for Airfoil Design

In the Reynolds number range over which laminar separation bubbles form, $40,000 < R < 4,000,000$, they assume many different sizes and thicknesses, each tied to a particular airfoil geometry or to particular conditions on different airfoils. In fact, many different types of aircraft with different mission requirements and

design constraints fly in this range. It often happens that particular airplane design goals conflict with flow conditions that would minimize the detrimental effects of bubbles. For instance, the low-drag requirement of sailplanes necessitates extensive use of natural laminar flow technology. The favorable pressure distribution to 50 or 60% of the chord generally employed on laminar flow airfoils necessarily leads to a steep pressure recovery over their aft-portion. The high performance of such airfoils hinges on forcing transition before the boundary layer encounters the adverse pressure gradient since the higher energy turbulent boundary layer is more able to recover the near-freestream trailing-edge pressure without separating. This is achieved by means of a region of moderately adverse pressure gradient, a "transition ramp," at the end of the favorable pressure gradient region. As the Reynolds number decreases, the transition ramp becomes insufficient to destabilize the laminar boundary layer into transition before the beginning of the recovery such that a thick, high-drag bubble forms. The trade-off, therefore, is between the advantages of natural laminar flow at cruise speeds and the disadvantages of the bubble in thermalling flight. The higher c_ℓ required for thermalling would at first sight seem to help the designer in avoiding the bubble. In fact, higher c_ℓ's are obtained at higher angles of attack such that the adverse pressure gradient starts near the leading edge. The destabilizing effect of this type of pressure distribution is offset, however, by the lower Reynolds numbers characteristic of this flight regime. Since small changes in the pressure distribution can effect large changes in bubble structure and, therefore, in drag, this "fine-tuning" engineering problem can be resolved only if the effects of the bubble can be accurately calculated under different types of pressure distributions at different Reynolds numbers.

One way of accounting for laminar separation bubbles in airfoil design is the bubble analog used in the design and analysis program of Eppler and Somers [1980].

The design method of this program uses an inverse conformal mapping method that allows great freedom and flexibility in specifying the characteristics of the airfoil pressure distribution to achieve the desired performance. The aerodynamic characteristics are calculated by an integral boundary-layer method driven by the inviscid velocity distribution. Close monitoring of the boundary-layer development is actively used in the design process to aid in the modification of the inviscid velocity distribution to achieve the desired transition and separation behavior. In this program, the designer is warned about the presence of separation bubbles which might unacceptably increase the drag over that which is predicted assuming that transition occurs at laminar separation. Although this approach has proven very useful in designing airfoils for low Reynolds number applications, it would be advantageous to have predictions of section properties which more fully account for the presence of laminar separation bubbles provided this can be done without significantly increasing computational requirements. In fact, while above $R = 500,000$ this criterion can be used effectively to design airfoils with short bubbles that do not increase the drag of the airfoil, as the Reynolds number decreases it becomes increasingly difficult to eliminate the detrimental drag increases [Mueller, 1984].

In order to design low Reynolds number airfoils more effectively, a new method of modelling the bubble has been developed in this thesis. It combines the speed of the empirical and semi-empirical approaches of the early years with the accuracy of the more recent interactive methods. This approach rests on the hypothesis that it should be possible to model a local phenomenon such as a laminar separation bubble through local rather than global information. This hypothesis has been confirmed. While the boundary-layer development upstream of laminar separation must in some cases be taken into account in order to predict accurately the transition location inside the bubble, all other characteristics of the bubble flowfield have been found

to depend on a few local scaling parameters that will be discussed in the following chapters. Furthermore, by accounting for the interaction through a local iteration, a uniformly accurate laminar separation bubble model has been developed. This model has been incorporated into the Eppler and Somers program. Although it is unable to account for strong interactions such as the large reduction in the suction peak sometimes caused by leading-edge bubbles, it is able to predict the increase in drag and the local alteration of the airfoil inviscid pressure distribution that are caused by bubbles occurring in the operational range which is of most interest.

In Chapter 2, the reasoning leading to the independent parameters that control the bubble is retraced. In Chapter 3, the calculation of the laminar part of the bubble is described in detail. In Chapter 4, possible approaches to the modelling of transition are discussed together with the method employed here. In Chapter 5, the calculation of the turbulent part of the bubble is described in detail. Several empirical functions necessary to model this most complicated part of the airfoil flowfield are proposed. In Chapter 6, several airfoils are analyzed and the results are compared to experimental data. In Chapter 7, the range of validity of the present model is assessed, important results are summarized, and specific suggestions are given toward enlarging the empirical data base necessary to confirm the present formulation.

Chapter 2

LOCAL PARAMETERS

In this chapter, the approach followed in developing the present laminar separation bubble model is justified. It is then shown how the shortcomings of previous similar models can be remedied by letting the bubble flowfield depend on three local parameters.

Modelling Philosophy

The development of a model of a physical phenomenon entails a three-step process that is usually iterative rather than sequential: (1) identifying which dependent variables need to be modelled, (2) identifying which independent variables best characterize the conditions on which the phenomenon depends, and (3) determining the correct relationships between the two. In the case of incompressible fluid flow, (1) is comprised by the velocity and pressure field, (2) by spatial variables, time, and boundary conditions, and (3) by a differential relationship, the Navier-Stokes equations, which embodies pointwise mass and momentum conservation. This model can be integrated numerically to obtain the dependence of the velocity and pressure on varying geometry and flow conditions for the laminar separation bubble problem as well as for thousands of other flowfields.

Motivated by computational efficiency requirements, methods of varying degrees of approximation have been developed. As soon as approximations are introduced, the modelling challenge changes in nature since assumptions have to be made about what does and what does not need to be approximated and these assumptions must be supported either by analytical arguments or by experimental evidence. For instance, viscous/inviscid interaction methods rely on the boundary-layer assump-

tions and on the extensive analytical and experimental evidence that supports them. There are two important consequences of this type of approximation: (1) the number and types of flowfields that can be analyzed with interactive boundary-layer methods is severely restricted from what could be done by the original equations; (2) by integrating the inviscid or outer problem, the independent conditions are shifted from geometry and spatial variables to flow variables. The final solution is arrived at by allowing the outer and boundary-layer flows to interchange their roles as dependent and independent processes at each iteration, with the relationship between them given by the numerical integration of either Laplace's equation or the boundary-layer equations. Although the solution information is limited to the airfoil surface, approximating high Reynolds number viscous flows in this way adds valuable *integral* insight about the solution over and above the knowledge that it is governed, *pointwise*, by the Navier-Stokes equations.

If the computational requirements are even more stringent, as in the present case, then a more drastic approximation of the physical phenomenon is necessary. The resulting model will be even more limited in applicability and it will have to rely on relationships that are further removed from the original differential pointwise balance and closer to the integrated solutions. In essence, the limit to this approximation process is simply an explicit solution to the original mathematical model of the phenomenon, necessarily obtained at the expense of its generality. That is, if such a solution is not possible at a particular level of approximation, the model is simplified further. The advantages of speed and insight brought by an explicit solution, however, are off-set by a model that may have become too simplistic and restrictive in applicability. In this thesis, the approximation is brought one step beyond the viscous/inviscid interaction approach to a semi-empirical method. In this case, this approach has proven to be a successful compromise between speed, gener-

ality, and understanding. In order to minimize the reliance on empirical "guesses," the governing integral boundary-layer equations are enforced in the bubble and are complemented with a set of simple relationships that capture the essential features of the bubble allowing the prediction of its characteristics and of its effects in general. This formulation was arrived at by starting with the simpler models and adding complexity only after establishing that it was absolutely necessary.

Early Results

In the course of the research reported here, efforts to develop a method able to predict the effects of a laminar separation bubble which interacts weakly with the inviscid flow began with the incorporation of the classical empirical model of Horton [1967], modified according to the suggestions of Roberts [1980] and Schmidt and Mueller [1989], into the Eppler and Somers program. Because they are formulated in terms of integral boundary-layer properties, bubble models such as these are well suited to the integral boundary-layer analysis method employed by Eppler. This method employs two coupled governing differential equations, the momentum and energy integral equations,

$$\frac{d\delta_2}{ds} = \frac{c_f}{2} - (H_{12}+2)\frac{\delta_2}{U}\frac{dU}{ds} \tag{2.1}$$

$$\frac{d\delta_3}{ds} = C_D - 3\frac{\delta_3}{U}\frac{dU}{ds} \tag{2.2}$$

together with appropriate closure relations for c_f, C_D, and H_{12} [Eppler, 1963], given in the Appendix. Contrary to simpler, one-equation methods such as that of Thwaites [1949], in two-equation methods the shape factor (H_{32}, in this case) is obtained directly from the governing equations and is therefore independent of the local pressure gradient parameter. This allows such methods to analyze accurately the non-similar boundary-layer developments characteristic of aerodynamic flows

provided that the assumed family of velocity profiles approximates the actual flow reasonably well.

The empirical models noted above do not take advantage of the accuracy afforded by a two-equation method to calculate the development of the shear layer along the bubble. Instead, they obtain the growth of δ_2 along the bubble by means of rather coarse approximations of these equations. Thus, assuming a constant-pressure plateau between separation and transition and negligible skin friction brought by the near-stagnant fluid in this region leads to

$$(\delta_2)_T = (\delta_2)_S \tag{2.3}$$

from the momentum integral equation. Based on low Reynolds number measurements [Schmidt and Mueller 1986; O'Meara, 1986; Brendel, 1988], Schmidt and Mueller [1989] suggest using, instead,

$$\frac{(\delta_2)_T}{c} = \frac{(\delta_2)_S}{c}\sqrt{1 + \frac{(1.1969)^2(\ell_1/c)}{[(\delta_2)_S/c](Re_{\delta_2})_S}} \tag{2.4}$$

from the similarity solution for the laminar free shear layer. The value of momentum thickness growth predicted by this equation, which was proposed earlier by Russell [1978], increases with decreasing Reynolds number. In order to evaluate this equation, the length of the laminar part of the bubble, given by correlations to be discussed in Chapter 4, must be known.

From the transition point, the growth of δ_2 in the turbulent part of the bubble is approximated by simplifying the momentum and energy integral equations. Combining these two equations leads to Truckenbrodt's shape parameter equation,

$$\delta_2 \frac{dH_{32}}{ds} = (H_{12} - 1)H_{32}\frac{\delta_2}{U}\frac{dU}{ds} + C_D - \frac{c_f}{2}H_{32} \tag{2.5}$$

As discussed by Horton [1967], it appears from experimental data that

$$\left[\frac{dH_{32}}{ds}\right]_{\mathcal{R}} = 0 \tag{2.6}$$

Using this result along with that of vanishing skin friction at a point of reattachment, Horton was able to reduce Eq. (2.5) to

$$\left[\frac{\delta_2}{U}\frac{dU}{ds}\right]_{\mathcal{R}} = -\left[\frac{C_D}{H_{32}(H_{12}-1)}\right]_{\mathcal{R}} = \Lambda_{\mathcal{R}} \tag{2.7}$$

The assumption of a universal reattachment velocity profile and a constant C_D in the turbulent part of the bubble leads to a constant value for $\Lambda_{\mathcal{R}}$. Assuming constant C_D and H_{32} and a linear pressure recovery from transition to reattachment, one can integrate the energy integral equation to obtain the momentum thickness at reattachment,

$$(\delta_2)_{\mathcal{R}} = (\delta_2)_{\mathcal{T}}\left(\frac{U_{\mathcal{T}}}{U_{\mathcal{R}}}\right)^3 + \ell_2\left(\frac{C_D}{4H_{32}}\right)\left(1+\frac{U_{\mathcal{T}}}{U_{\mathcal{R}}}\right)\left[1+\left(\frac{U_{\mathcal{T}}}{U_{\mathcal{R}}}\right)^2\right] \tag{2.8}$$

Then, eliminating $(\delta_2)_{\mathcal{R}}$ between Eqs. (2.7) and (2.8) one obtains

$$\ell_2 = \frac{(\delta_2)_{\mathcal{T}}(\frac{U_{\mathcal{T}}}{U_{\mathcal{R}}})^3(1-\frac{U_{\mathcal{T}}}{U_{\mathcal{R}}})}{\Lambda_{\mathcal{R}} - \left(\frac{C_D}{4H_{32}}\right)\left[1-(\frac{U_{\mathcal{T}}}{U_{\mathcal{R}}})^4\right]} \tag{2.9}$$

In order to implement this result numerically, $U_{\mathcal{R}}$ is decreased in small increments from the value of $U_{\mathcal{T}}$. At each step, ℓ_2 is calculated and it is checked whether or not the segment joining $\mathcal{T}$ to $\mathcal{R}$ intersects the inviscid velocity distribution. When this happens, $(\delta_2)_{\mathcal{R}}$ is calculated from Eq. (2.8) and the turbulent boundary-layer method is started at $s_{\mathcal{R}}$ using this value and $(H_{32})_{\mathcal{R}} = 1.51$ for initial conditions.

This type of formulation is inadequate for several reasons. It does not properly account for the effects of the local viscous/inviscid interaction on the pressure distribution in the laminar part and therefore cannot accurately calculate the growth of δ_2 in this region. It relies on local empirical transition criteria which are unable to sense the influence of the upstream boundary-layer development. Also, in actuality, neither H_{32} nor C_D are constant in the turbulent part of the bubble.

The turbulent recovery distribution can deviate appreciably from a straight line. Finally, the pressure at the reattachment point can be significantly below or above the corresponding inviscid value.

In an attempt at better approximating the pressure distribution induced by the bubble, van Ingen's functions were implemented [Ingen and Boermans, 1986]. In the laminar part use is made of the empirical function

$$\frac{U}{U_S} = .978 + .022\exp(-4.545\xi - 2.5\xi^2) \tag{2.10}$$

where

$$\xi = \frac{s - s_S}{(R_{\delta_2})_S(\delta_2)_S} \tag{2.11}$$

which allows for a slight pressure recovery between separation and transition. For the turbulent part, a Stratford pressure distribution is employed and again it is assumed that reattachment occurs at the intersection with the inviscid distribution. Fig. 2-1 shows a comparison between the Horton and Stratford recoveries. The dashed line is the locus of possible reattachment points as given by Eq. (2.9).

Using the empirical separation bubble model noted, the sensitivity of the boundary-layer development and drag prediction to various parts of the bubble was explored. In order to achieve accurate drag polar predictions, it was found necessary to capture the vanishing of the bubble with increasing adverse pressure gradient while at a constant chord Reynolds number. It is found that the transition length for such empirical models responds to variations in chord Reynolds numbers but not in pressure gradient. The drag prediction, in turn, is very sensitive to small variations in the governing parameters, for instance, the pressure level at the beginning of the turbulent pressure recovery. Thus, although generally capable of predicting features of the bubble to within thirty percent, empirical bubble models based only on conditions at separation cannot provide acceptable drag predictions. Fig. 2-2 shows the aerodynamic characteristics of the Eppler E387 airfoil

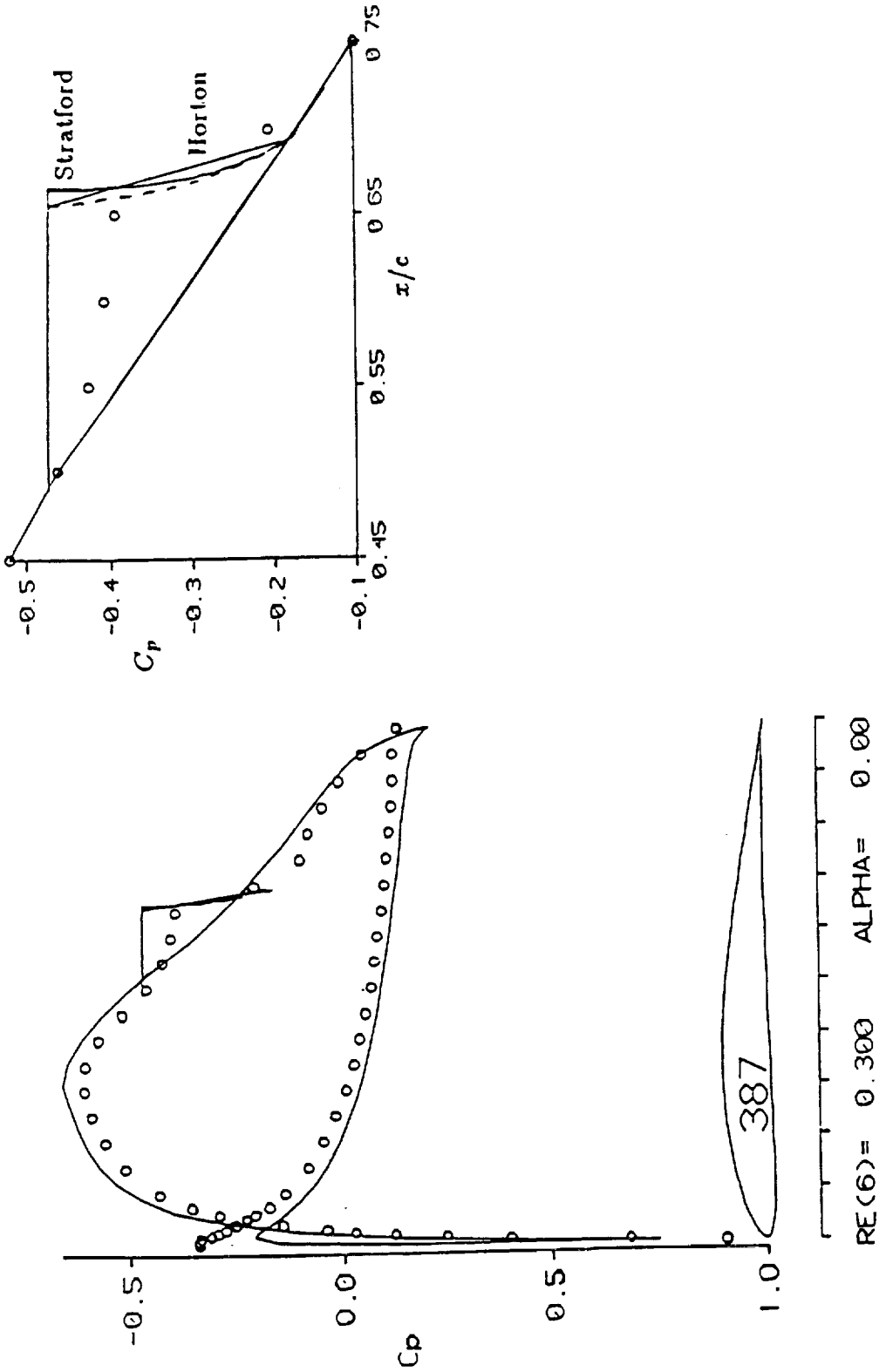

Fig. 2-1 Prediction of bubble pressure distribution. Comparison of Horton and Stratford recoveries. Data are from McGhee [1988].

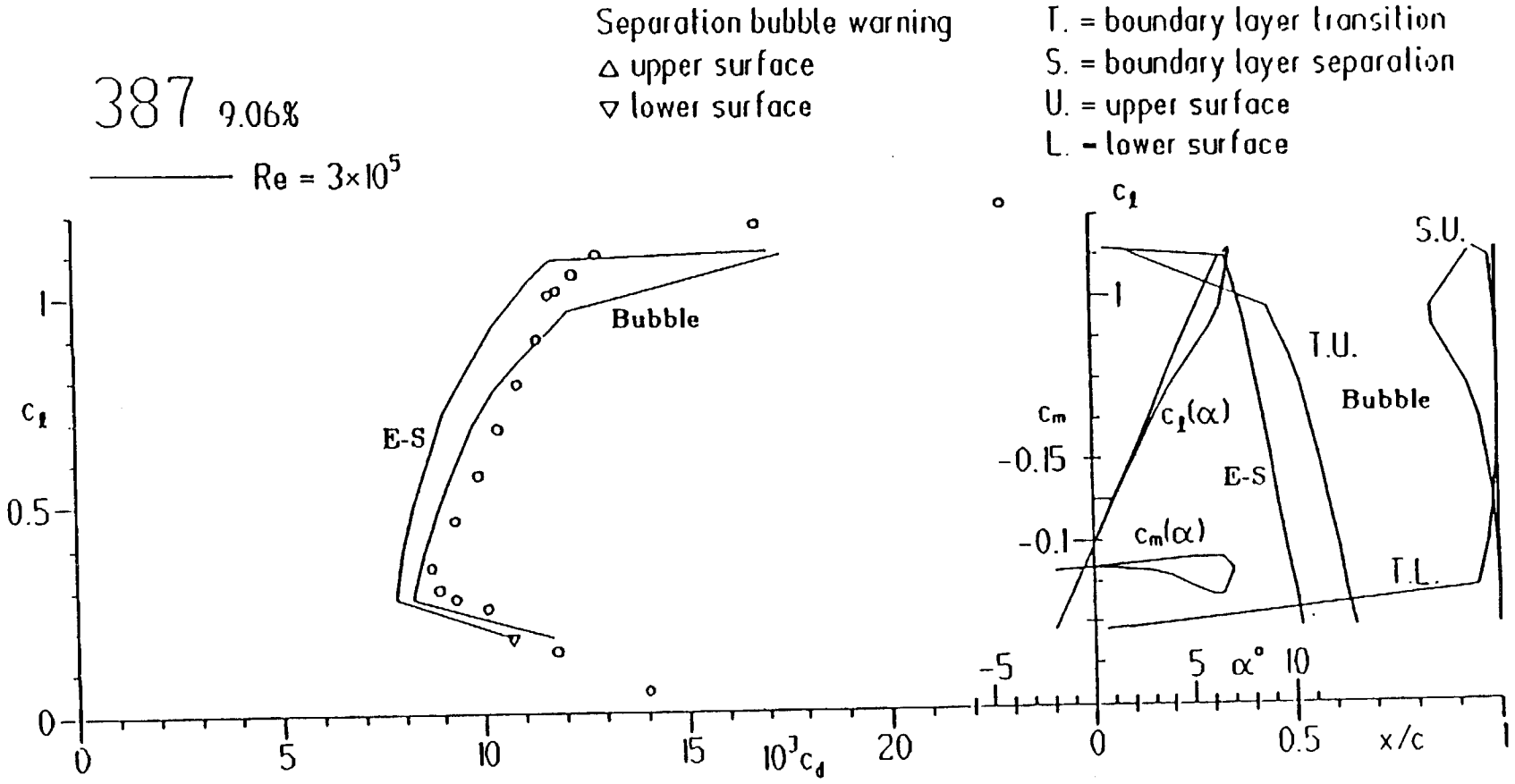

Fig. 2-2 Aerodynamic characteristics for the Eppler E387 airfoil obtained with the original Eppler and Somers program compared with those obtained using the program incorporating the bubble model with the characteristics: inviscid Cp, transition by Schmidt [1986], $(\delta_2)_T$ from Eq. (2.4), $U_T = U_S$, Stratford recovery, $(H_{32})_R = 1.51$. Experimental data are from McGhee et al. [1988].

at $R = 300,000$ obtained with this early version of the bubble model compared to the original Eppler and Somers prediction and the measurements of McGhee et al. [1988] taken in the Low Turbulence Pressure Tunnel at the NASA-Langley Research Center.

Before beginning a discussion of possible alternatives to the above approximations, two issues indirectly affecting the bubble model should be addressed. Firstly, due to the presence of the boundary layer, the experimental pressure distribution does not equal the inviscid one at the same angle of attack but falls inside it, leading to a smaller lift coefficient. If a weakly interacting bubble is present, it will modify the viscous pressure distribution only locally. Using the inviscid pressure distribution to drive the bubble model, therefore, necessarily leads to a discrepancy between the predicted and measured results if the same angle of attack is prescribed. This discrepancy can be eliminated by employing a viscous/inviscid interaction algorithm. While appropriate for analyzing near-stall conditions, methods of this type are not really necessary at lower lift coefficients where the design effort is most often concentrated. In fact, since aerodynamic characteristics are usually compared at the same c_ℓ rather than at the same α, the difference in angle of attack between the experimental and inviscid lift coefficients poses no obstacles to comparing drag predictions obtained with the inviscid pressure distribution to the experimental drag polar. It may be expected that the validity of the present model will decrease for mid-chord bubbles on highly aft-loaded airfoils and for leading-edge bubbles near bursting.

Secondly, the turbulent boundary-layer analysis method developed by Eppler and employed in the program is based on empirical equilibrium relationships between the integral variables [Eppler, 1963]. While quite appropriate for analyzing high Reynolds number flows without bubbles, such a method cannot correctly ac-

count for the relaxing, nonequilibrium turbulent boundary layer downstream of reattachment, especially at lower Reynolds numbers. The present model, therefore, makes use of the nonequilibrium turbulent boundary-layer method developed by Drela [1986]. To provide a comparison between these two boundary-layer methods, in Figs. 2-3 and 2-4 the Eppler E387 and the NASA NLF(1)-1015 airfoils are analyzed assuming transition at the laminar separation point using the original and Drela's turbulent boundary-layer methods. The turbulent separation point predicted by Drela is downstream of that predicted by Eppler for the low Reynolds number case but is equal to it at the higher Reynolds number. The drag coefficient, however, is consistently higher by 10 to 15 counts.

The Local Independent Parameters Controlling the Bubble

It is stated in Chapter 1 that the present model has confirmed the hypothesis that it should be possible to model the weakly interactive bubble solely by means of local parameters, with the exception of the transition process. Although transition may be the most important effect, it is not of much help without an accurate estimation of the bubble flowfield. Thus, the failure of the early empirical models can be traced not only to their poor modelling of transition but also to their inability to capture the principal physical processes in the two parts of the bubble. In spite of this, their reliance on local conditions has not been abandoned in the present model. Rather, it has been extended to achieve a more detailed prediction of this flowfield. Specifically, the local parameters must be able to characterize three aspects of the bubble flowfield that have been found to control all other bubble characteristics: the boundary-layer momentum thickness at separation, the mean inviscid pressure gradient along the bubble, and the thickness of the bubble at transition. In addition, the correct lowest-order response of the bubble to these inputs must be identified. The failure or success of previous approaches to predict the bubble flowfield and its

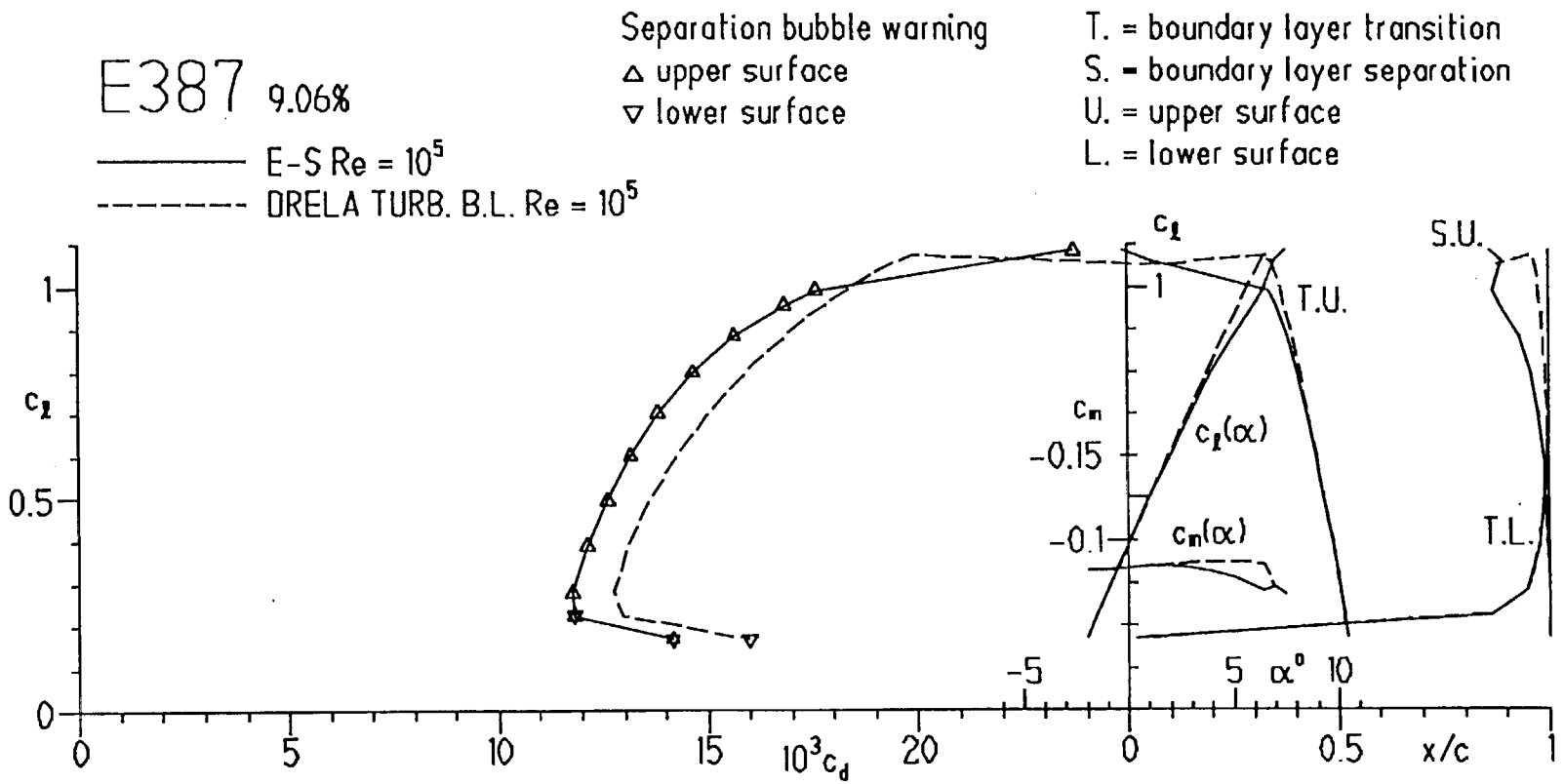

Fig. 2-3 Comparison of the Eppler and Drela turbulent boundary-layer methods at a low Reynolds number. Transition at laminar separation.

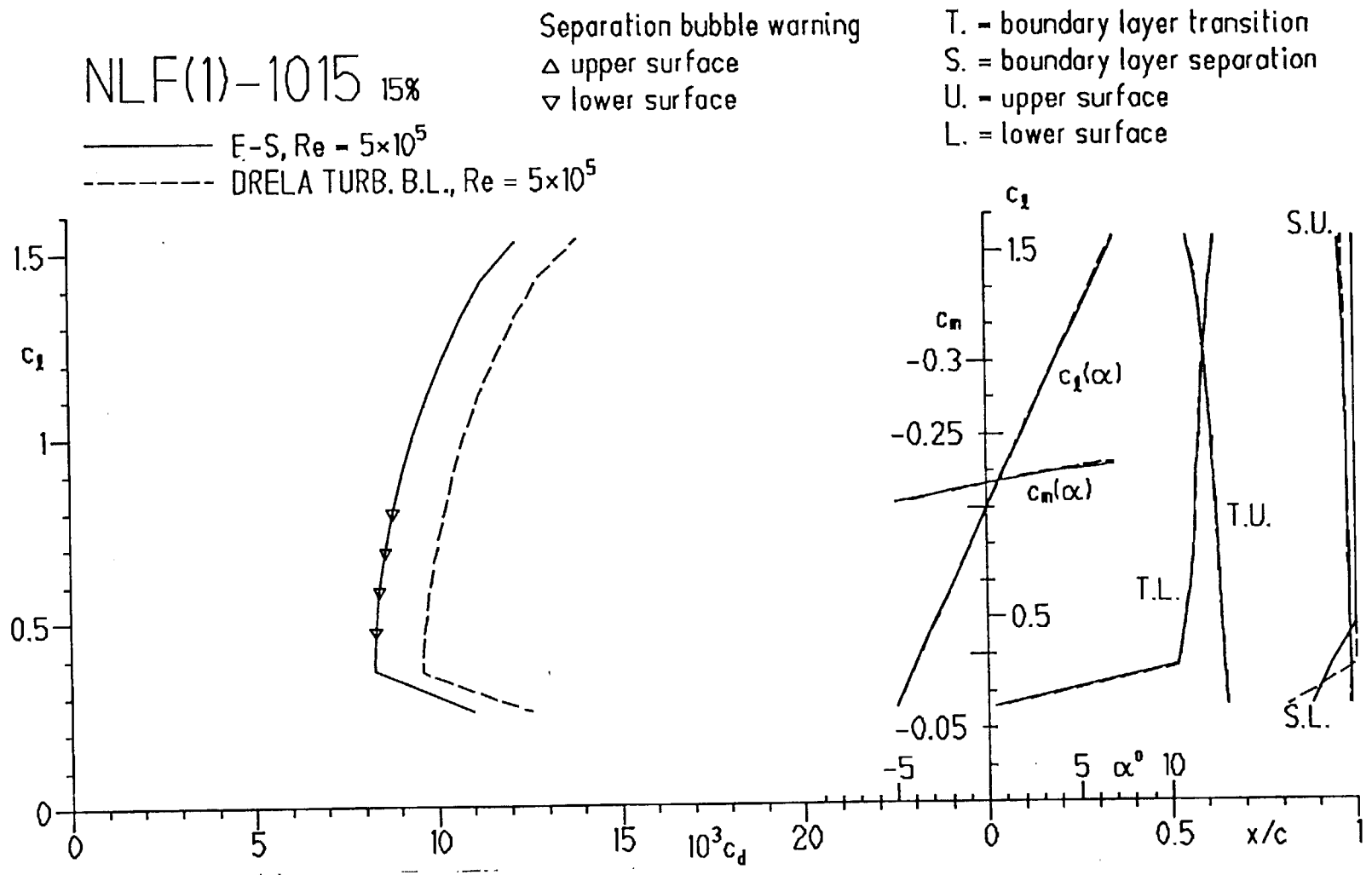

Fig. 2-4 Comparison of the Eppler and Drela turbulent boundary-layer methods at an intermediate Reynolds number. Transition at laminar separation.

effects on airfoil performance can be shown to be directly related to their failure or success to account properly for these independent and local flow conditions.

The first investigators of the bubble problem recognized that the transition location plays a fundamentally important role in determining the size of the bubble. They therefore recognized the need to estimate the degree of instability present in the boundary layer as it separates from the surface. A very stable boundary layer at separation, in fact, is likely to be followed by a fairly long bubble, whereas an unstable one would be associated with a shorter bubble. The Reynolds number has been universally used as an indicator of how far from turbulence a particular flowfield is. In addition, as the chord Reynolds number is decreased, the bubble becomes longer until it bursts at the critical value. It seemed plausible, therefore, that a good correlating parameter for the stability of the separating boundary-layer flow could be arrived at by forming a Reynolds number with the value of inviscid velocity and momentum thickness at laminar separation as characteristic velocity and length,

$$(R_{\delta_2})_S = \frac{U_S(\delta_2)_S}{\nu} \tag{2.12}$$

This parameter is certainly useful but, unfortunately, only provides a coarse indication of the stability of the flow at laminar separation. Another parameter that has been used extensively in empirical correlations is the value of momentum thickness at laminar separation nondimensionalized with respect to the airfoil chord. Rather than a measure of the stability of the separating shear layer, this parameter only contains information on how much momentum has already been lost by the boundary layer upon reaching the laminar separation point. These criteria lack sensitivity to the effect of the pressure distribution on transition, namely the effect of the upstream boundary-layer development. As will be discussed in Chapter 4, this effect is well modelled by the e^n method of linear stability theory.

Another effect that needs to be accounted for is the local strong viscous/inviscid interaction. Since this interaction is a result of the presence of separated flow and since the amount of separated flow is affected by the severity of the pressure gradient and by $(\delta_2)_S$, it is not surprising that this effect has been found to scale well with a parameter that incorporates these flow conditions, Gaster's pressure gradient parameter, given by Eq. (1.4).

It should be mentioned at this point that a recent study [Pauley et al., 1989] of the laminar separation bubble shows Gaster's parameter to be important in yet another respect. In this study, the unsteady laminar Navier-Stokes equations are discretized to calculate the flow through a duct. Although the local Reynolds number of the flow based on the distance between the entrance of the tunnel and the laminar separation point is on the order of $R = 50,000$-$300,000$, transition to turbulence cannot be accurately computed (computational unsteadiness can occur) due to the grid resolution and time-step used to keep the computational requirements within reasonable limits. A suction port on the upper wall of the duct provides an adverse pressure gradient for the laminar boundary layer developing along the lower wall.

The value of the parameter $P_{max} = .24$, a modification to Gaster's parameter with the velocity gradient representing the maximum rather than the average inviscid gradient between separation and reattachment, is found to correspond to the boundary between steady and unsteady reattachment of the laminar shear layer. This boundary correlates well to Gaster's bursting line such that it separates the long (steady, $P_{max} < .24$) from the short (unsteady, $P_{max} > .24$) bubbles measured by Gaster. Because of this correlation between the steady and long bubbles and the unsteady and short bubbles, it is proposed by Pauley et al. that the reattachment process may be governed by the large-scale laminar pressure field rather than by

turbulent transfer of momentum. While this cannot be proved or disproved with certainty, the onset of unsteadiness can be justified in the case of laminar flow. In fact, as P_{max} increases, the inviscid gradient and/or the momentum loss at separation increases. Thus, a greater momentum transfer is necessary to recover the inviscid pressure and/or to accelerate the sizable amount of reverse flow. As the laminar shear layer is not capable of such momentum transfer, reattachment probably occurs due to Coanda's effect, or the formation of a low-pressure region below the shear layer. This effect as it relates to laminar separation bubbles is discussed by Russell [1978]. When the adverse inviscid gradient exceeds the favorable suction of the flow below the shear layer, the bubble starts growing without bounds; until, that is, the large vortex of recirculating flow at constant pressure becomes unstable and is shed causing the bubble to collapse in size. This small bubble then starts growing again and the cycle repeats.

Before the above description was arrived at, it was thought that transitional bubbles, too, were unsteady in the large scale and short-time mean. It was also thought that the unsteadiness near reattachment would feed back upstream and influence the transition location. It seems now that if there is some unsteadiness it should not necessarily be periodic in nature and that the turbulent transfer of momentum is a much more significant factor in determining reattachment than Coanda's effect if turbulence is present. Although the final word on transition cannot be given with the method used in the present model, it appears at this point to depend mainly on upstream rather than downstream conditions. It is still not clear, therefore, why the unsteady laminar simulation reported by Pauley et al. correlates so well with Gaster's measurements of transitional bubbles. Resolution of this issue may have to wait for a complete understanding of bubble bursting.

Given a means of approximating the viscous/inviscid interaction in the laminar

part of the bubble and the transition location, the height of the bubble at transition can be estimated. This geometrical characteristic of the bubble is the keystone that bridges the laminar and the turbulent parts, providing the correct characteristic length for the latter. As the spreading angle of the turbulent shear layer is a weak function of Reynolds number and pressure gradient, in fact, the length of the turbulent part of the bubble follows directly and the model is thereby closed.

Chapter 3

THE LAMINAR PART OF THE BUBBLE

The Eppler and Somers program uses a very reliable criterion to detect laminar separation. It is based on the value of the energy to momentum thickness shape factor,

$$(H_{32})_S = 1.515095 \tag{3.1}$$

This value is approached from above. Upon detection of laminar separation, the development of the separated laminar shear layer is calculated using the momentum and energy integral equations, together with closure relations to be discussed below. Instead of implementing this boundary-layer method in the inverse mode as it is usually done, the development of a general family of pressure distributions in the laminar part of the bubble allows its calculation in the direct mode.

Pressure Distribution

The function used to approximate the pressure distribution in the laminar part of the bubble is a generalization of that developed by van Ingen and Boermans [1986] and given by Eq. (2.10). This distribution allows a slight pressure recovery after laminar separation, quickly approaching a limiting value. Using detailed pressure distributions in the bubble region available from wind-tunnel tests of the NASA NLF(1)-1015 airfoil in the NASA-Langley Low-Turbulence Pressure Tunnel, the accuracy of Eq. (2.10) was checked for several different conditions. It was found that, as the pressure gradient along the bubble decreases, the pressure distribution tends to fall below van Ingen's curve while, as the pressure gradient steepens, it becomes flatter, closer to Horton's approximation and above van Ingen's curve. It is therefore postulated that Eq. (2.10) can be improved by relaxing the amount of

pressure recovery between separation and transition,

$$\frac{U}{U_S} = (1 - DU) + DU \exp(-4.545\xi - 2.5\xi^2) \tag{3.2}$$

The steeper the pressure gradient along the bubble, the smaller the value of DU. This behavior is consistent with an inviscid velocity distribution calculated over an ever-thickening displacement surface in a steepening adverse gradient.

While the agreement with the experimental distributions was much improved by use of Eq. (3.2), an inconsistency became apparent when attempting to predict the pressure distribution over leading-edge bubbles. Given the very large gradients along these bubbles, the predicted pressure distributions in the laminar part were quite flat, in contrast to the measurements which show only a small perturbation of the inviscid distribution with a significant pressure recovery between separation and transition. This apparent contradiction with the trend observed for mid-chord bubbles can be resolved once it is realized that the amount of pressure recovered is inversely proportional to the magnitude of the perturbation of the displacement surface, that is, to the amount of fluid entrained by the bubble. Near the leading edge, the boundary layer is so thin that the short bubbles ($1-6\%c$) usually observed there can only hold a very small amount of fluid and can therefore only modify the inviscid distribution slightly.

Although there is a strong correlation between the thickness of the boundary layer at separation and the amount of fluid caught in the separated region, the value of $(\delta_2)_S$ more precisely reflects the input to the momentum balance that determines such amount: the greater the momentum already lost by the boundary layer, that is, the greater the amount of separated flow necessary to counteract the imposed inviscid gradient. The variable DU should therefore depend both on the average pressure gradient along the bubble as well as on $(\delta_2)_S$. Both these effects are included in Gaster's pressure gradient parameter, Eq. (1.4) which, for this

reason, is thought to be a better independent parameter than simply the average dimensionless inviscid velocity gradient along the bubble,

$$\frac{\Delta(U/U_\infty)}{\Delta(s/c)} \tag{3.3}$$

In dimensionless variables P becomes,

$$P = R\left[\frac{(\delta_2)_S}{c}\right]^2 \frac{\Delta(U/U_\infty)}{\Delta(s/c)} \tag{3.4}$$

From experimental pressure distributions, it is found that DU is well represented as a function of the Gaster pressure gradient parameter, P. This functional relationship, shown in Fig. 3-1, was developed by extracting corresponding values of DU and P directly from the experimental pressure distributions of the NLF(1)-1015 [NASA LaRC LTPT, June 1987] and the Eppler E387 airfoils [McGhee et al., 1988]. The solid line is a quadratic least-squares fit that has been included in the model,

$$DU = \begin{cases} 0.0610 + 0.3048P + 0.5072P^2 & -P < .3 \\ 0.0152 & -P > .3 \end{cases} \tag{3.5}$$

The value of $DU = 0.022$ used by van Ingen and Boermans falls in the middle of the variation in DU shown in Fig. 3-1.

As pointed out by van Ingen [1989], the factor 4.545 in Eq. (3.2) was derived to ensure continuity in the velocity gradient when Thwaites's laminar boundary-layer method is used to determine the laminar separation point. In fact, if the derivative of Eq. (2.10) is evaluated at laminar separation and the variables are rearranged, one obtains

$$\left[\frac{(\delta_2)^2}{\nu}\frac{dU}{ds}\right]_S = -(4.545)(.022) = -.10 \tag{3.6}$$

which is Thwaites's laminar separation criterion. Eppler's separation criterion (Eq. (3.1)), however, corresponds to slightly different values of Thwaites's parameter for differing upstream developments. Furthermore, in the present formulation a

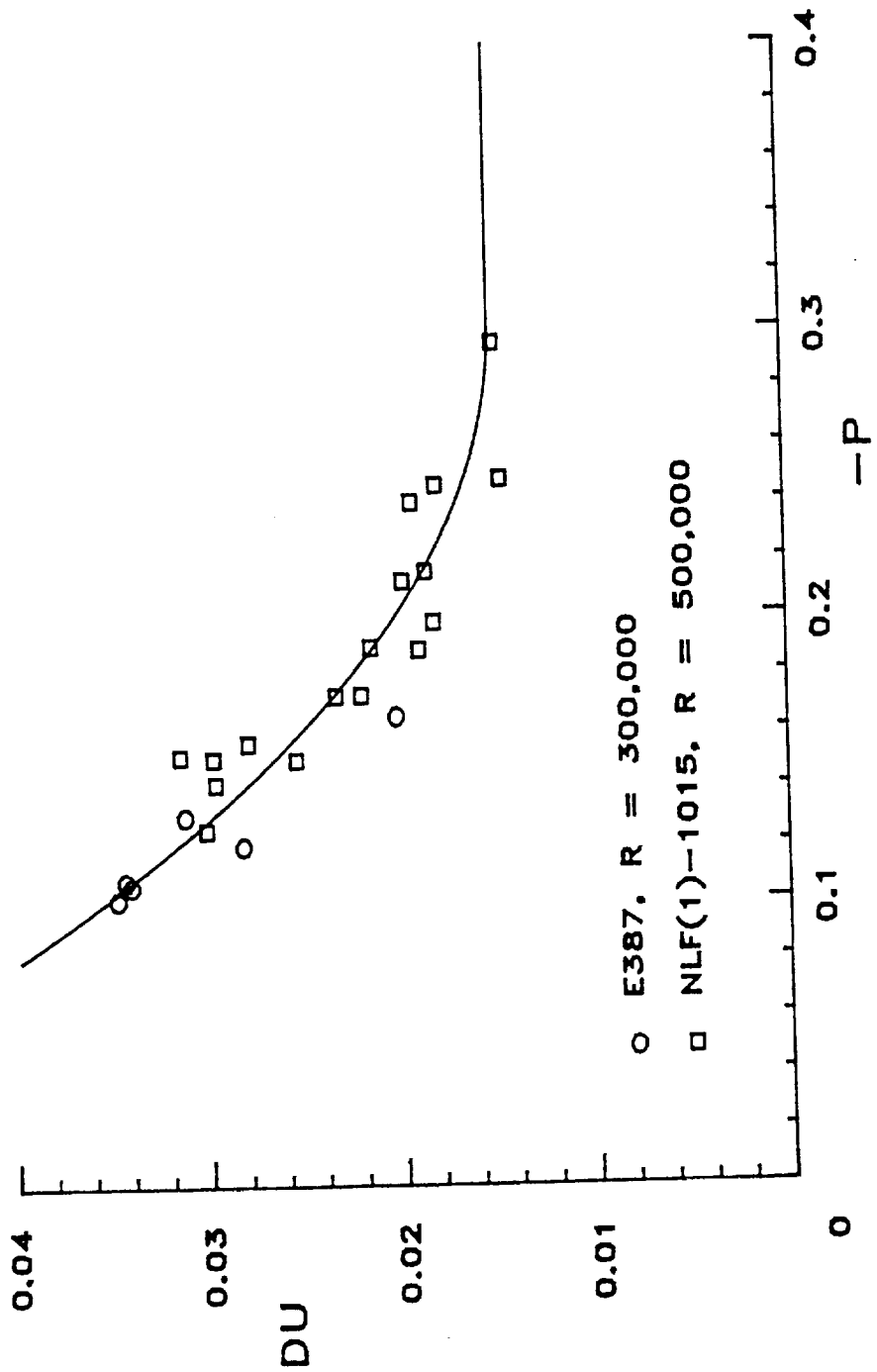

Fig. 3-1 Pressure recovery in the laminar part of the bubble as function of Gaster's pressure gradient parameter.

variable DU is used in place of 0.022. Therefore, the constant necessary to ensure a continuous velocity gradient at separation when Eq. (3.2) is used in conjunction with Eppler's laminar boundary-layer method is

$$C = -\frac{1}{DU}\left[\frac{(\delta_2)^2}{\nu}\frac{dU}{ds}\right]_S \tag{3.7}$$

When C is substituted for 4.545 in Eq. (3.2), the result is

$$\frac{U}{U_S} = 1 - DU\left\{1 - \exp\left[\frac{1}{DU}\frac{U'_S}{U_S}(s - s_S)\right]\right\} \tag{3.8}$$

where the prime denotes the derivative with respect to s and the second term in the exponent of the original expression has been neglected.

Closure

In order to integrate the momentum and energy integral equations in the direct mode as driven by the pressure distribution given above, closure correlations for H_{12}, c_f, and C_D must be provided. The most natural choice is to use the reversed Falkner-Skan, or Stewartson [1954], profiles since the attached Falkner-Skan, or Hartree, profiles [Schlichting, 1979] are used to develop the correlations upstream of separation. Recent measurements by Fitzgerald and Mueller [1990], however, seem to indicate that the Stewartson profiles may not be the best choice. This matter was therefore examined in some detail.

Fitzgerald and Mueller [1990] have obtained good agreement between their measurements and the two-parameter profile family originally developed by Green [1966] for a turbulent shear layer forming a free stagnation point downstream of a base. As shown in Fig. 3-2, the two parameters are linked to the geometrical characteristics of the profiles. (h/b) is the ratio of the distance of the shear layer from the centerline of the wake to the width of the shear layer and G is the amplitude of Coles's wake function. Since there is slip along the centerline of such a

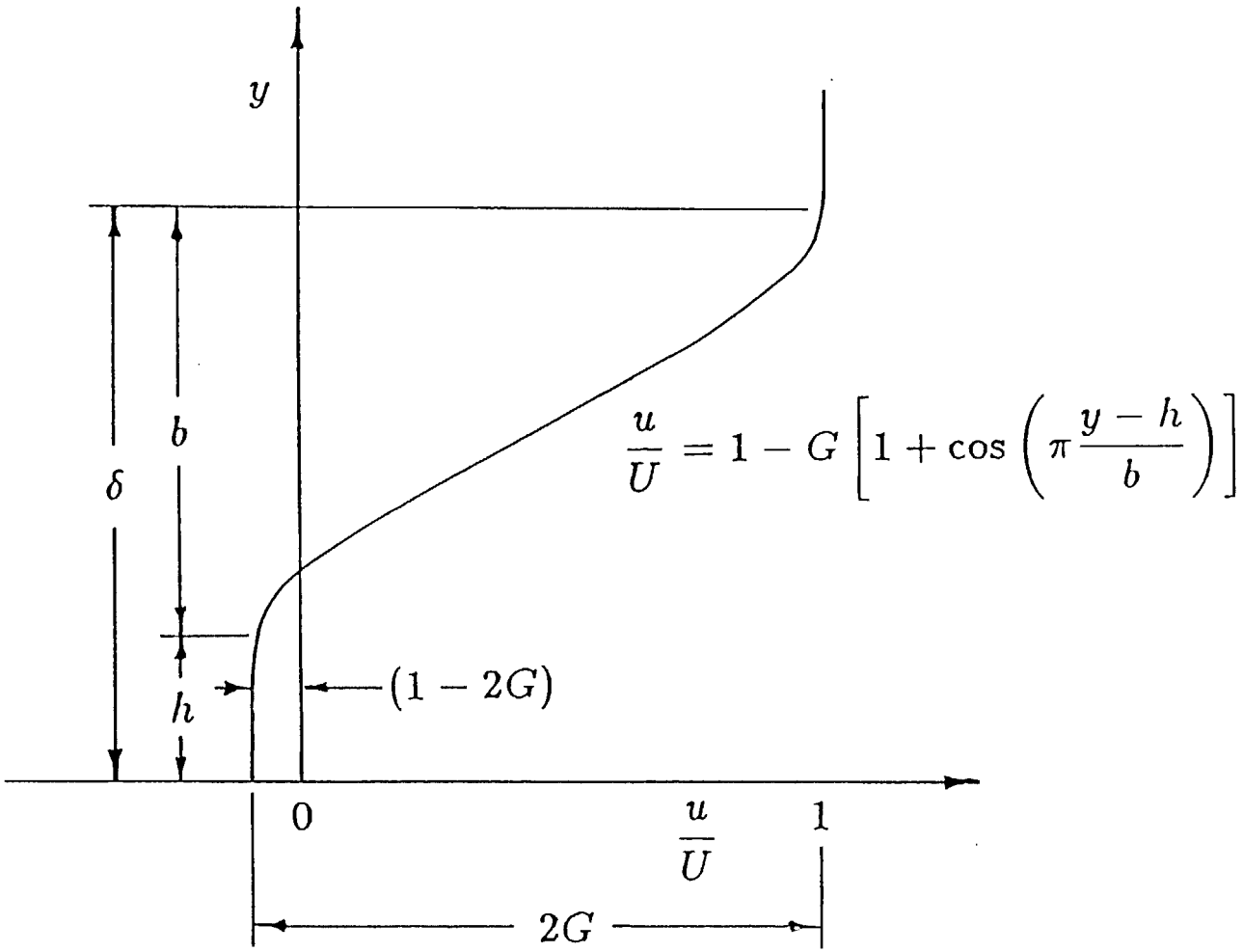

Fig. 3-2 Green's two-parameter reversed velocity profile.

recirculating base flow, these profiles cannot be used to develop a correlation for c_f. By applying the definitions for the integral thicknesses of the boundary layer and for the dissipation coefficient, the following relationships are obtained:

$$H_{12} = \frac{1 + 2\frac{h}{b}}{(1 - \frac{3}{2}G) - 2\frac{h}{b}(1 - 2G)} \tag{3.9}$$

$$H_{32} = \frac{(2 - \frac{9}{2}G + \frac{5}{2}G^2) + 4\frac{h}{b}(1 - 3G + 2G^2)}{(1 - \frac{3}{2}G) - 2\frac{h}{b}(1 - 2G)} \tag{3.10}$$

$$R_{\delta_2} C_D = \frac{\pi^2 G^3}{2}[1 - \frac{3}{2}G + 2\frac{h}{b}(1 - 2G)] \tag{3.11}$$

In order to compare these relationships to those obtained from the Stewartson profiles, it is necessary to know how the two parameters vary inside the bubble. The values used by Fitzgerald and Mueller to fit the profiles measured inside one bubble can serve as a starting point. The three boundary-layer variables are evaluated at values of the parameters corresponding to the same downstream station inside the bubble and then plotted against one another. The same calculations are then repeated for values of G and (h/b) similar to those used by Fitzgerald and Mueller in order to determine the sensitivity of the correlations to these parameters. The result is shown in Figs. 3-3 and 3-4 where these new two-parameter correlations are compared to those developed by Drela [1986] from the Stewartson profiles. The solid lines utilize the fitted variations of G and (h/b). As both H_{12} and H_{32} increase monotonically between separation and transition, moving to greater values of the abscissa on these plots corresponds to moving downstream inside the bubble. Thus, both are very similar to the Stewartson correlations near separation but can be quite different further downstream.

While $H_{12}(H_{32})$ seems quite sensitive to changes in the parameters, $C_D(H_{32}, R_{\delta_2})$ is not, thereby making the determination of its exact dependence on G and (h/b) less crucial. It appears from the measurements that the back-flow,

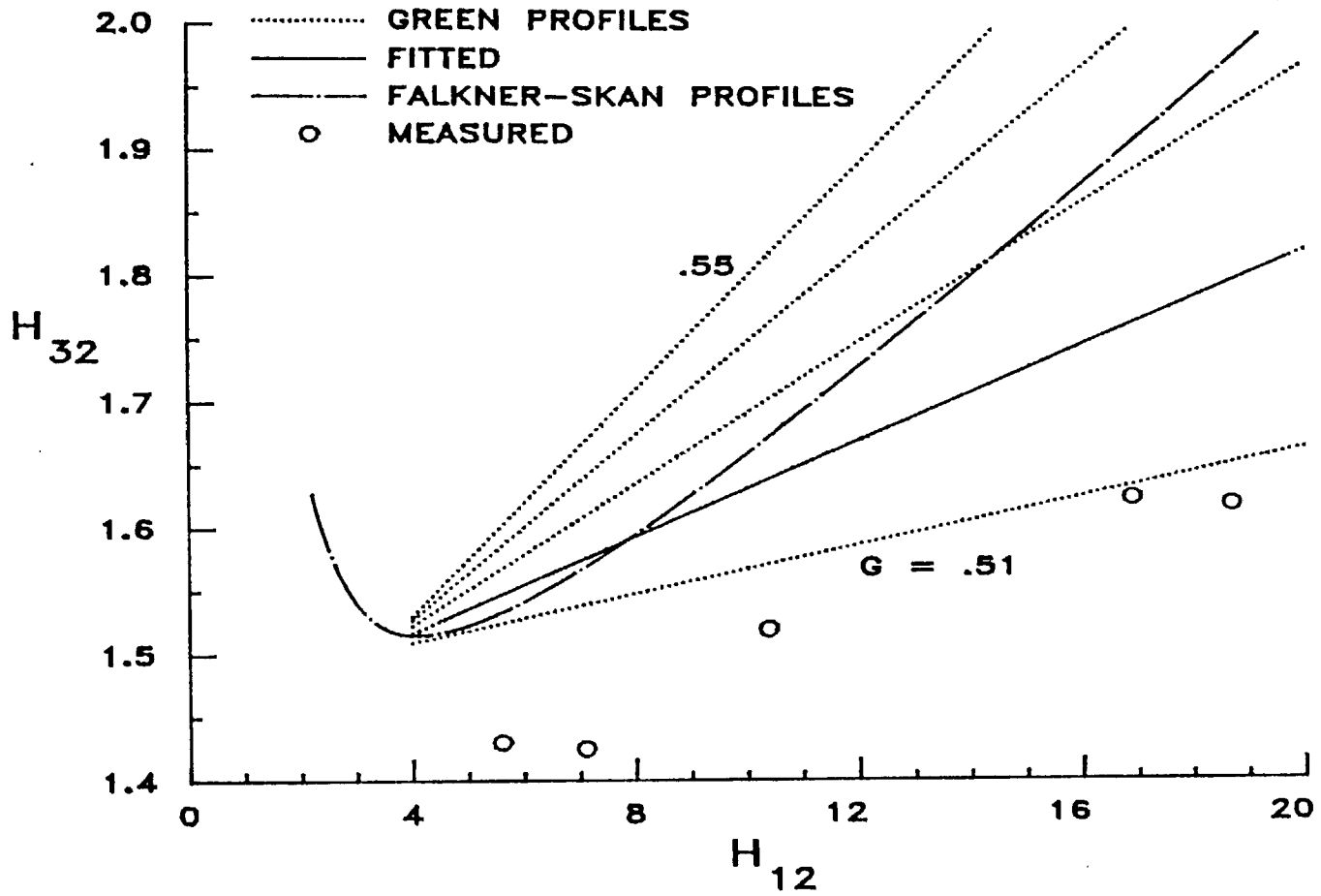

Fig. 3-3 Comparison of the shape-factor correlation for the Falkner-Skan and Green profiles.

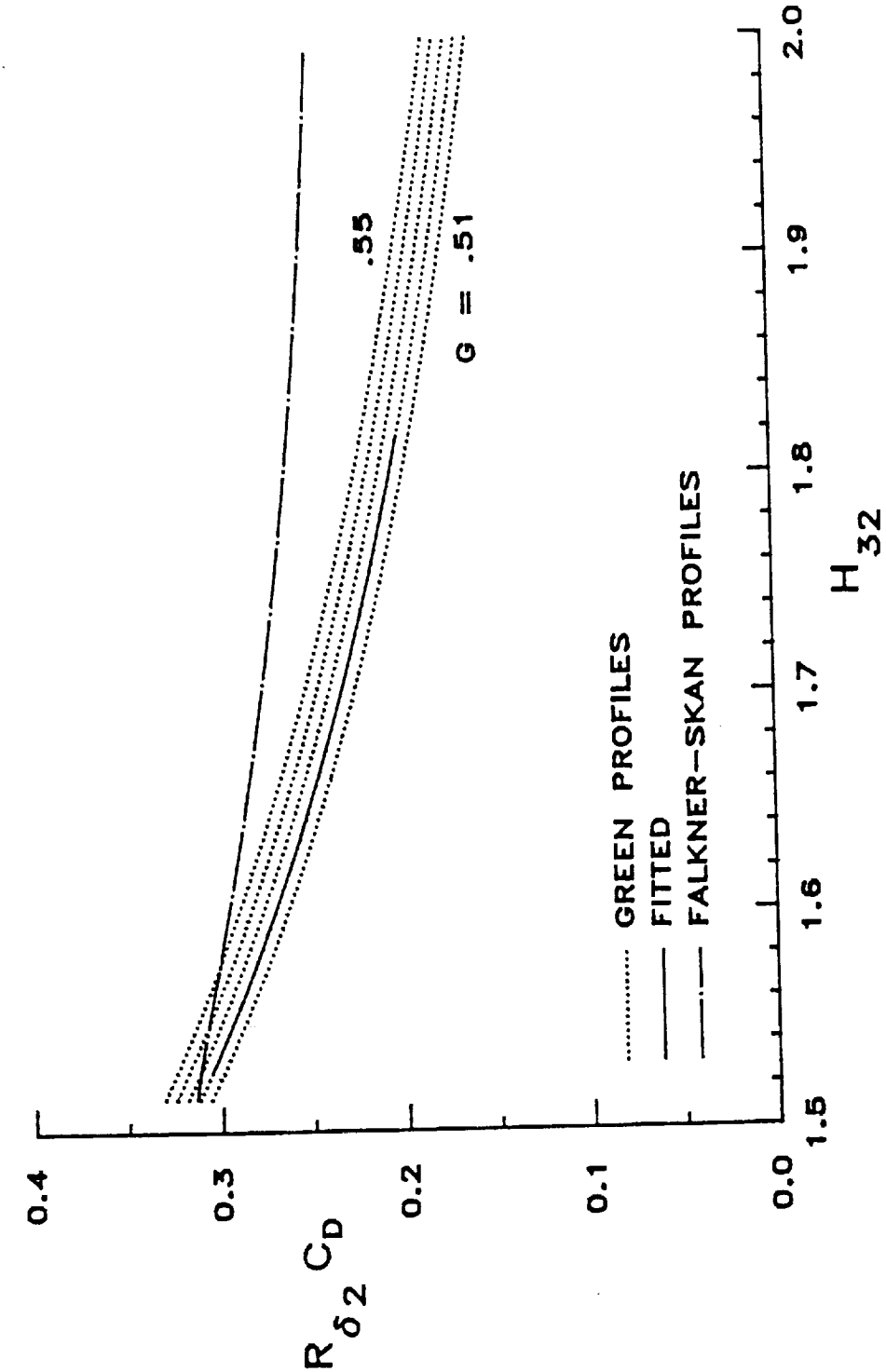

Fig. 3-4 Comparison of the dissipation coefficient correlation for the Falkner-Skan and Green profiles.

proportional to G, may be constant within each bubble although different for different bubbles. As shown in Fig. 3-3, the values of shape factors actually measured, although different in absolute value, follow the same slope, thus confirming a constant value of back-flow velocity. These considerations justify eliminating (h/b) between Eqs. (3.9) and (3.10) and expressing the closure relationships in terms of H_{32}, calculated from the governing equations and G, whose behavior within each bubble appears easier to correlate to local flow conditions,

$$H_{12} = \frac{3(1-G) - H_{32}}{(1-G)(1-2G)} \tag{3.12}$$

$$R_{\delta_2} C_D = \frac{\pi^2 G^3}{2} \left[1 - \frac{3}{2} G - \frac{(4-5G)(1-G) - (2-3G)H_{32}}{4(1-G) - 2H_{32}} \right] \tag{3.13}$$

Although very encouraging, these results do not appear sufficiently well developed to be implemented in the model in their present form. In fact, the dependence of G on local flow conditions is unknown and no measure of c_f can be obtained from these profiles. By contrast, although the details of the velocity profiles are not well represented by the Stewartson profiles, the integrated parameters derived from them are not far from the corresponding values obtained with the fitted Green profiles. It seems better, therefore, to keep using the Stewartson profiles, for now, until these issues have been resolved. Accordingly, the closure correlations developed by Drela [1986] have been implemented in the model. Since the governing integral equations yield the value of H_{32} directly, Drela's shape factor correlation is inverted,

$$H_{12} = \frac{H_{32} - 1.194068}{0.08} + \left[\left(\frac{H_{32} - 1.194068}{.04} \right)^2 - 64.4 \right]^{\frac{1}{2}} \tag{3.14}$$

The skin-friction coefficient is found from

$$R_{\delta_2} \frac{c_f}{2} = \begin{cases} -0.067 + 0.01977 \frac{(7.4 - H_{12})^2}{H_{12} - 1}, & H_{12} < 7.4 \\ -0.067 + 0.022 \left[1 - \frac{1.4}{H_{12} - 6} \right]^2, & H_{12} \geq 7.4 \end{cases} \tag{3.15}$$

while the dissipation coefficient is given by

$$R_{\delta_2}\frac{C_D}{H_{32}} = 0.207 - 0.003(H_{12} - 4)^2 \tag{3.16}$$

Removal of the Separation Singularity

Knowledge of the pressure distribution downstream of separation has led to a simple technique for removing the Goldstein singularity at laminar separation and to allow for some effect of the bubble on the pressure distribution upstream of laminar separation. When the development of the laminar shear layer is calculated in the direct mode from laminar separation using the function described above, the boundary-layer variables remain at their separation values for a few percent chord before starting to grow normally. This is believed a consequence of the singularity, in the following sense. The growth of the boundary-layer variables upstream of separation does not reflect just the local pressure gradient but is increasingly affected by the singularity as separation is approached. This effect is equivalent to a much steeper pressure gradient than is actually present and causes the distribution of H_{32} to exhibit a very steep slope immediately upstream of separation. The skin-friction coefficient behaves similarly and thereby leads to a prediction of the separation point upstream of the experimentally observed location. Therefore, when the separation values are incremented downstream of separation using a pressure gradient continuous with its value upstream, it is felt by the boundary layer as, in fact, a much gentler gradient which cannot maintain the previous rate of growth. In the present model, the point where the separated laminar shear layer starts growing again is taken as the actual laminar separation point. The laminar boundary layer is therefore calculated again from a few percent chord upstream of the "inviscid" laminar separation point to this point by prescribing between them an assumed (cubic) development of $H_{12}(s)$ and solving the laminar boundary-layer equations

in the inverse mode. Smooth growth of the boundary layer through the separation point results.

The local inverse solution causes the velocity distribution to start deviating from the inviscid some distance upstream of the laminar separation point. As this distribution matches the experimental measurements, this behavior of the separation point and of the corresponding velocity distribution is believed to be correct. In fact, as the boundary-layer assumptions break down as separation is approached, a modification to the inviscid pressure distribution upstream of separation is to be expected. Referring to Fig. 3-5, as the new separation point is usually at a higher pressure than the original, the old value of DU is usually too great and a new one is calculated from

$$DU_{new} = DU_{old} - \frac{(U_S)_{old} - (U_S)_{new}}{(U_S)_{old}} \tag{3.17}$$

Using this value and the new value for the velocity gradient at separation, Eq. (3.8) can be used to generate a new velocity distribution whose tangent is continuous with the current distribution at the separation point.

Separation Angle

Using the new value of momentum thickness at the "viscous" separation point, the tangent of the angle the separating streamline makes with the surface is given by an empirical relationship proposed by Wortmann [1974],

$$\tan\gamma = -\frac{64P}{(R_{\delta_2})_S} \tag{3.18}$$

A similar relationship proposed by van Ingen et al. [1980] was also examined,

$$\tan\gamma = \frac{B}{(R_{\delta_2})_S} \tag{3.19}$$

B is given the experimental mean value of 17.5. The model did not perform at all well with the latter relationship. The reason is that the factor $64P$ assumes a wide

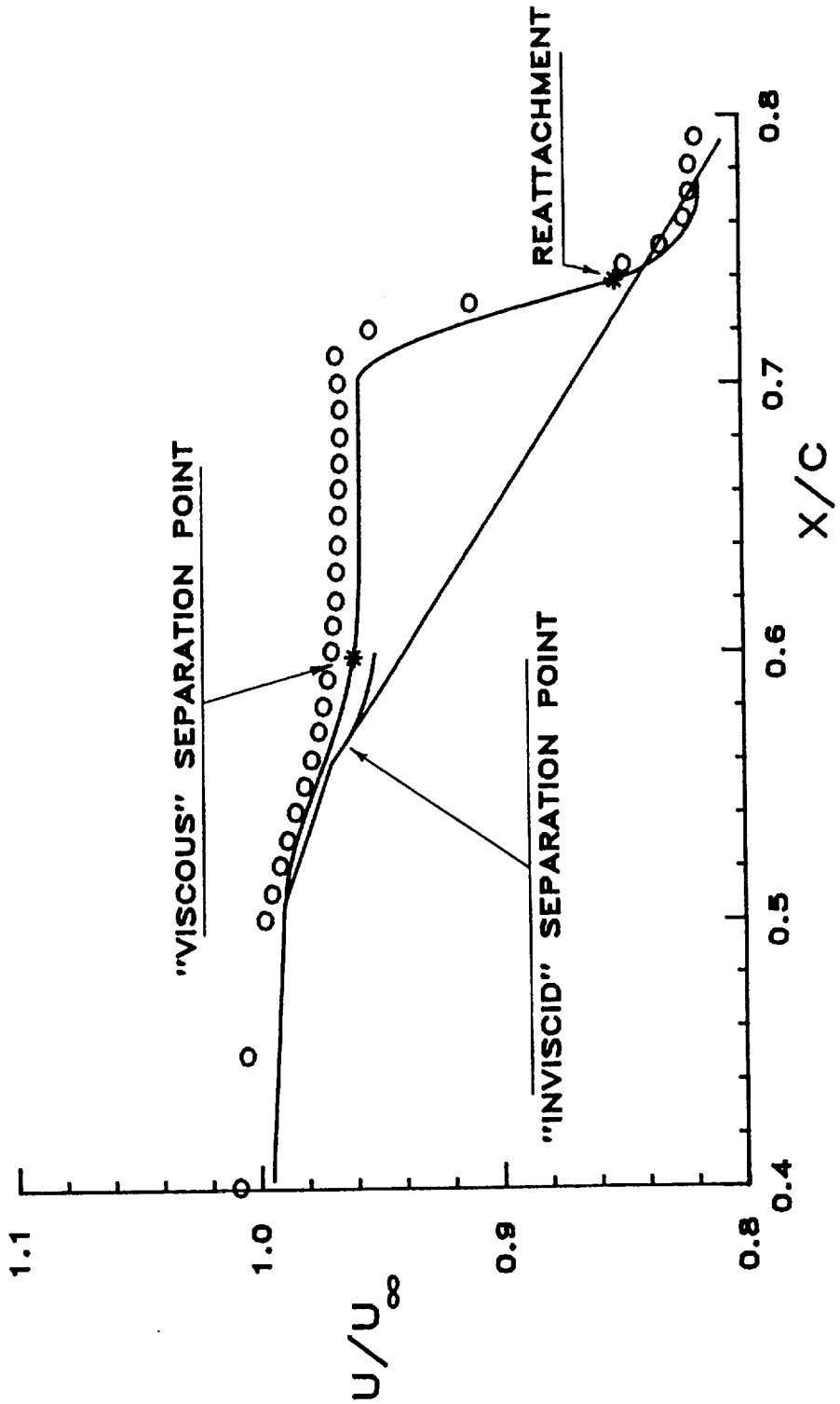

Fig. 3-5 Close-up of the laminar separation region demonstrating the removal of the Goldstein singularity.

range of values, from as low as 2 up to 30 for the range of bubbles examined, and their average does not give the model enough flexibility. Eq. (3.18), on the other hand, gives the correct scaling for this variable. In addition, very similar values for B as given by Eq. (3.18) have been reported by Pauley et al. [1988] in their Navier-Stokes simulation. Eq. (3.18), therefore, has been included into the model.

Chapter 4

TRANSITION

The prediction of the transition location inside the bubble has received a great deal of attention since the very first models. In fact, both the drag increment due to the bubble as well as the bursting behavior depend strongly on the location where the calculations switch in a more or less gradual way from laminar to turbulent flow. Although it has been claimed that the length of the transition region inside the bubble must be modelled accurately [Walker, 1989], a point-transition has been found to work very well in the present model. In this chapter, a few empirical transition criteria are discussed together with the method employed in the model.

Empirical Criteria

Ever since bubbles were first observed, many researchers have looked for an empirical correlation between the distance from separation to transition and local bubble characteristics such as conditions at separation. Since it was observed that the length of the bubble is inversely proportional to the Reynolds number, the first transition criterion, proposed by Von Doenhoff [1938], assumed a constant Reynolds number based on the velocity at separation and the distance between separation and transition,

$$R_{\ell_1} = \frac{U_S \ell_1}{\nu} = 50,000 \tag{4.1}$$

As the Reynolds number increases, U_S usually increases, too, such that this criterion forces the laminar length to decrease in size. Horton [1967], thirty years later, used a value of 40,000. This expression can be rearranged as

$$\frac{\ell_1}{c} = \left[\frac{40,000}{(R_{\delta_2})_S}\right] \frac{(\delta_2)_S}{c} \tag{4.2}$$

O'Meara and Mueller [1986] took an experimental mean from many sets of data as

$$\frac{\ell_1}{c} = 155\frac{(\delta_2)_S}{c} \tag{4.3}$$

which is a less general relationship. As pointed out by Schmidt and Mueller [1989], these relationships cannot capture the vanishing of the bubble at the experimentally reported value [Crabtree, 1957] of momentum thickness Reynolds number at separation of about 750, over which transition precedes laminar separation. Schmidt and Mueller describe how the correlation developed by Vincent de Paul [1972] is able to capture this effect by allowing a variable R_{ℓ_1}. Similarly, based on the same data sets used by O'Meara and Mueller, Schmidt and Mueller propose the following criterion,

$$\frac{\ell_1}{c} = \begin{cases} [513 - 3.7820(R_{\delta_2})_S]\frac{(\delta_2)_S}{c}, & 27 < (R_{\delta_2})_S < 72 \\ [267 - 0.3709(R_{\delta_2})_S]\frac{(\delta_2)_S}{c}, & 72 < (R_{\delta_2})_S < 720 \end{cases} \tag{4.4}$$

such that the bubble length vanishes at values of $(R_{\delta_2})_S > 720$. Fig. 4-1 shows this criterion in graphical form together with Eq. (4.3). Since Eq. (4.3) does not incorporate any dependence on $(R_{\delta_2})_S$, it is shown in the figure as a plane whose projection onto the $(\delta_2)_S/c$-ℓ_1/c plane is simply a straight line through the origin.

While it is true that the Reynolds number has a strong influence on the transition length, and therefore on the overall length, of separation bubbles, this effect is reflected in many of these correlations in a rather coarse way. The correlations for which the transition length is proportional to the value of momentum thickness at separation better predict the length of leading-edge bubbles due to a spurious coincidence. For airfoil flows, in fact, small values of $(\delta_2)_S$ correspond to leading-edge bubbles, which form on large suction peaks near the stagnation point and are usually quite short. Larger values of $(\delta_2)_S$ are usually associated with mid-chord bubbles that occur far downstream of the stagnation point and are usually much longer. Fig. 4-2 illustrates this effect, where the isolated points are leading-edge

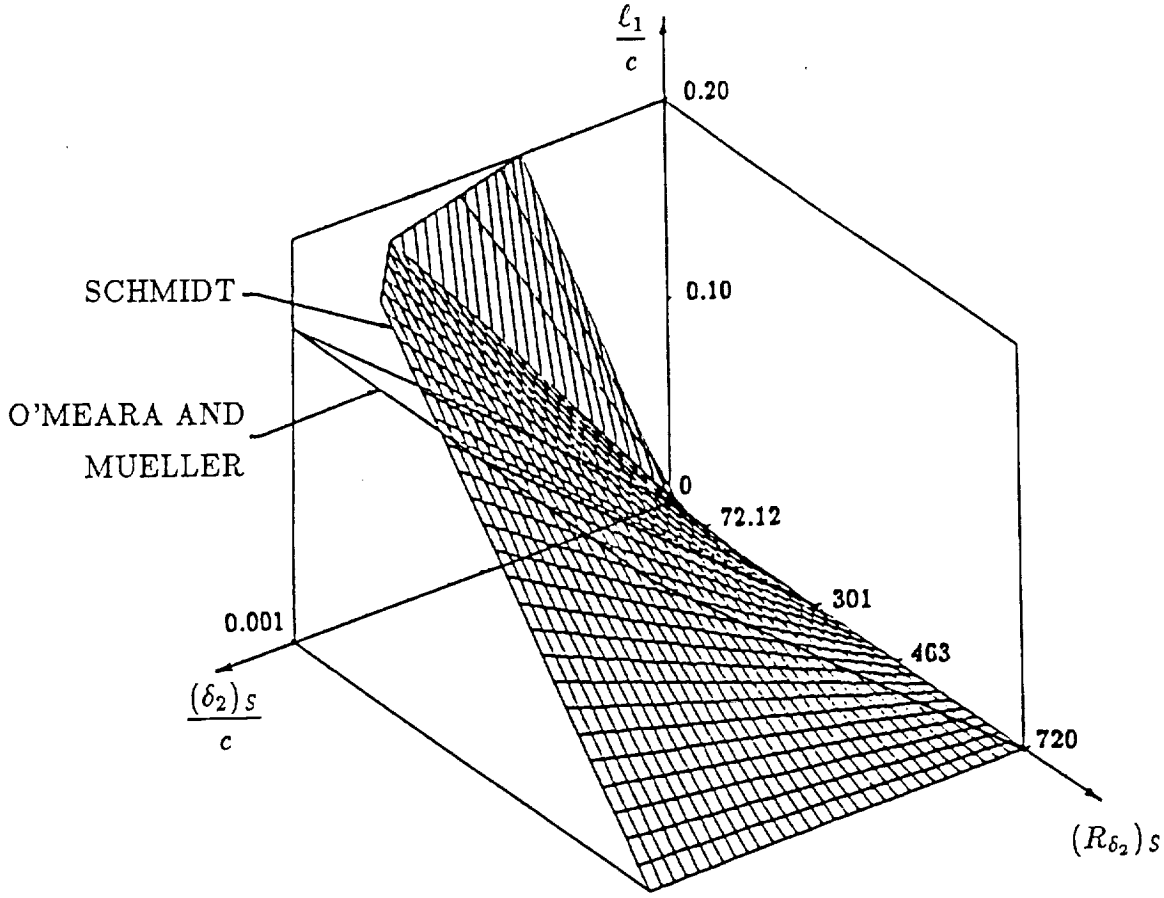

Fig. 4-1 Comparison of two empirically derived transition correlations for the separated laminar shear layer.

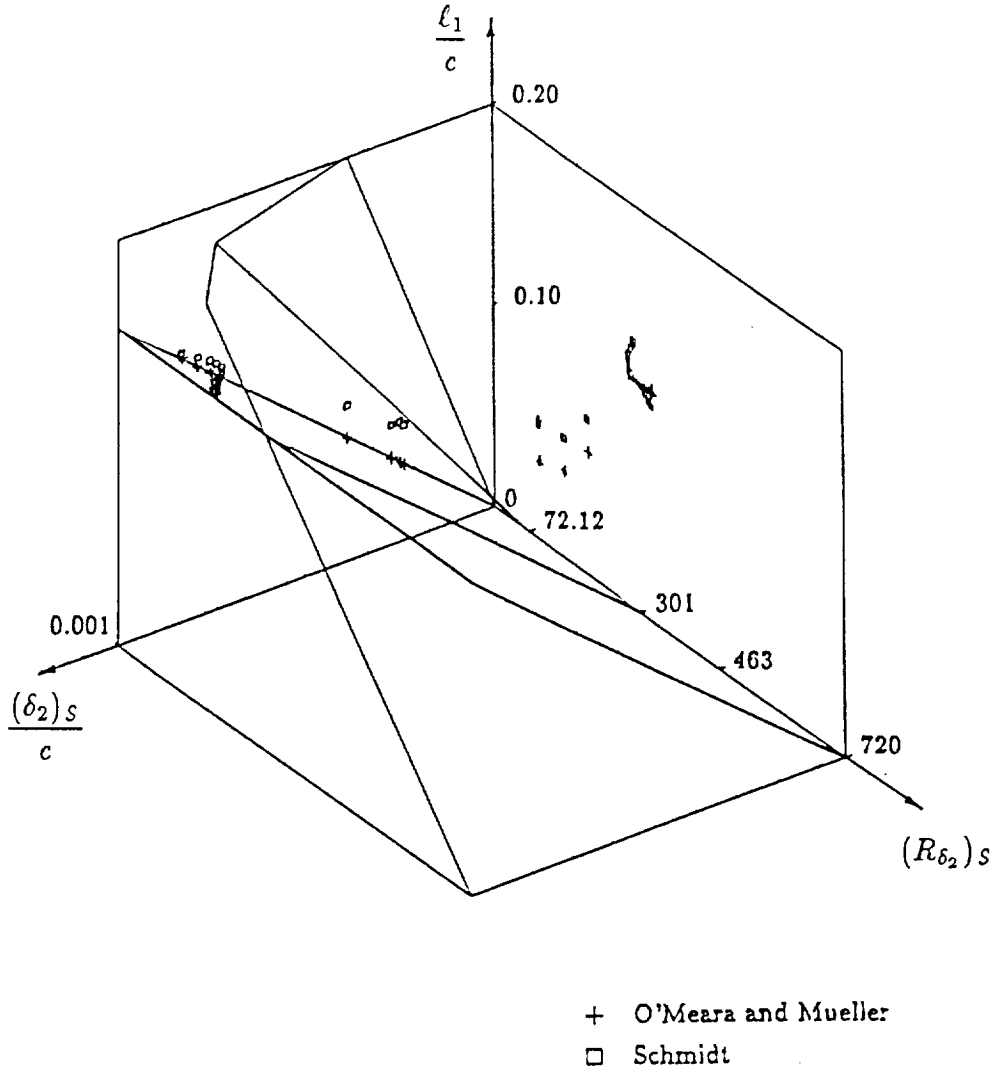

Fig. 4-2 Comparison of the laminar lengths predicted by the two correlations for the Eppler E387 airfoil at $R = 300,000$.

bubbles. The value of $(\delta_2)_S$, however, does not in itself contain any information about the stability of the separating shear layer. In fact, no empirical criterion developed so far can capture the effects of a variable pressure distribution. Specifically, no local criterion can capture the vanishing of the upper-surface mid-chord bubble with increasing angle of attack.

Eppler's Transition Criterion

Given the success of Eppler's transition criterion in predicting the transition location in attached boundary layers, it was thought that it should be possible to extend such a criterion to separated boundary layers. Whereas the criteria described above seek a correlation between transition in the free shear layer and conditions at separation, which is at a different location on the airfoil, Eppler's criterion is based on the local characteristics of the boundary layer. Since, unlike in the early bubble models, the boundary layer development here is calculated also downstream of separation, it seemed that monitoring the development at each downstream increment would naturally lead to a more accurate transition prediction. In order to better explain how Eppler's criterion is implemented, Eppler's boundary-layer development plot should be described.

Integration of the momentum and energy integral equations gives the values of δ_2 and δ_3 at each downstream station. The shape factor $H_{32} = \delta_3/\delta_2$ is therefore also known. Since the inviscid velocity along the airfoil is taken as the boundary-layer edge velocity that drives the boundary-layer development, U and δ_2 at each downstream station can be grouped to obtain the development of R_{δ_2}. Eppler connects subsequent (H_{32}, R_{δ_2})-pairs on a plot whose axes measure the variation in these two variables, thereby describing the boundary-layer development from the stagnation point to the trailing edge in a very concise way. The stagnation point occurs at a value of $H_{32} = 1.62$ and R_{δ_2} approximately equal to 10. Values of

$R_{\delta_2} < 10$ are not plotted. Fig. 4-3 shows a typical boundary-layer development. Following the upper surface development given by the solid line, laminar separation is encountered when $H_{32} = 1.515095$. This criterion is shown on the plot as a vertical dotted line. From the laminar separation point, H_{32} starts growing again until transition is met. While H_{32} grows monotonically inside the laminar part of the bubble with downstream distance from laminar separation, R_{δ_2} stays approximately constant. A very similar criterion to Eq. (4.4) can therefore be constructed by correlating the value of H_{32} at transition to $(R_{\delta_2})_S$. The particular transition criterion for separated shear layers shown in this figure as a family of cubics introduces an additional dependence on P. Thus, while the bubble is seen to disappear at values of $(R_{\delta_2})_S > 875$, for smaller values $(H_{32})_T$ increases with decreasing P. This trend in $(H_{32})_T$ does not necessarily imply a similar trend in laminar length since the rate of growth of H_{32} depends on the pressure distribution in the laminar part of the bubble. Although unsuccessful, this and similar criteria served to illustrate how poorly $(H_{32})_T$ correlates to local bubble conditions incorporated in parameters such as P and $(R_{\delta_2})_S$. In fact, while any one particular bubble could be matched quite easily with a criterion as shown in the figure, any such criterion was consistently found of very limited generality. Downstream of transition, the turbulent shear layer growth causes H_{32} to decrease again to a value at reattachment which is weakly dependent on the local momentum thickness Reynolds number and always close to 1.51. The attached turbulent boundary-layer development causes H_{32} to increase again toward the flat-plate fully developed value of 1.77. As the trailing edge is approached, the adverse pressure gradient drives the boundary layer toward turbulent separation which occurs at $H_{32} = 1.46$ for Eppler's method and $H_{32} = 1.51$ for Drela's method, which will be discussed in the next chapter.

In the course of these investigations, it was found that the curve corresponding

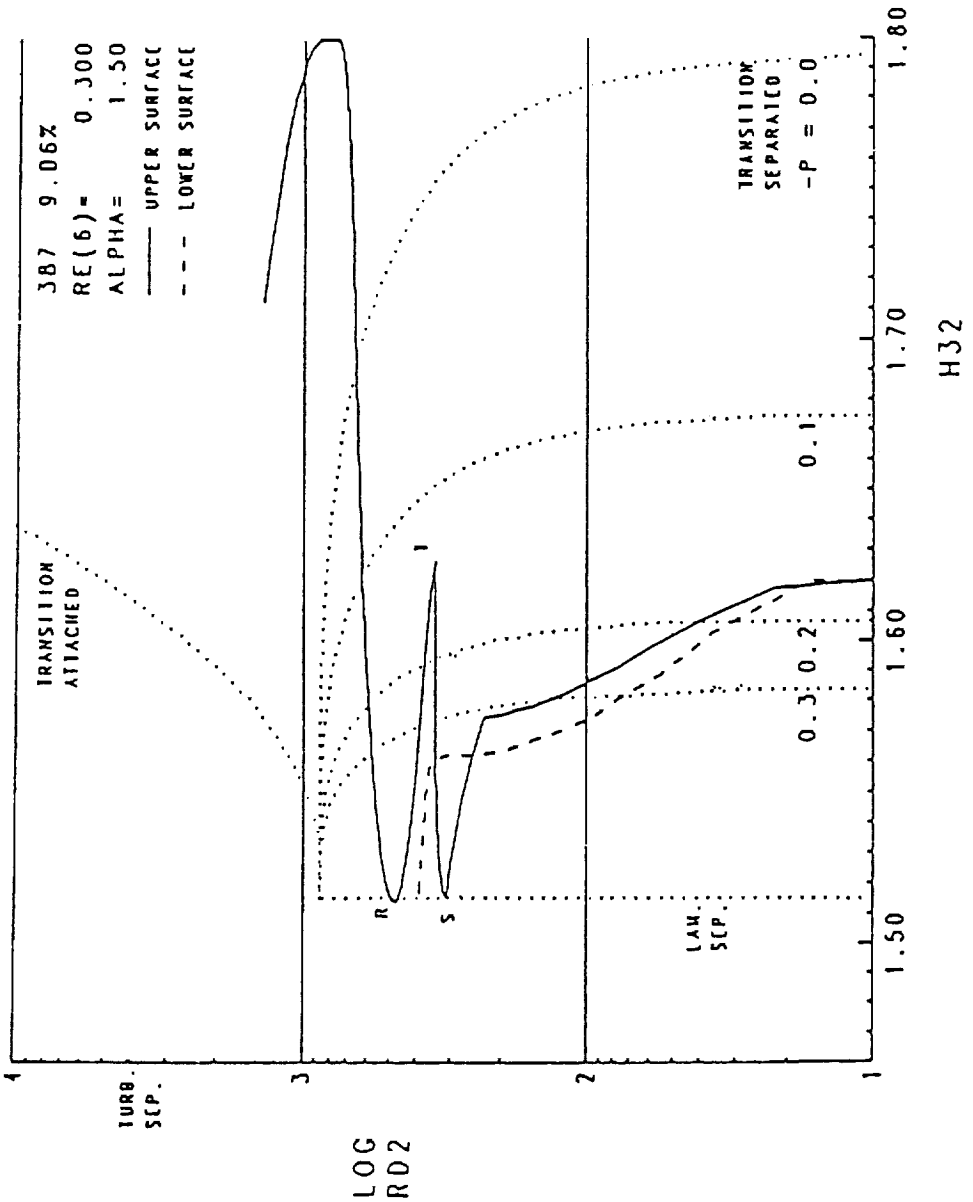

Fig. 4-3 Modified Eppler boundary-layer development plot showing the shear layer development inside the bubble.

to attached transition will cause natural transition to be predicted in many cases where a bubble is actually present. This happens because the value of Reynolds number at which transition precedes laminar separation can be quite high. In fact, it can be higher than the value of 720 proposed by Schmidt and Mueller. Eppler's original transition criterion [Eppler, 1963], not shown, intersected the laminar separation line at $R_{\delta_2} = 463$. Based on additional measurements, Eppler [1989] has modified the criterion to

$$[\ln R_{\delta_2}]_T \geq -21.74 + 18.4H_{32} + 125(H_{32} - 1.573)^2 \tag{4.5}$$

where now the intersection occurs at $R_{\delta_2} = 704$. For such a value, however, transition is still predicted too soon when the boundary layer is near separation. In order to be able to compare bubbles forming on airfoils at chord Reynolds numbers of one million or greater, approximately, the 125 in Eq. (4.5) is replaced with 190. This leads to a value at the intersection of $R_{\delta_2} = 875$, which seems to work well. This apparent coarseness in Eppler's criterion is due to its having been calibrated mainly from airfoil drag coefficient data rather than from a modelling of the actual transition process. The reason why transition is predicted instead of a bubble at high chord Reynolds numbers is simply that at such values the bubble does not cause any significant drag increase; in fact, it usually causes the same increase in momentum thickness that is given by the attached turbulent boundary layer over its length.

In an attempt to reconcile Eppler's transition criterion with another very successful transition prediction method, the e^n method, they are plotted together in Fig. 4-4. In the e^n method, a value of $n = 9$ has been found to correspond to observed transition locations in many different flows. Rather than using Eppler's boundary-layer development plot, this comparison is done here on a plot of R_{δ_2} *vs.* H_{12} in order to include several measurements of these variables at observed

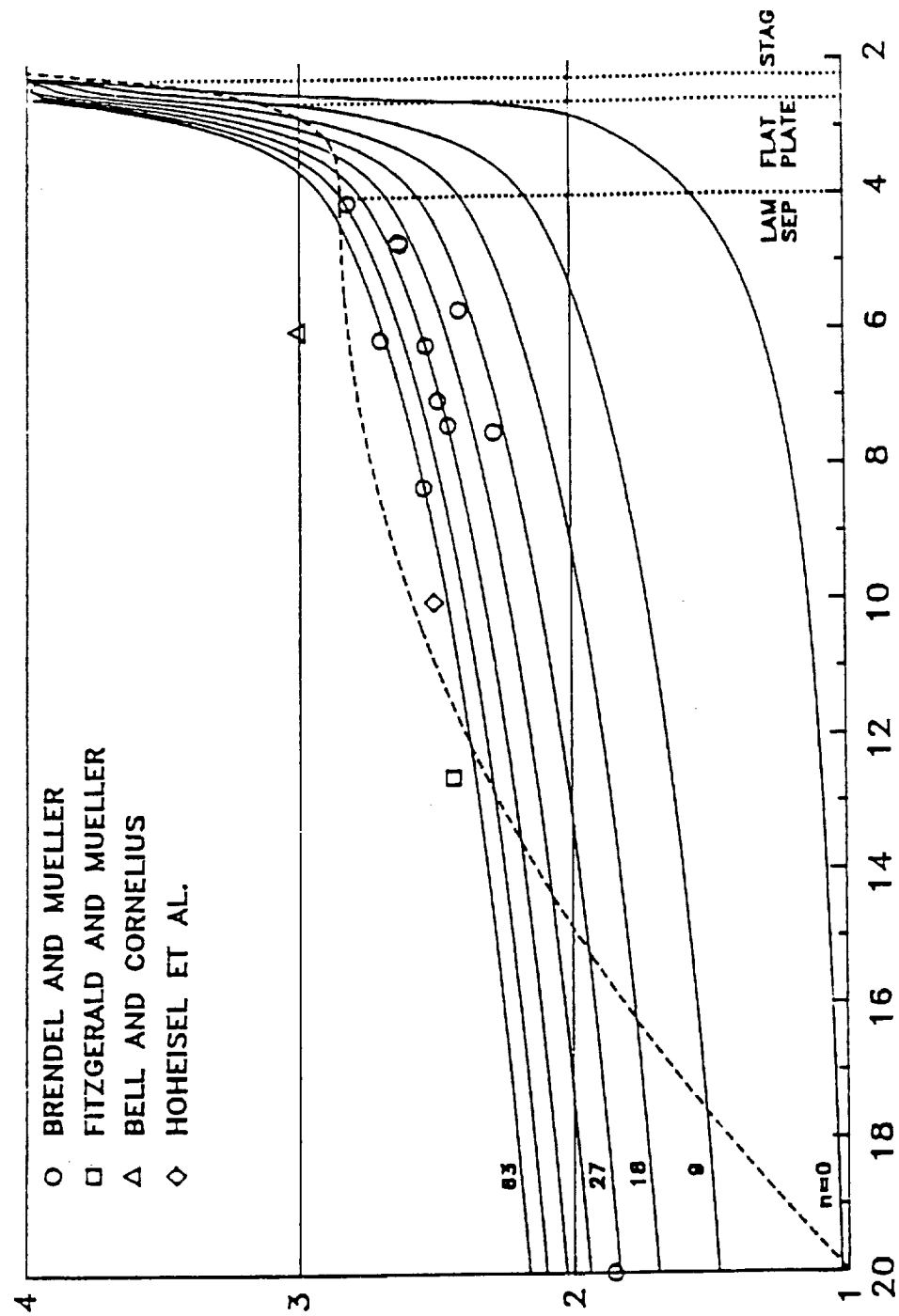

Fig. 4-4 Comparison of Eppler's transition criterion with the amplification surface for self-similar profiles. Dashed line for $H_{12} < 4$ is Eppler's transition criterion for attached flow; dashed line for $H_{12} > 4$ is one of the attempted criteria for separated flow.

transition locations. This comparison was attempted also because, since the e^n method can predict transition successfully in a separated shear layer, it was hoped that a suitable criterion for use in the boundary-layer development plot could be inferred from it. In this figure, contours of constant n are given for the Falkner-Skan self-similar developments [Schlichting, 1979]. For such developments, in fact, a unique surface exists that allows the determination of the value of n from the local values of the momentum thickness Reynolds number and shape factor alone. The equation defining this surface was developed by Drela [1986] and will be discussed below. Shown in this figure is Eppler's transition criterion for attached boundary layers as well as one of the attempted criteria for separated flow. It is interesting that Eppler's curve falls quite close to the $n = 9$ contour, for zero-pressure gradient flow ($H_{12} = 2.59$). As can be seen from the wide scatter in the experimental data, however, it seems dubious that a single curve could capture the correct transition location inside the bubble with any generality. In fact, the growth of n in a non-similar boundary layer development will not follow the surface whose contours are shown in the figure, regardless of whether the flow is attached or separated. This implies that transition is not dependent solely on the local boundary-layer characteristics but depends also on the manner in which the boundary layer arrives at such values. The inclusion of path-dependency, or the effect of upstream boundary-layer development on transition, has captured the generality that the transition criteria discussed so far lack In order to fully understand why, the e^n method will now be discussed in detail.

The e^n Method

The e^n semi-empirical transition prediction method, developed thirty years ago [van Ingen, 1956; Smith and Gamberoni, 1956] and since successfully applied to a variety of aerodynamic flows, relies on a theory that can explain the moderate

success of some of the correlations described above, that can correctly distinguish between leading-edge and mid-chord bubbles, and that can correctly model the effects of variations in pressure distribution upstream of the bubble. Linear stability theory, in fact, directly models the growth of instabilities in a boundary layer while indirectly, through the boundary-layer development, accounting for the effects of Reynolds number. $n(s)$ is defined as the logarithm of the ratio of disturbance amplitude at station s to its amplitude at neutral stability, s_0. Transition is assumed to take place when n reaches a value previously correlated to experimentally observed transition locations. For similar flow environments this value has been reported to lie around 9 by many researchers, although it appears to depend on Reynolds number [Evangelista and Vemuru, 1989; Horstmann et al., 1990].

It is generally accepted that linear stability theory correctly models the transition process for approximately 70% of the distance between neutral stability ($n = 0$) and fully turbulent flow. The actual "transition region," however, is usually defined as the region between the first appearance of turbulent spots and fully turbulent flow [Arnal, 1984], or the last 30% of this distance. In order to approximate the transition process in the nonlinear amplification region, an intermittency function is usually employed at a value close to $n = 8$. Equally often, transition is taken to be completed when $n = 9 - 14$ and the turbulent calculations are started abruptly at the corresponding streamwise station. In both cases, significant empirical input is necessary to render the method usable. Another concern associated with this method is that the amplitude of the disturbance at neutral stability is unknown. The inability of the method to model directly the influence of the turbulence intensity of the oncoming air and surface conditions on the onset of transition forces the use of further empirical corrections [Mack, 1977]. In spite of these weaknesses, the e^n method remains the engineering transition prediction method most faithful

to the actual physical process.

The e^n method is based on the numerical solution of the Orr-Sommerfeld equation which is derived from the Navier-Stokes equations as follows. The two-dimensional Navier-Stokes equations are perturbed and linearized. An assumption of locally parallel mean flow is made. Subtracting the mean flow, a system of three partial differential equations for the perturbation field is obtained. Since the coefficients are functions only of y, the method of normal modes can be applied in the particular form

$$v'(x,y,t) = \mathrm{Re}\left[\hat{v}(y)e^{i(\alpha^* x - \omega^* t)}\right] \tag{4.6}$$

which implicitly assumes a sinusoidal disturbance. Here v' is the disturbance in the y-direction. Similar expressions are assumed for u' and p'. α^* is the wavenumber and ω^* the radian frequency, which can be nondimensionalized with respect to a reference length and velocity,

$$\begin{aligned} \alpha &= \alpha^* L_{ref} \\ \omega &= \frac{\omega^* L_{ref}}{U_{ref}} \end{aligned} \tag{4.7}$$

Substitution of these expressions into the partial differential equations for the disturbance field results in a set of three ordinary differential equations for the disturbances. Eliminating $\hat{u}'$ and $\hat{p}'$ in favor of $\hat{v}'$, the Orr-Sommerfeld equation is obtained,

$$\hat{v}'''' + [-iR(\alpha U - \omega) - 2\alpha^2]\hat{v}'' + [iR(\alpha U - \omega)\alpha^2 + iRU''\alpha + \alpha^4]\hat{v} = 0 \tag{4.8}$$

α and ω are, in general, both complex. Although the derivation and the analysis are performed in the complex plane, it is understood that physical quantities are obtained by taking the real part of any of the complex variables employed.

Two limiting cases of interest are

$$\begin{cases} \alpha = \alpha_r, \quad \omega = \omega_r + i\omega_i & \text{temporal instability} \\ \alpha = \alpha_r + i\alpha_i, \quad \omega = \omega_r & \text{spatial instability} \end{cases} \tag{4.9}$$

To calculate the amplification of disturbances as the boundary layer develops, a spatial instability analysis is necessary. Thus, the Reynolds number and the frequency are specified and the wavenumber is found by solving numerically the Orr-Sommerfeld equation subject to the boundary conditions

$$v' = \frac{dv'}{dy} = 0 \qquad \text{at} \quad y = 0 \quad \text{and as} \quad y \to \infty \tag{4.10}$$

The homogeneous boundary conditions imply the existence of an infinity of solutions or eigenvalues α. The value of greatest physical interest is the eigenvalue for which $-\alpha_i$ is largest. This can be seen from the expression for the fluctuation,

$$\begin{aligned} v' &= \hat{v}(y) e^{i[(\alpha_r^* + i\alpha_i^*)x - \omega_r^* t]} \\ &= [\hat{v}(y) e^{-\alpha_i^* x}] e^{i(\alpha_r^* x - \omega_r^* t)} \end{aligned} \tag{4.11}$$

where $\hat{v}(y)$ is the distribution of the disturbance amplitude (eigenfunction) and the bracketed term is the amplitude of the disturbance at a distance x from some reference point. The ratio between this term evaluated at two different x-locations represents the amplification of a disturbance between them. Assuming a boundary layer developing in zero pressure gradient,

$$\frac{A_2}{A_1} = \frac{\hat{v}(y) e^{-\alpha_i^* x_2}}{\hat{v}(y) e^{-\alpha_i^* x_1}} = e^{-\alpha_i^* (x_2 - x_1)} \tag{4.12}$$

The amplification factor, n, is defined as the logarithm of this ratio,

$$n = \ln\left(\frac{A_2}{A_1}\right) = -\alpha_i^* (x_2 - x_1) \tag{4.13}$$

The amplification factor is thus equal to the area under the amplification rate curve. In this case, this curve is a constant because the parallel flow approximation and the absence of a pressure gradient prevent any change in the local Reynolds number such as, for instance, R_{δ_2}.

The continuous wavelength modulation encountered by a fixed-frequency disturbance travelling downstream in a developing boundary layer is approximated

locally by a series of constant-wavelength plateaus, obtained by solving the Orr-Sommerfeld equation for a sequence of parallel mean flows of different thicknesses and at different pressure gradients, each characterizable by a different value of R_{δ_2} and H_{12}. As the streamwise extent of the plateaus tends to zero, Eq. (4.13) can be generalized to

$$n = \int_{x_1}^{x_2} -\alpha_i^* \, dx \tag{4.14}$$

As a measure of how far from transition a boundary layer is, it is preferred to calculate the total amplification that has occurred: the amplification, that is, from the lower branch of the neutral curve,

$$n(s) = \int_{s_0}^{s} -\alpha_i^* \, ds \tag{4.15}$$

where the independent variable is again s, the distance along the airfoil from the front stagnation point.

In general, the disturbance environment in a wind tunnel or in free flight does not consist of a single-frequency pressure pulse but, rather, of broad-band or white noise. The boundary layer simply amplifies those frequencies that, at a specific local Reynolds number, correspond to what in simpler dynamical systems is called the natural frequency. Since the local boundary-layer Reynolds number changes with downstream distance, different frequencies are amplified as the boundary layer develops. This necessitates the tracking of several different frequencies at the same time, with the first that reaches $n = 9$ indicating transition.

As the frequencies amplified in the separated shear layer may be different from those upstream of separation, it may not be necessary to monitor the stability of the laminar boundary layer upstream of separation. The fact that some frequencies may come close to $n = 9$ upstream of separation does not necessarily imply that transition will occur sooner once the boundary layer separates. If this is true,

then it should be possible to devise a transition criterion based solely on local information, for instance on conditions at laminar separation. The consistent failure of all previous such criteria would still not be sufficient proof of the untenability of this hypothesis.

Drela's Approximate e^n Method

While the questions raised above need further study, for the present time the approximation to the e^n method developed by Drela [1986] has been implemented in the Eppler and Somers program. In order to demonstrate that this method introduces an error in the calculation of n over and above its declared approximations, it is now discussed in some detail.

Rather than performing a linear stability analysis of the boundary-layer velocity distribution as can be obtained, for instance, from a finite-difference method at each downstream station, following Gleyzes et al. [1983] Drela computes a data base of the stability characteristics of the Falkner-Skan profiles that can be "tapped" during a boundary-layer calculation using the local shape factor as the coupling parameter. More precisely, the nondimensional growth rate, $-\alpha_i$, corresponding to a particular value of the local shape factor of a Falkner-Skan profile and of the local Reynolds number is divided by the local boundary-layer characteristic thickness, i.e. δ_2, to obtain the physical growth rate to be used in the integral (4.15). Given that the correct characteristic thickness is obtained independently, from the momentum integral equation, the manner in which the nondimensional data base is generated is of no consequence. The most convenient way is to calculate the growth rates for self-similar developments at constant H_{12} values and increasing R_{δ_2}. Starting from the Orr-Sommerfeld spatial instability analysis of the Falkner-Skan profiles at many different values of H_{12}, a set of neutral curves is generated, one for each value of shape factor. An example of these neutral curves is shown in Fig. 4-5 for two values

of H_{12}. For each value of shape factor, the dimensionless amplification rate, $-\alpha_i$, is evaluated along rays of constant reduced frequency,

$$F = \frac{2\pi f \nu}{U^2} \tag{4.16}$$

to form curves $-\alpha_i(H_{12}, R_{\delta_2}, F)$. From these curves the amplification factor for the devclopment of each Falkner-Skan profile is found from

$$\begin{aligned} n(H_{12}, R_{\delta_2}, F) &= \int_{s_0}^{s} -\alpha_i^* ds \\ &= \int_{R_{\delta_2 0}}^{R_{\delta_2}} \frac{-\alpha_i^*}{\frac{dR_{\delta_2}}{ds}} dR_{\delta_2} \end{aligned} \tag{4.17}$$

For a Falkner-Skan profile,

$$R_{\delta_2} = \frac{U\delta_2}{\nu} = \frac{U}{\nu}\left[\left(\frac{2}{1+m}\frac{\nu s}{U}\right)^{\frac{1}{2}} \int_0^{\infty} f'(1-f')d\eta\right] \tag{4.18}$$

where m is constant and defined as

$$m = \frac{s}{U}\frac{dU}{ds} \tag{4.19}$$

Denoting the momentum-thickness integral (not a function of s) by I,

$$R_{\delta_2} = \left(\frac{2}{1+m}\frac{Us}{\nu}\right)^{\frac{1}{2}} I \tag{4.20}$$

Thus,

$$\begin{aligned} \frac{dR_{\delta_2}}{ds} &= I\left(\frac{2}{1+m}\right)^{\frac{1}{2}}\left[\frac{1}{2}\left(\frac{U}{\nu s}\right)^{\frac{1}{2}} + \frac{1}{2}\left(\frac{s}{\nu U}\right)^{\frac{1}{2}}\frac{dU}{ds}\right] \\ &= \frac{1}{2}I\left(\frac{2}{1+m}\frac{U}{\nu s}\right)^{\frac{1}{2}}\left[1 + \frac{s}{U}\frac{dU}{ds}\right] \\ &= I\left(\frac{2}{1+m}\frac{U}{\nu s}\right)^{\frac{1}{2}}\frac{1+m}{2} \\ &= \left[\left(\frac{1+m}{2}\frac{U}{\nu s}\right)^{\frac{1}{2}}\frac{1}{I}\right] I^2 \\ &= \frac{I^2}{\delta_2} \end{aligned} \tag{4.21}$$

Thus, Equation (4.17) becomes,

$$n(H_{12}, R_{\delta_2}, F) = \frac{1}{I^2} \int_{R_{\delta_{2_0}}}^{R_{\delta_2}} -(\alpha_i^* \delta_2)\, dR_{\delta_2}$$

$$= \frac{1}{[I(H_{12})]^2} \int_{R_{\delta_{2_0}}}^{R_{\delta_2}} -\alpha_i(H_{12}, F)\, dR_{\delta_2} \tag{4.22}$$

In this way, the original dimensionless eigenvalues of the dimensionless Orr-Sommerfeld equation can be used to find n, which is defined in terms of a dimensional wave number and distance. This can be done for a self-similar profile since dR_{δ_2}/ds assumes the particular form shown.

The curves obtained with this integral for different frequencies and at a constant H_{12} are shown in Fig. 4-6. Drela takes the envelope as a straight line as done by Gleyzes et al. [1983]. This leads to the following expression for the amplification surface for self-similar developments,

$$n(R_{\delta_2}, H_{12}) = \left[\frac{dn}{dR_{\delta_2}}(H_{12})\right]^e [R_{\delta_2} - R_{\delta_{2_0}}(H_{12})] \tag{4.23}$$

where the superscript "e" denotes a value obtained from the envelope of amplified frequencies and

$$\left[\frac{dn}{dR_{\delta_2}}(H_{12})\right]^e = 0.01[\{2.4H_{12} - 3.7$$

$$+ 2.5\tanh[1.5(H_{12} - 3.1)]\}^2 + 0.25]^{\frac{1}{2}} \tag{4.24}$$

$$\log_{10}[R_{\delta_{2_0}}(H_{12})] = \left[\frac{1.415}{H_{12} - 1} - 0.489\right] \tanh\left[\frac{20}{H_{12} - 1} - 12.9\right]$$

$$+ \frac{3.295}{H_{12} - 1} + 0.440 \tag{4.25}$$

While Gleyzes et al. then evaluate the amplification integral as

$$n(s) = \int_{R_{\delta_{2_0}}}^{R_{\delta_2}(s)} \left[\frac{dn}{dR_{\delta_2}}(H_{12})\right]^e dR_{\delta_2} \tag{4.26}$$

Drela changes the variable of integration back to s,

$$n(s) = \int_{s_0}^{s} \left[\frac{dn}{dR_{\delta_2}}(H_{12}) \right]^e \frac{dR_{\delta_2}}{ds} ds \tag{4.27}$$

At this point, Drela finds an expression for dR_{δ_2}/ds in a rather roundabout way.

$$\begin{aligned}
\frac{d}{ds}\left(\frac{U\delta_2}{\nu}\right) &= \frac{\delta_2}{\nu}\frac{dU}{ds} + \frac{U}{\nu}\frac{d\delta_2}{ds} \\
&= \frac{1}{2}\frac{s}{U}\frac{dU}{ds}\frac{U\delta_2}{\nu s} + \frac{U}{\nu}\frac{d\delta_2}{ds} + \frac{1}{2}\frac{\delta_2}{\nu}\frac{dU}{ds} \\
&= \frac{1}{2}\left[\frac{s}{U}\frac{dU}{ds} + 2\frac{\nu s}{U\delta_2}\left(\frac{U}{\nu}\frac{d\delta_2}{ds} + \frac{1}{2}\frac{\delta_2}{\nu}\frac{dU}{ds}\right)\right]\frac{U\delta_2^2}{\nu s}\frac{1}{\delta_2}
\end{aligned} \tag{4.28}$$

He shows that dR_{δ_2}/ds equals this last expression with a 1 in place of the second term inside the square bracket. If this is taken as a condition, the resulting differential equation can be integrated as follows,

$$\begin{aligned}
2\frac{\nu s}{U\delta_2}\left(\frac{U}{\nu}\frac{d\delta_2}{ds} + \frac{1}{2}\frac{\delta_2}{\nu}\frac{dU}{ds}\right) &= 1 \\
2\frac{s}{\delta_2}\frac{d\delta_2}{ds} + \frac{s}{U}\frac{dU}{ds} &= 1 \\
s\left[2\frac{d}{ds}(\ln\delta_2) + \frac{d}{ds}(\ln U)\right] &= 1 \\
s\frac{d}{ds}\left[\ln(\delta_2^2 U)\right] &= 1 \\
d[\ln(\delta_2^2 U)] &= \frac{ds}{s} \\
\ln(\delta_2^2 U) &= \ln s + C \\
\delta_2^2 U &= Cs \\
\delta_2 &= C\sqrt{\frac{s}{U}}
\end{aligned} \tag{4.29}$$

Thus, the functional form characteristic of Falkner-Skan profiles is recovered, where the constant is in general a function of the shape factor. Drela now introduces the two "empirical relations" (given in the Appendix),

$$\frac{s}{U}\frac{dU}{ds} = m(H_{12}) \tag{4.30}$$

$$\frac{U\delta_2^2}{\nu s} = \ell(H_{12}) \tag{4.31}$$

What he means is "analytical correlations from the Falkner-Skan profiles." Since he is using these profiles here and since his form for dR_{δ_2}/ds indeed implies the assumption of a Falkner-Skan δ_2-growth, it is not clear why he did not simply substitute the Falkner-Skan expression for $\delta_2(s)$ directly into his expression for dR_{δ_2}/ds, Eq. (4.28),

$$\begin{aligned}\frac{dR_{\delta_2}}{ds} &= \frac{1}{2}\left[\frac{s}{U}\frac{dU}{ds}+1\right]\frac{U\delta_2^2}{\nu s}\frac{1}{\delta_2} \\ &= \frac{1}{2}(m+1)\frac{U}{\nu s}\left[\left(\frac{2}{1+m}\frac{\nu s}{U}\right)^{\frac{1}{2}}\int_0^\infty f'(1-f')d\eta\right]^2\frac{1}{\delta_2} \\ &= \frac{I^2}{\delta_2} \qquad (4.32)\end{aligned}$$

which is identical to Eq. (4.21). Thus, Drela only had to curve-fit $I(H_{12})$.

Having established that

$$\frac{m(H_{12})+1}{2}\ell(H_{12}) = [I(H_{12})]^2 \qquad (4.33)$$

Drela's integral for evaluating $n(s)$,

$$n(s) = \int_{s_0}^{s}\left[\frac{dn}{dR_{\delta_2}}(H_{12})\right]^e \frac{m(H_{12})+1}{2}\frac{\ell(H_{12})}{\delta_2(s)}ds \qquad (4.34)$$

can be written, using Eqs. (4.17), (4.21), (4.26), and (4.33),

$$n(s) = \int_{s_0}^{s}\left[\frac{-\alpha_i^*}{\frac{I^2}{\delta_2}}\right]^e \frac{I^2}{\delta_2(s)}ds \qquad (4.35)$$

where $\delta_2(s)$ comes from the non-similar boundary-layer development as calculated by the momentum and energy integral equations. Thus,

$$n(s) = \int_{s_0}^{s}\frac{[-\alpha_i^*\delta_2]^e}{\delta_2(s)}ds \qquad (4.36)$$

$$= \int_{s_0}^{s}\frac{[-\alpha_i]^e}{\delta_2(s)}ds \qquad (4.37)$$

Which is identical to the expression used by Stock and Degenhart except for the use of an envelope to find α_i. Using $\delta_2(s)$ as calculated by the governing equations is precisely what enables the method to account for upstream history on the growth of n. That is, the dimensionless growth rate $-\alpha_i$ obtained at each downstream station from the value of H_{12} and R_{δ_2} is divided by the local boundary-layer momentum thickness which is in general *different* from the value in a self-similar development at the same value of H_{12} and R_{δ_2}.

The Envelope Error

In collaboration with Selig [1990], the author found that, even if Drela had used the actual envelope of the amplification curves instead of approximating it with a straight line, his $n(s)$-development would not correspond to the true envelope of the amplification curves at constant frequency along the airfoil surface. The error arises whenever the boundary-layer development is non-similar. To see this, it is necessary to rely on a numerical example, since the functions in question are not known analytically but are obtained numerically. Thus, it is helpful to envision a fictitious boundary-layer development made up of two constant-H_{12} lengths with a discontinuous jump in between. Fig. 4-5 shows the neutral curves corresponding to the two values of shape factor. It is desired to compare the growth of n obtained by following the development through the jump in H_{12} at constant frequency to that obtained using Drela's envelope. Fig. 4-6 shows the amplification curves for the three reduced frequencies shown on the neutral curves plot as calculated by Eq. (4.22) together with the envelopes given by Eqs. (4.23)-(4.25) for the two values of H_{12}. Fig. 4-7 shows the n-growth along the boundary layer with the switch in shape factor occurring at $R_{\delta_2} = 500$.

The three frequencies selected represent limiting cases that serve best to elucidate the argument. Referring to Fig. 4-7, as R_{δ_2} increases $n(F_1)$ grows according

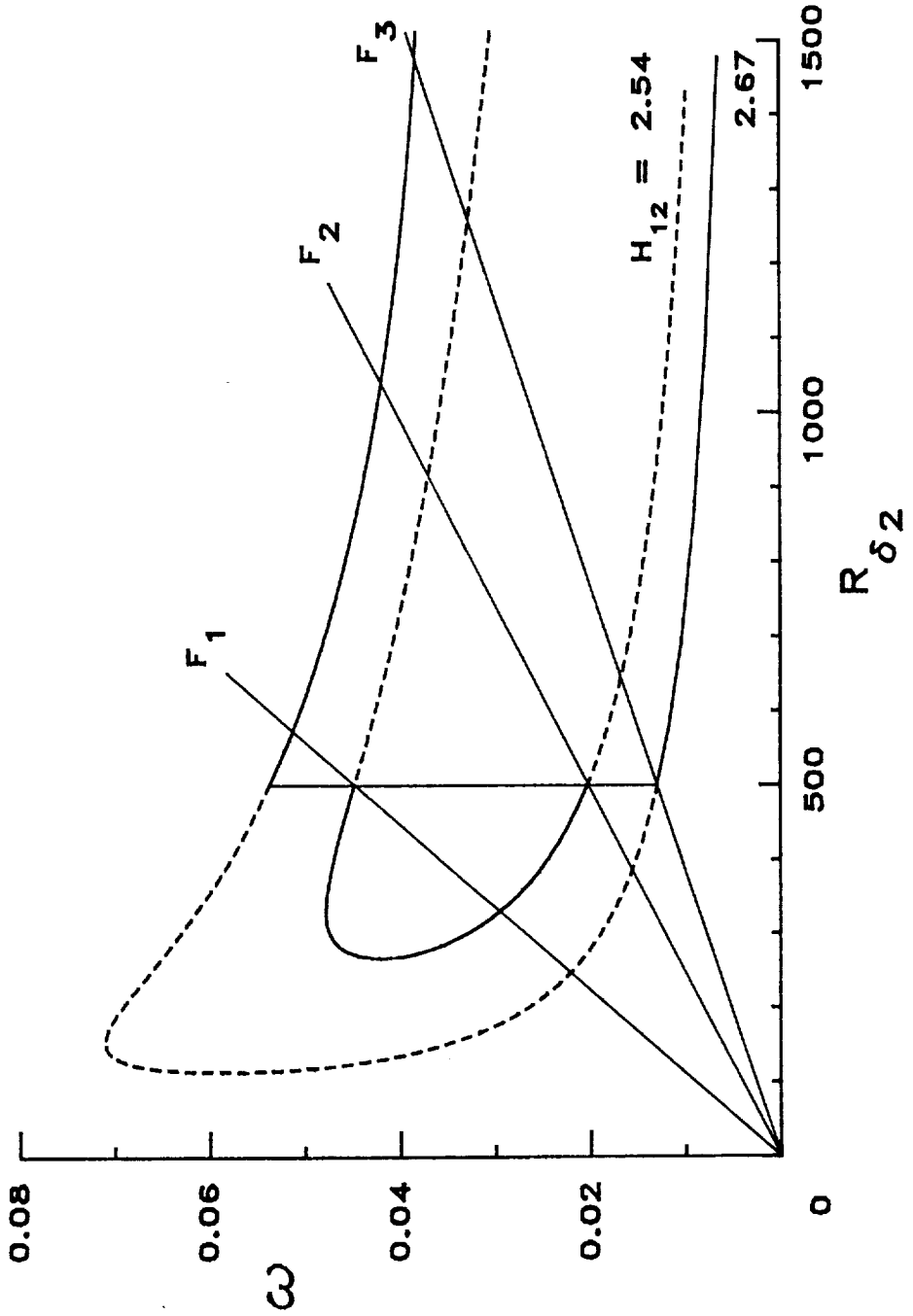

Fig. 4-5 Neutral curves for two values of the shape factor.

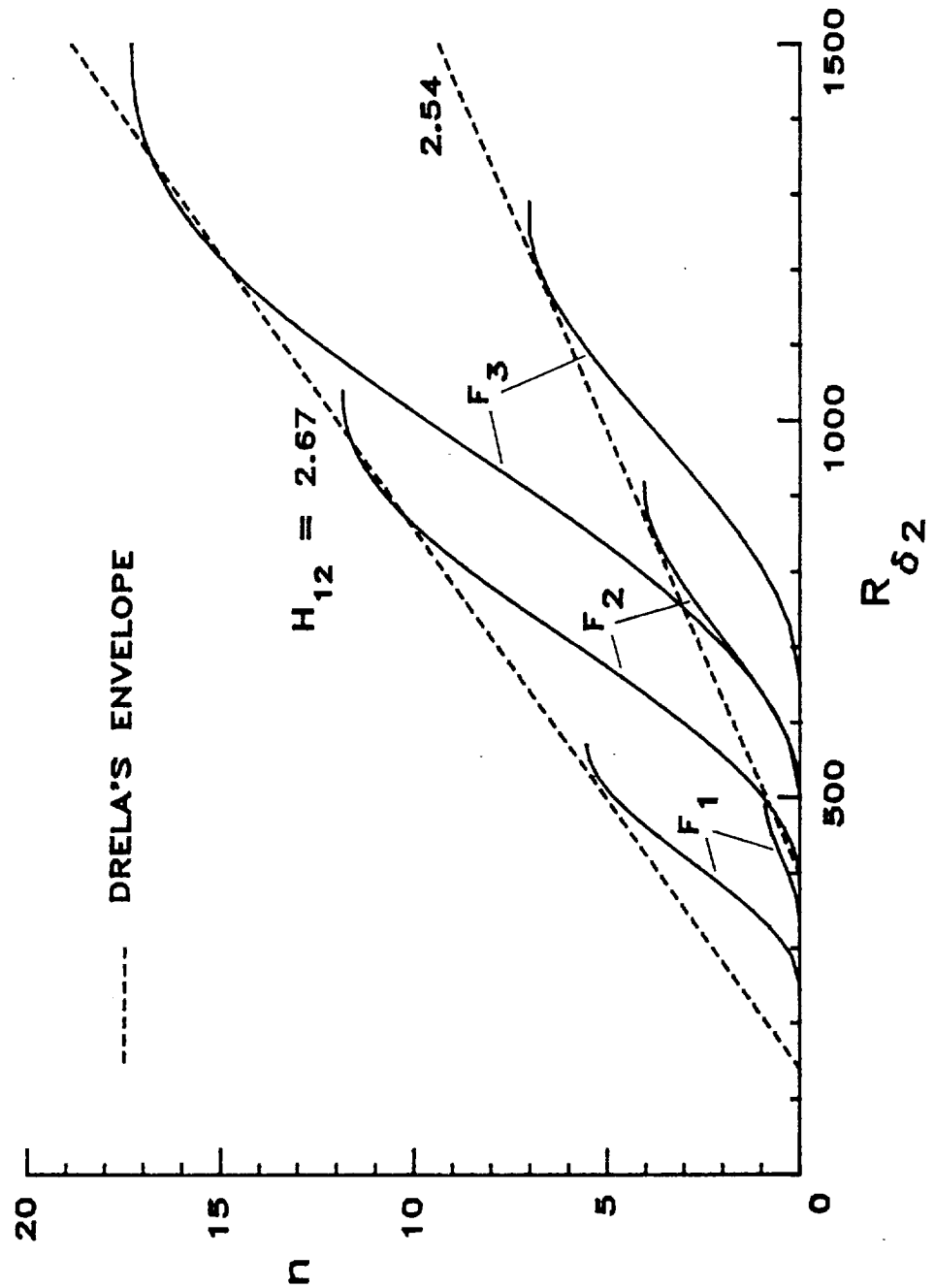

Fig. 4-6 Amplification curves for two values of the shape factor.

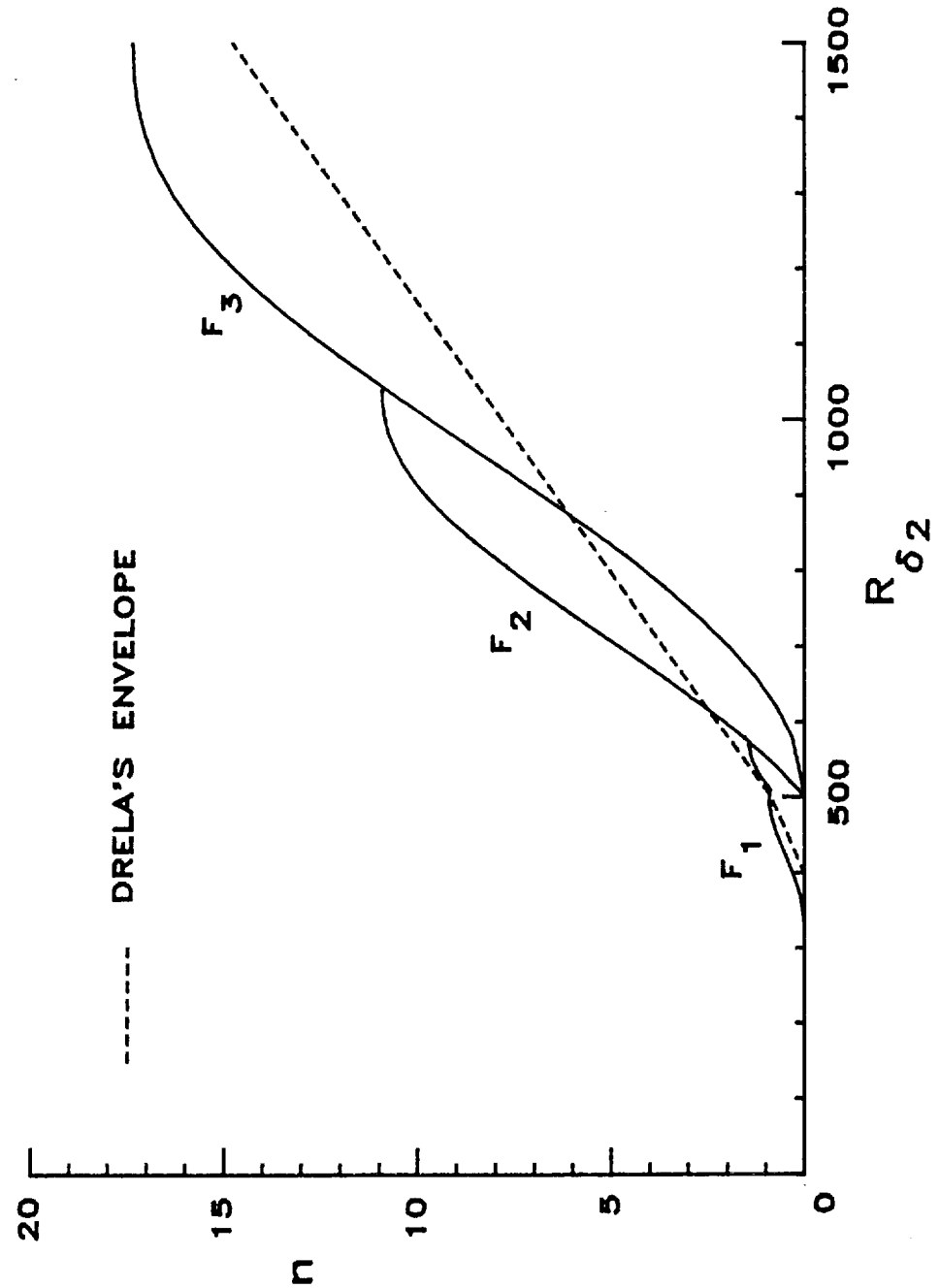

Fig. 4-7 Growth of n in a non-similar boundary-layer development compared to Drela's erroneous envelope method.

to Fig. 4-6 up to the maximum and, just as it is ready to start decaying, the jump in H_{12} forces further amplification until the upper branch of the neutral curve corresponding to $H_{12} = 2.67$ is crossed. This additional growth will not necessarily be steeper than the envelope. $n(F_2)$ does not start being amplified until the switch occurs, at which point it grows quite steeply in accordance with the greater area under the amplification rate surface $-\alpha_i(2.67, R_{\delta_2}, \omega)$. This curve does not necessarily exceed the envelope. Starting with the F_3-curve, at all lower frequencies the growth of n will follow the $H_{12} = 2.67$ line, which is parallel to but greater than Drela's envelope. In this example, it is possible to recover the steep similarity growth given by Eq. (4.23) since the shape factor is held constant downstream of the switch. In a non-similar development, however, the variation of H_{12} is continuous. If a monotonically increasing shape factor is approximated by a series of infinitesimally small steps, the resulting growth on n will never be able to "catch up" with the value obtained from a self-similar profile at the same local shape factor and Reynolds number. The correct envelope obtained by following each frequency, therefore, will lie above Drela's approximation without ever reaching the growth given by Eq. (4.23). The converse is true for an accelerating boundary-layer.

Based on the above argument, Drela's envelope method may be expected to overpredict the transition location for non-similar, decelerating flows and to underpredict it for non-similar, accelerating flows. This method has been incorporated in the model nonetheless, although the method of Stock and Degenhart should be extended to separated profiles and used in its stead in future research.

Chapter 5

THE TURBULENT PART OF THE BUBBLE

The calculation of the turbulent part of the bubble relies on the assumption that reattachment will occur. An independent bursting criterion has not been devised, nor have existing ones been tested. The reason is that bursting occurs either at very low Reynolds numbers or when the mean inviscid pressure gradient becomes too steep, downstream of a suction peak. Regardless of the fact that the same mechanism may not be responsible for both types of bursting, both conditions represent extremes that lie outside the capabilities of the simple approach taken with the present model. This is not so much because of a failure of the bubble model itself but, rather, because at such extremes the onset of strong global viscous/inviscid interaction modifies too greatly the inviscid pressure distribution which drives the model.

In this chapter, a parameter that characterizes the turbulent part of the bubble is introduced and the modelling of the reattachment process within the context of an integral method is discussed in detail.

Scaling Parameter

Having obtained a good approximation of the strong local viscous/inviscid interaction induced by the laminar part of the bubble and a fairly accurate transition location, now a steep pressure recovery must be predicted in order for the turbulent shear layer to reach again the inviscid distribution as it flows past reattachment, downstream of the strong interaction region. In the laminar part, the strength of the interaction depends on the amount of near-stagnant fluid downstream of separation and can be gauged by the deviation of the local viscous pressure distribution from

the inviscid. As this amount is, in turn, proportional to the local mean inviscid pressure gradient and to the momentum already lost by the boundary layer—to $(\delta_2)_S$, that is—it is not too surprising that the pressure recovered in this part of the bubble correlates well with P. In the turbulent part, on the other hand, the strong interaction is the result of a different mechanism, which acts to reverse what happened in the laminar part. As a consequence, the solution may be expected to depend on a different scaling parameter.

Assuming the boundary-layer equations to be valid in this region allows the use of conditions at transition as initial conditions for the turbulent calculations. A similar approach to that taken in the laminar part was attempted, at first. Thus, several types of velocity distributions, similar to Horton's straight line or to Stratford's recovery, were prescribed and the boundary-layer equations were solved in the direct mode. In addition to the difficulty in approximating observed reattachment velocity distributions with any degree of generality, the solution was found highly sensitive to the smallest variations in the input pressure distribution, suggesting that this part of the bubble could not be calculated by solving the boundary-layer equations in the direct mode.

Unlike in the laminar part, it is more convenient here to approximate the distribution of H_{32} than that of edge velocity. In fact, given that the value as well as the slope of the H_{32}-distribution is always known at the reattachment point, a general function has been developed in this study which allows the solution of the turbulent part of the bubble in the inverse mode. The distribution of H_{32} is specified as

$$H_{32}(\overline{y}) = (H_{32})_R + A_i\,[(H_{32})_T - (H_{32})_R]\left\{1 + \sin\left[\frac{\pi}{\overline{y}}\right]\right\} \qquad (5.1)$$

where the subscript $i = 1, 2$ denotes the amplitudes of the $\sin(1/x)$ function up-

stream and downstream of reattachment, respectively, and

$$\overline{y} = \left(\frac{2}{3} - \overline{y}_0\right)\sigma + \overline{y}_0 \tag{5.2}$$

$$\overline{y}_0 = \frac{\pi}{3\pi - \sin^{-1}(1/A_1 - 1)} \tag{5.3}$$

$$\sigma = \begin{cases} (s - s_T)/\ell_2 & s \leq s_R \\ [(s - s_T)/\ell_2 - 1]SF + 1 & s > s_R \end{cases} \tag{5.4}$$

where

$$SF = \sqrt{A_1/A_2} \tag{5.5}$$

ensures continuity in the curvature of $H_{32}(s)$ at the reattachment point. This function is shown in normalized form in Fig. 5-1.

The inverse boundary-layer formulation employed here, where the distribution of shape factor is specified [Eppler, 1989], is especially convenient and powerful since it allows complete control of the boundary-layer behavior in an otherwise extremely sensitive region while at the same time relying on an intrinsically general function. Indeed, in view of the discussion given above concerning the reversal of solution hierarchy in regions of reversed flow from the standard weakly-interacting boundary-layer formulation, it is perhaps not mere coincidence that an inverse method should prove so much more effective in this part of the bubble. Such effectiveness, however, comes at a price. In fact, while specification of the pressure recovery distribution, if the correct one were indeed known in general, would automatically drive the boundary layer to reattach at the correct location, the turbulent length of the bubble, ℓ_2, in Eq. (5.4) is not known *a priori* and must be found by independent means.

For some time during the model development, the inviscid velocity distribution was used to guide the location of the reattachment point. The correct value of ℓ_2, that is, would be the one that leads the pressure at reattachment near the inviscid

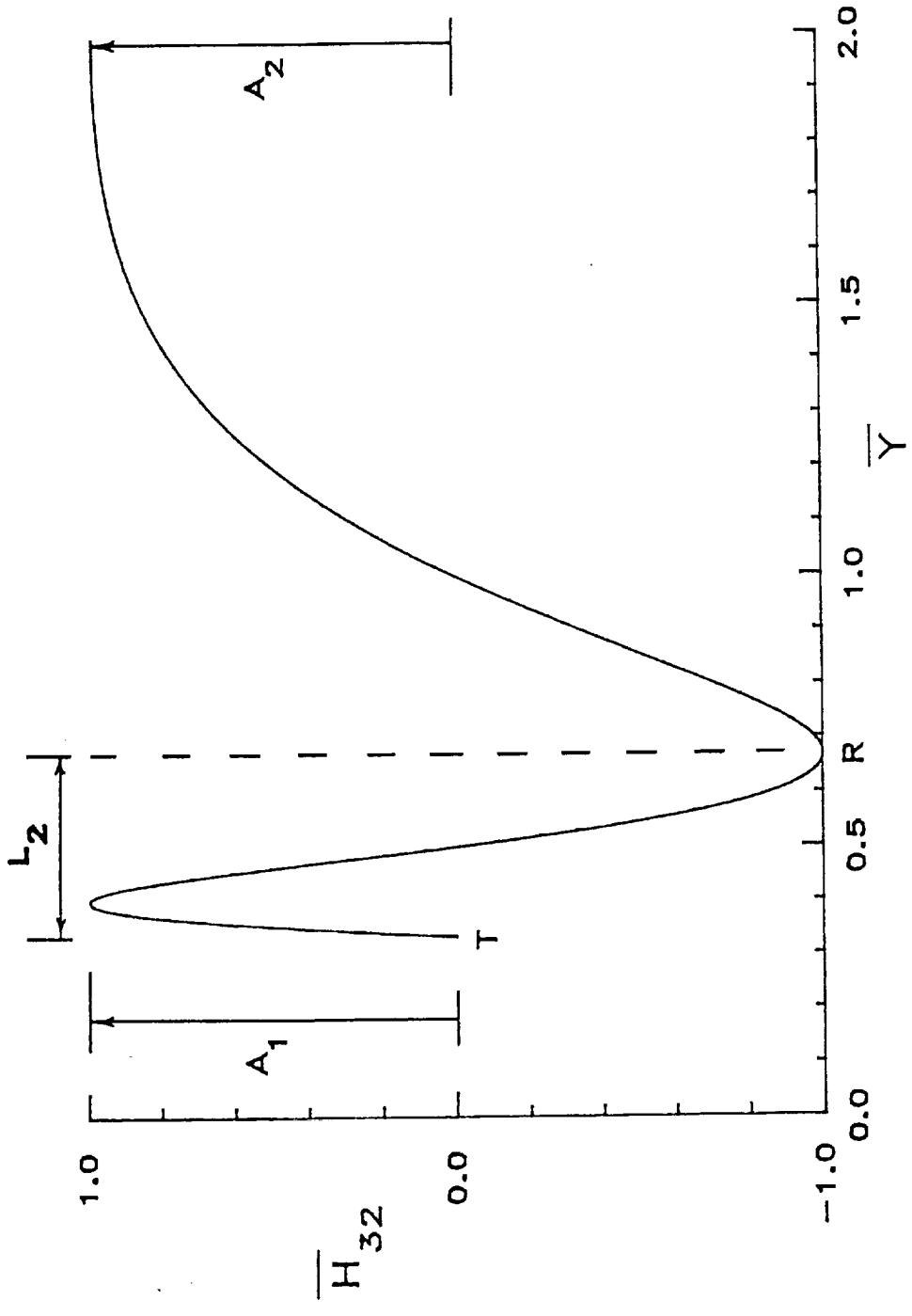

Fig. 5-1 Normalized shape factor turbulent recovery function.

value at the same station. Previous models, such as Horton's, have also assumed that reattachment occurs at the intersection of the bubble recovery with the inviscid pressure distribution. Using the experimental pressure distributions for the NLF(1)-1015 airfoil, however, integration of the boundary-layer equations in the direct mode along the bubble revealed that the reattachment point may lie significantly above as well as below this intersection. Although the validity of this result is limited by the accuracy of the closure correlations employed, as well as by the assumption of the validity of the boundary-layer equations themselves, the observed trends seemed too consistent to be mere coincidence. Specifically, it was observed that for long, high-drag, mid-chord bubbles, corresponding to the middle of the airfoil drag polar, the reattachment point is always below the inviscid distribution (above, in the value of pressure) whereas for short mid-chord bubbles about to disappear corresponding to the top of the low-drag bucket in the airfoil polar, as well as for leading-edge bubbles, the reattachment point is always well above the inviscid. Allowing this point to move and trying to reproduce the observed trends by means of an empirical function based on local bubble conditions was helpful in obtaining reasonable drag predictions at least for a single Reynolds number. The inability to justify such a function physically and its limited generality, however, prompted further study.

It was noticed that interaction methods have no trouble pinpointing the unique solution. Whereas the accuracy of such computed solutions still depends on the accuracy of the correlations, their mere ability to reach a converged solution indicates that all the necessary physical constraints are somehow accounted for. Also, their success at predicting the correct trends with respect to the location and pressure level of the reattachment point is explained by their ability to "sense" the presence of the wall through variations in the strength of the transpiration velocity or through the shape of the displacement thickness itself needed for convergence. An equiv-

alent geometrical constraint had to be introduced in the present model. Whereas prescribing the pressure level at reattachment is consistent with a direct formulation of the boundary-layer equations, in a region of such strong viscous/inviscid interaction as the bubble the inverse formulation of the boundary-layer equations should be complemented with the treatment of the correct physical process as the indcpendent one to reflect the reversal in the solution hierarchy. The local flowfield is driven by a turbulent momentum-transfer mechanism whereby the outer momentum brought toward the wall accelerates the near-stagnant reverse flow until reattachment is achieved. Reattachment, therefore, becomes dependent on the efficiency of this mechanism. In geometrical terms, the reattachment location becomes dependent on the spreading angle of the turbulent shear layer and on the initial distance of the shear layer from the wall; that is, on the height of the bubble at transition. Since the spreading rate of the shear layer is nearly insensitive to variations in Reynolds number and, in this particular flowfield, in inviscid pressure gradient, the turbulent length of the bubble becomes almost entirely dependent on the thickness of the bubble at transition nondimensionalized with respect to the airfoil chord. Making the characteristics of the turbulent part of the bubble depend on this parameter has enabled the model to reproduce all the available experimental data with excellent and consistent accuracy in the range $100,000 < R < 2,000,000$.

Governing Equations

Following Eppler [1989], the distribution of H_{32} described above is input into the momentum and energy integral equations expressed in the inverse mode,

$$\frac{dU}{ds} = \left[(c_f/2)H_{32} - C_D + \delta_2 \frac{dH_{32}}{ds}\right] \frac{U}{\delta_2 H_{32}(H_{12}-1)} \tag{5.6}$$

$$\frac{d\delta_2}{ds} = \left[-\frac{3(c_f/2)H_{32}}{H_{12}+2} + C_D - \delta_2 \frac{dH_{32}}{ds}\right] \frac{H_{12}+2}{H_{32}(H_{12}-1)} \tag{5.7}$$

where H'_{32} denotes the derivative with respect to s of Eq. (5.1).

Drela's turbulent boundary-layer method makes use of an additional equation, the turbulence lag equation. Following Green et al. [1973], Drela simplifies the stress-transport equation originally proposed by Bradshaw and Ferris [1968] to a rate equation for the maximum shear stress coefficient,

$$\frac{\delta}{C_\tau}\frac{dC_\tau}{ds} = 4.2(C_{\tau_{eq}}^{\frac{1}{2}} - C_\tau^{\frac{1}{2}}) \tag{5.8}$$

where C_τ is defined as

$$C_\tau = \frac{(-\overline{u'v'})_{max}}{U^2} \tag{5.9}$$

and δ, the boundary-layer thickness, is given by

$$\delta = \delta_2\left(3.15 + \frac{1.72}{H_{12}-1}\right) + \delta_1 \tag{5.10}$$

This system of equations needs to be supplemented with closure relations for C_D, H_{12}, c_f, and $C_{\tau_{eq}}$.

Closure

Much of the following discussion is an expansion on that given by Drela [1986]. The maximum shear stress coefficient is used in the expression for the local dissipation coefficient. Its deviation from the equilibrium value, $C_{\tau_{eq}}$, as calculated by means of Eq. (5.8) accounts for the slow response of the intensity of the turbulence being convected from upstream to varying local conditions. The equilibrium value refers to the equilibrium turbulent boundary layers of Clauser [1954], for which the local pressure gradient acting on the displacement thickness is balanced by the local wall shear stress. The ratio of the two forces acting on an incremental "slice" of the boundary layer is a constant,

$$\frac{\delta_1}{\tau_w}\frac{dp}{ds} = -\frac{2}{c_f}\frac{\delta_1}{U}\frac{dU}{ds} = \beta_t \tag{5.11}$$

For equilibrium flows, the modified shape parameter G_t is also constant,

$$G_t = \frac{H_{12}-1}{H_{12}}\frac{1}{\sqrt{c_f/2}} = \frac{1}{\sqrt{c_f/2}} - \frac{\delta_2}{\Delta} \tag{5.12}$$

Δ is the displacement thickness scaled in an analogous way to the defect profile,

$$\Delta = \int_0^\infty \frac{U-u}{u_*}dy = \delta_1\frac{u_*}{U} \tag{5.13}$$

where

$$u_* = \sqrt{\frac{\tau_w}{\rho}} = U\sqrt{\frac{c_f}{2}} \tag{5.14}$$

To lowest order, the defect law $(u-U)/u_*$ *vs.* y/δ will collapse the outer layer of any boundary-layer development for which β_t equals a constant. Thus, there exists a unique relationship between G_t and β_t for equilibrium boundary layers, or "equilibrium locus" [Kline et al., 1968],

$$G_t = 6.7\sqrt{1+0.75\beta_t} \tag{5.15}$$

Using Eqs. (5.11), (5.12), and (5.15), the velocity gradient can be expressed as

$$\frac{\delta_1}{U}\frac{dU}{ds} = \frac{1}{0.75}\left[\frac{c_f}{2} - \left(\frac{H_{12}-1}{6.7H_{12}}\right)^2\right] \tag{5.16}$$

Noting that for these flows H_{12} and H_{32} are nearly constant, Eq. (2.5) can be simplified to

$$0 = C_D - \frac{c_f}{2}H_{32} + H_{32}(H_{12}-1)\frac{\delta_2}{U}\frac{dU}{ds} \tag{5.17}$$

Eliminating the velocity gradient between Eqs. (5.16) and (5.17), yields an expression for the dissipation coefficient valid only for equilibrium flows,

$$C_D = \frac{c_f}{2}\left[\frac{4}{H_{12}} - 1\right]\frac{H_{32}}{3} + 0.03\left[\frac{H_{12}-1}{H_{12}}\right]^3 \tag{5.18}$$

In the laminar boundary-layer calculation, the closure relationships are derived from the similarity profiles and, strictly, are valid only for such flows. This means

that if for a self-similar development the Falkner-Skan pressure gradient parameter is calculated directly from its definition [Schlichting, 1979],

$$\beta = \frac{\xi_{FS}^2}{\nu}\frac{dU}{ds} \tag{5.19}$$

this value will be constant and will correspond to a unique value of the shape factor, also constant. In a non-similar development, on the other hand, the relationship between β and H_{32} is not unique anymore. It is found in this case that calculating the shape factor from the governing equations while disregarding entirely the local value of β allows accurate values for C_D, H_{12}, and c_f to be obtained even though the similarity correlations are utilized. In the calculation of the turbulent boundary layer the same approach is used by Eppler [1963] who utilizes empirical correlations that are valid mostly for equilibrium flows. In this case, however, obtaining the shape factor from the governing equations is not sufficient anymore if the pressure gradient is varying too rapidly as, for instance, downstream of a bubble. This is because of the large inertia of the Reynolds stresses that respond slowly to variations in local pressure gradient. As the stress level is the most important physical quantity in a turbulent boundary layer, it makes sense for there to be a need for its careful modelling in flows that depart too greatly from equilibrium assumptions. Just as in the laminar case decoupling the shape factor from local conditions brought a great gain in accuracy, so here the maximum shear stress coefficient should be decoupled from a statement of the type of Eq. (5.21) (in the next page) and obtained independently. Therefore, just as in the laminar case an additional equation is necessary, the kinetic energy integral equation, a third governing equation must be introduced, the rate equation for C_τ.

The integral variable which is affected the most by the stress level in the boundary layer is the dissipation coefficient. In the laminar case, obtaining the shape factor independently was sufficient to obtain accurate values of C_D through the

similarity correlation, Eq. (3.16) inside the bubble. Although this provides no guarantee of success for the turbulent case, an analogous argument is followed and Eq. (5.18) is assumed to be valid also for non-equilibrium flows. In order to be able to use it, however, it must be expressed in terms of $C_{\tau_{eq}}$. To this end, the dissipation coefficient is assumed to equal the sum of a wall and a wake contribution,

$$C_D = c_f U_{slip} + 2C_{\tau_{eq}}(1 - U_{slip}) \tag{5.20}$$

By equating this expression to Eq. (5.18),

$$C_{\tau_{eq}} = \frac{0.015 H_{32}}{1 - U_{slip}} \left[\frac{H_{12} - 1}{H_{12}}\right]^3 \tag{5.21}$$

$$U_{slip} = \frac{H_{32}}{6}\left[\frac{4}{H_{12}} - 1\right] \tag{5.22}$$

So that, finally, the dissipation coefficient is given by

$$C_D = c_f U_{slip} + 2C_{\tau}(1 - U_{slip}) \tag{5.23}$$

where U_{slip} is given by Eq. (5.22) and C_τ is calculated from the rate equation (5.8).

The shape factor correlation is derived from the analytical profiles of Swafford [1983]. In the present method, this correlation needs to be expressed in the form $H_{12}(H_{32})$. Since Drela's correlation is expressed as $H_{32}(H_{12})$ and, unlike in the laminar case, cannot be inverted, a close approximation has been developed. Defining first

$$H_{32_0} = 1.505 + \frac{4}{R_{\delta_2}} \tag{5.24}$$

$$H_{12_0} = 3 + \frac{400}{R_{\delta_2}} \tag{5.25}$$

$$c_1 = 0.081(R_{\delta_2} - 300)^{0.1} \tag{5.26}$$

$$c_2 = 0.0158(R_{\delta_2} - 300)^{0.08} \tag{5.27}$$

$$c_3 = 1.06 + \frac{3000}{(R_{\delta_2} + 600)^{1.5}} \tag{5.28}$$

H_{12} is obtained from

$$H_{12} = \begin{cases} \dfrac{H_{12_0}}{1+\left[\frac{H_{32}-H_{32_0}}{c_1}\right]^{\frac{1}{1.27}}}, & c_f > 0 \\ H_{12_0} + \left[\dfrac{H_{32}-H_{32_0}}{c_2}\right]^{\frac{1}{c_3}}, & c_f < 0 \end{cases} \tag{5.29}$$

This expression, as the original, is valid for $R_{\delta_2} > 400$. It is shown in Fig. 5-2.

The skin-friction law of Swafford is employed for attached flow,

$$c_f = \frac{0.3e^{-1.33H_{12}}}{(\log R_{\delta_2})^{1.74+0.31H_{12}}} + 0.00011\left[\tanh\left(4 - \frac{H_{12}}{0.875}\right) - 1\right] \tag{5.30}$$

This expression does not give the correct value of skin-friction in the turbulent part of the bubble. The modification employed is discussed in the next section together with the remaining empirical functions.

Supplementary Functions

In order to achieve good agreement with measured bubble pressure distributions and corresponding airfoil drag coefficients, existing turbulent correlations had to be modified and several empirical functions have been introduced. These functions are specified by assigning values to certain parameters left free. While such a formulation granted the model great flexibility, the unknown dependence of these parameters on local flow conditions significantly limited its generality. Identification of the correct scaling parameter for the turbulent part of the bubble, however, has made the determination of the correct functional dependence of these parameters both easier and less crucial. The remaining details for the calculation of the turbulent part of the bubble will now be discussed and, wherever possible, supporting arguments will be given. It should be realized, however, that final proof of the validity of the modifications introduced will await more detailed measurements of this region of the bubble flowfield.

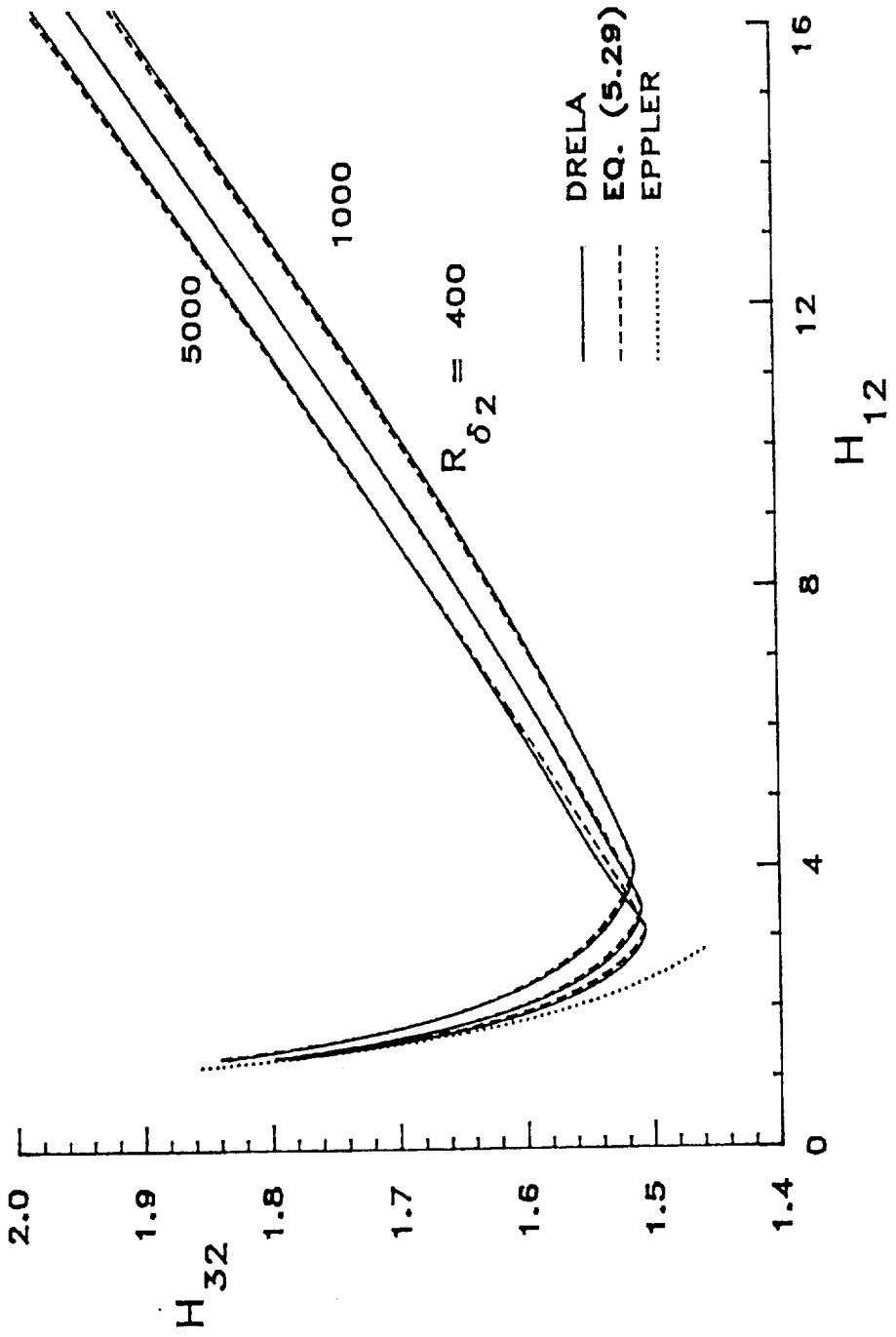

Fig. 5-2 Comparison of the shape factor correlation of Eppler, Drela, and the present function.

The height of the bubble at transition is estimated by means of the expression

$$h_T = \frac{\ell_1}{\tan\gamma} \tag{5.31}$$

where $\tan\gamma$ is given by Eq. (3.18). An estimate for the spreading angle is obtained from the experimental values reported by Birch and Eggers [1973]. In this report, measured spreading rates are expressed in nondimensional form as function of a velocity ratio defined as

$$\lambda = \frac{u_1 - u_2}{u_1 + u_2} \tag{5.32}$$

where u_1 and u_2 are the velocities above and below a splitter plate, respectively. The spreading rates are normalized with respect to the maximum, which occurs at $\lambda = 1$. The data are all taken in shear layers developing in zero pressure gradient, so that their validity in the turbulent part of the bubble, where the pressure varies very rapidly, could be doubted.

Making recourse to the strongly interacting nature of the flow, the above objection can be dispelled. Specifically, this shear layer is not developing inside a duct with diverging wall, where the pressure gradient is imposed as a boundary condition of the inviscid flow. In the bubble, the amount of pressure recovered is strictly a function of the intensity of the turbulence: of the momentum transfer across the shear layer. Therefore, treating the reattaching turbulent shear layer in the bubble as a shear layer in zero pressure gradient with varying velocity ratios, with the rise in pressure a by-product with negligible feed-back, seems a reasonable approximation.

In order to obtain an estimate of the spreading rate of the shear layer from the experimental plot given by Birch and Eggers, it should be realized that between transition and reattachment λ varies between a value slightly greater than 1 to 1. It falls, therefore, off the plot. Since the magnitude of the reverse flow is quite small

compared to the local edge velocity, it is not a bad approximation to assume that the spreading rate will be slightly larger than the maximum reported and constant. The following function, which depends weakly on Reynolds number, has been found satisfactory,

$$\tan\theta = .0975 + 2.5 \times 10^{-8} R \tag{5.33}$$

This corresponds to a spreading angle varying from 5.71^0 at $R = 100,000$ to 8.39^0 at $R = 2,000,000$, measured from the parallel to the airfoil surface. Thus, the turbulent length of the bubble is simply obtained from

$$\ell_2 = \frac{h_T}{\tan\theta} \tag{5.34}$$

The bubble geometry as defined by these expressions is summarized in Fig. 5-3.

The coarseness of this approximation may seem unnecessary. In fact, it is a well known fact that the dividing streamline is curved downstream of transition and meets the airfoil surface at 90°. It is assumed here, instead, to be straight. In addition, the spreading of the shear layer should be measured from its bottom edge or from its center, the line of zero velocity, whereas here it is measured from the dividing streamline. This apparently wrong resolution of the bubble geometry is followed because the height of the dividing streamline is the only length scale known entirely from the upstream development. The approximation works so well because the extent of the turbulent part of the bubble is very short and because this height is an accurate characteristic length.

Having determined ℓ_2, Eq. (5.1) is completely specified when values are assigned to the A_i. The value for A_1 may be linked to the length of the transition region. In accordance with the H_{32}-distributions measured by Horton [1967] as well as, more recently, by Fitzgerald and Mueller [1990], A_1 is such that H_{32} grows steeply downstream of transition to a local maximum before dropping to the

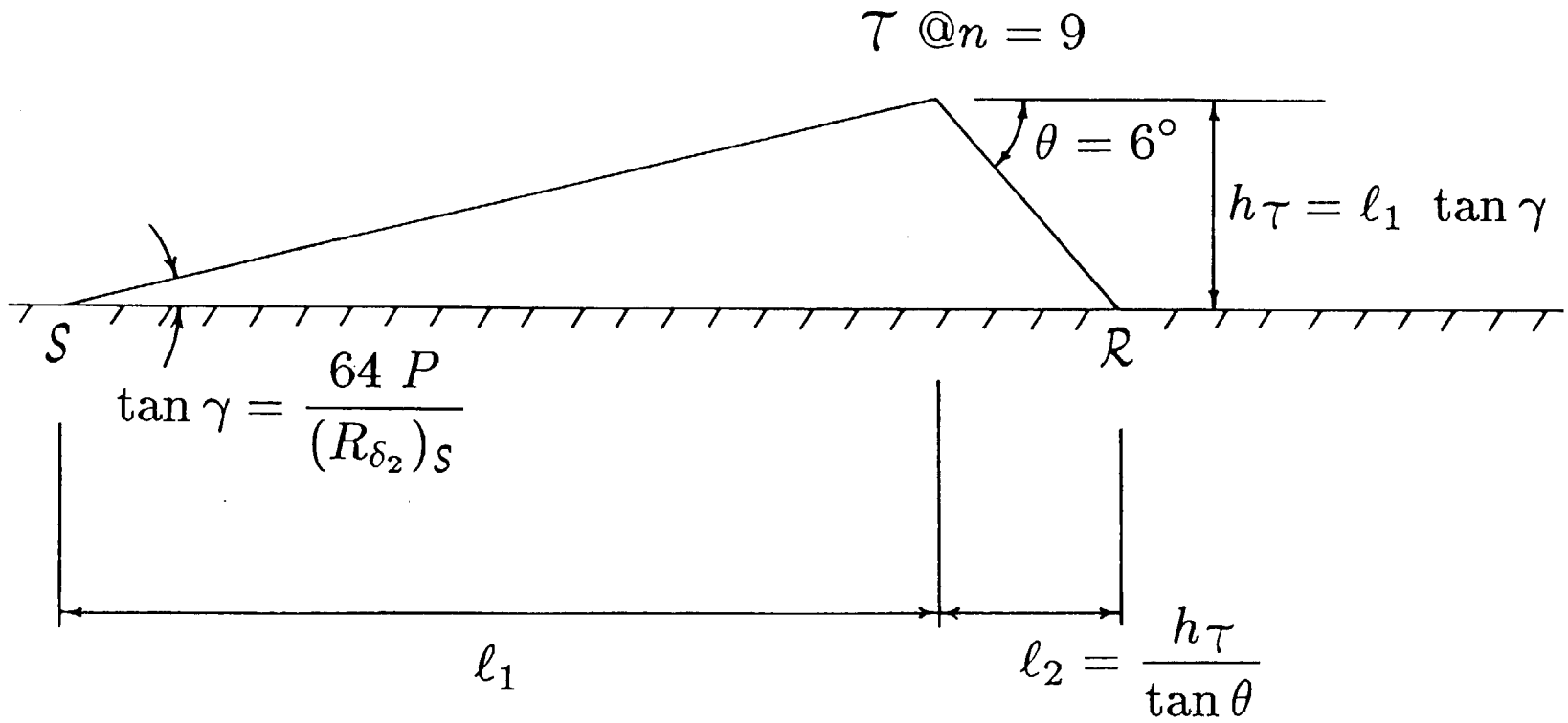

Fig. 5-3 Summary of bubble geometry and scaling parameters.

reattachment value. This local maximum corresponds to the sharp "knee" in the pressure distribution which, as maintained by Russell [1978], occurs downstream of transition and corresponds to the location where the turbulent shear layer first touches the surface. The following function has been found necessary to give good results for leading-edge as well as mid-chord bubbles,

$$A_1 = 0.5 + e^{-300(h_T/c)} \tag{5.35}$$

The value of A_2 is obtained by iterating on the intersection angle between the undershoot and the inviscid distribution. As shown in Fig. 5-4, the calculations between the reattachment point and this intersection are repeated with different values of A_2 until the angle satisfies the desired tolerance. As the drag prediction has been found to be quite insensitive to this tolerance, it has been relaxed to only 1 radian to maximize computational efficiency.

The closure relations for C_D and c_f, Eqs. (5.23) and (5.30), were originally used unchanged. There were cases, however, when the reattaching experimental pressure distribution could not be reproduced. This is explained as follows. Drela's turbulent correlations were originally developed for separated turbulent boundary layers downstream of turbulent separation. The skin-friction coefficient obtained from these correlations in the turbulent part of the bubble is quite small in magnitude, equal to or less than that in the laminar part, while the dissipation coefficient is very similar to that of an attached turbulent boundary layer. While such values make sense in the slowly recirculating, constant pressure flow downstream of turbulent separation, they are clearly too small to reflect the effect of a turbulent shear layer impinging on the wall, a process for which the boundary-layer approximations are likely to break down. This claim is also supported by Navier-Stokes simulations, such as the one reported by Briley and McDonald [1983], which show a peak in negative skin friction in the turbulent part of the bubble several times its

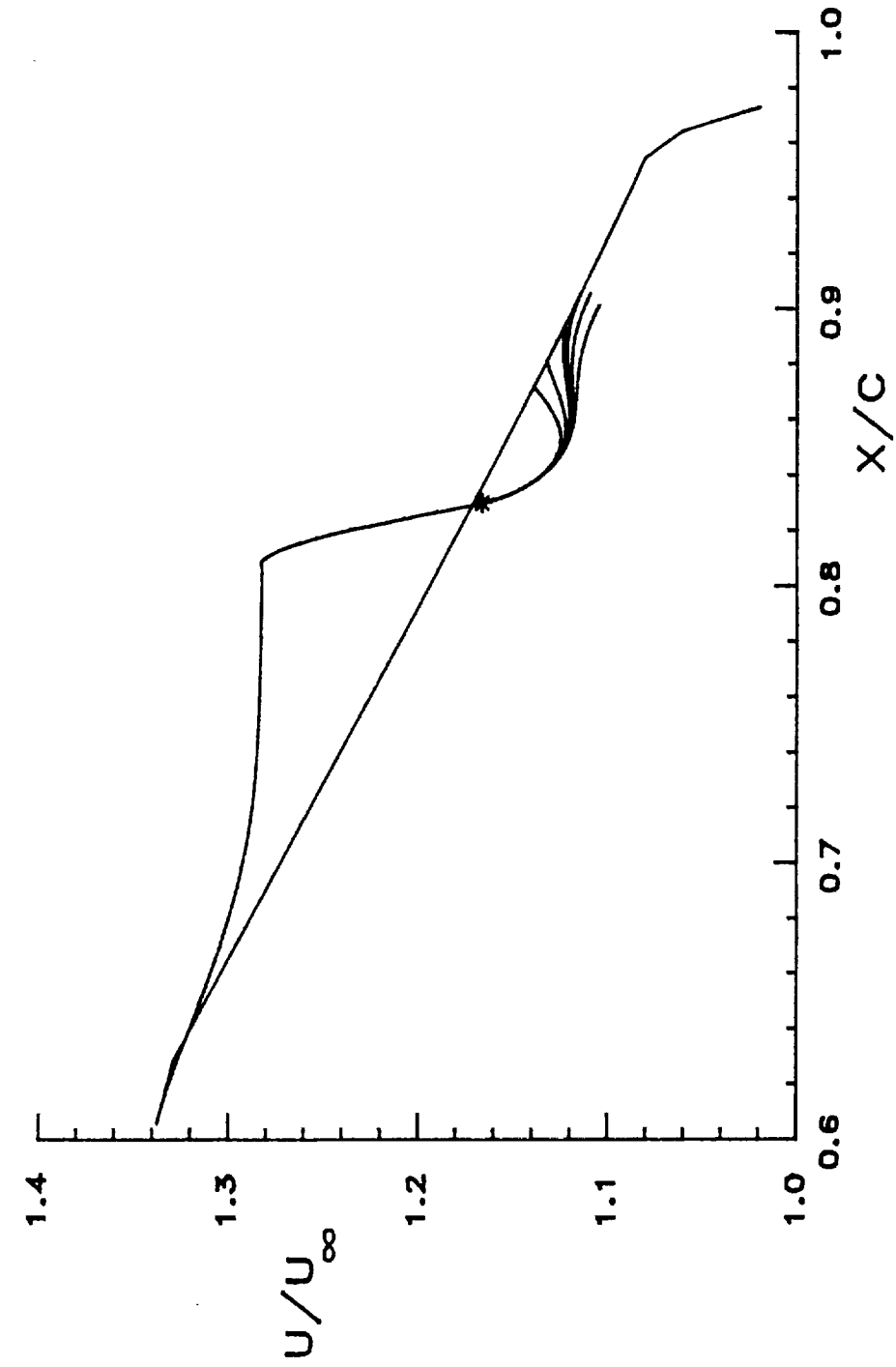

Fig. 5-4 Example of iteration on undershoot to merge with inviscid distribution.

value before transition, as well as by the high peak in heat-transfer coefficient measured at the reattachment point of bubbles developing on turbine blades [Pucher and Göhl, 1987]. Roberts [1980] reports a measured mean value for the dissipation coefficient of 0.035, which is twice the value originally proposed by Horton and also given by Drela's correlations. Finally, it is not known with certainty whether or not the reattachment process is unsteady. Unsteadiness certainly seems likely at lower Reynolds numbers, as the critical value is approached, or for very large values of h_T/c. The most effective way to capture such unsteadiness in a steady, integral method is to lump its effects into a higher value for C_D.

Two additional empirical functions have been introduced. The distribution of skin-friction is specified by fitting a parabola to the transition point, the reattachment point (where $c_f = 0$ by definition), and to a preassigned value, $c_{f_{min}}$, half-way in between,

$$c_{f_{min}} = -\sqrt{0.0002\frac{h_T}{c}} \tag{5.36}$$

The higher level of dissipation is obtained by means of a multiplicative function to Drela's values. This function rises quadratically from 1 at transition to a peak, $C_{D_{max}}$, at the mean reattachment point and then exponentially decays back to 1 a small distance downstream of reattachment,

$$f = \begin{cases} 1 + (C_{D_{max}} - 1)\left(\frac{s-s_T}{\ell_2}\right)^2, & 0 \le \frac{s-s_T}{\ell_2} \le 1 \\ 1 + (C_{D_{max}} - 1)e^{-r\left(\frac{s-s_T}{\ell_2}-1\right)}, & \frac{s-s_T}{\ell_2} > 1 \end{cases} \tag{5.37}$$

where the decay rate is

$$r = 15 - 1000\frac{h_T}{c} \tag{5.38}$$

such that

$$C_D = f \times [C_D]_{Drela} \tag{5.38}$$

The decay rate downstream of reattachment increases with decreasing bubble thickness at transition. This reflects the assumed slower rate of decay of the turbulence

(or unsteadiness) downstream of thicker bubbles.

It is not known whether or not Roberts's value of $C_D = 0.035$ is representative of most bubbles. Thus, although the value of $C_{D_{max}}$ could be adjusted to match this experimental value, its general dependence on varying flow conditions cannot be inferred from it. Given the great impact of this variable on the shear layer development, however, it is still indispensable to obtain an estimate for at least the order of magnitude of its variation. Rather than offering a rigorous derivation, the following argument discusses flow variables that may be used to develop an empirical correlation between $C_{D_{max}}$ and h_T/c.

As shown in Fig. 5-5, it is observed that, for an airfoil at a fixed α, as the Reynolds number decreases the bubble increases in length with the (nondimensional) edge velocity at transition remaining practically constant. The laminar separation point calculated with the boundary-layer equations (without interaction) is independent of Reynolds number [Schlichting, 1979]. Since most airfoil velocity distributions are nearly linear in the main recovery region, the amount of velocity that needs to be recovered in order to reach the inviscid distribution from a constant value at transition increases linearly as this value moves downstream. Referring now to Fig. 5-6, it can be seen how the main contribution to the decrease in edge velocity comes from the dissipation coefficient term in Eq. (5.6). Specifically, the decrease in velocity between transition and reattachment is mostly dependent on the area under the C_D-distribution. As an aside, it can be seen from this figure that a correct modelling of c_f is not crucial. If a linear decrease in velocity with increasing transition length is desired, therefore, an approximately linear increase in this area is necessary. As the Reynolds number decreases, the ratio

$$P/(R_{\delta_2})_S = \frac{(\delta_2)_S}{U_S}\frac{\Delta U}{\Delta s} \tag{5.39}$$

which determines the separation angle, varies together with the transition length

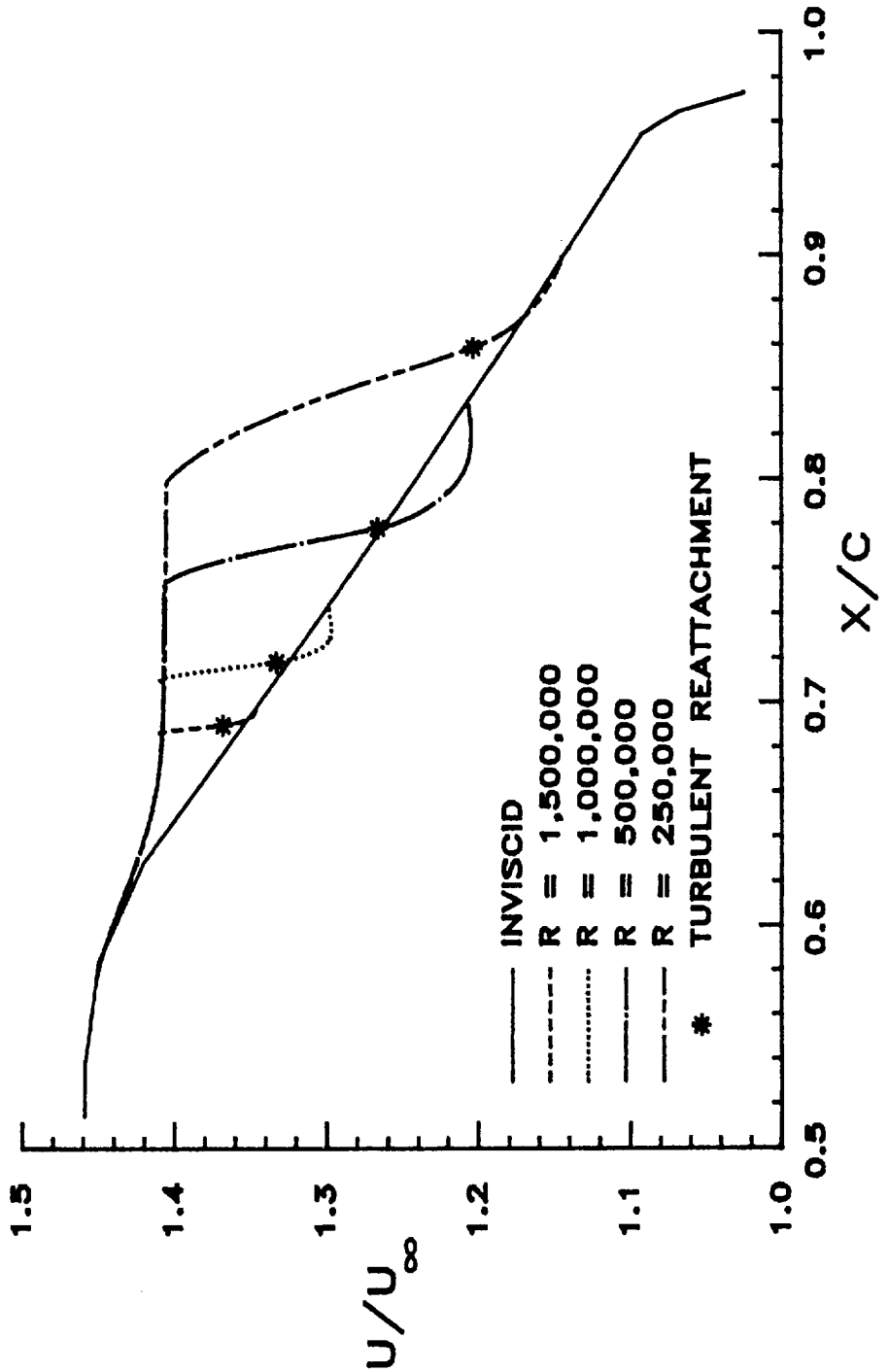

Fig. 5-5 Effect of decreasing Reynolds number on bubble velocity distribution.

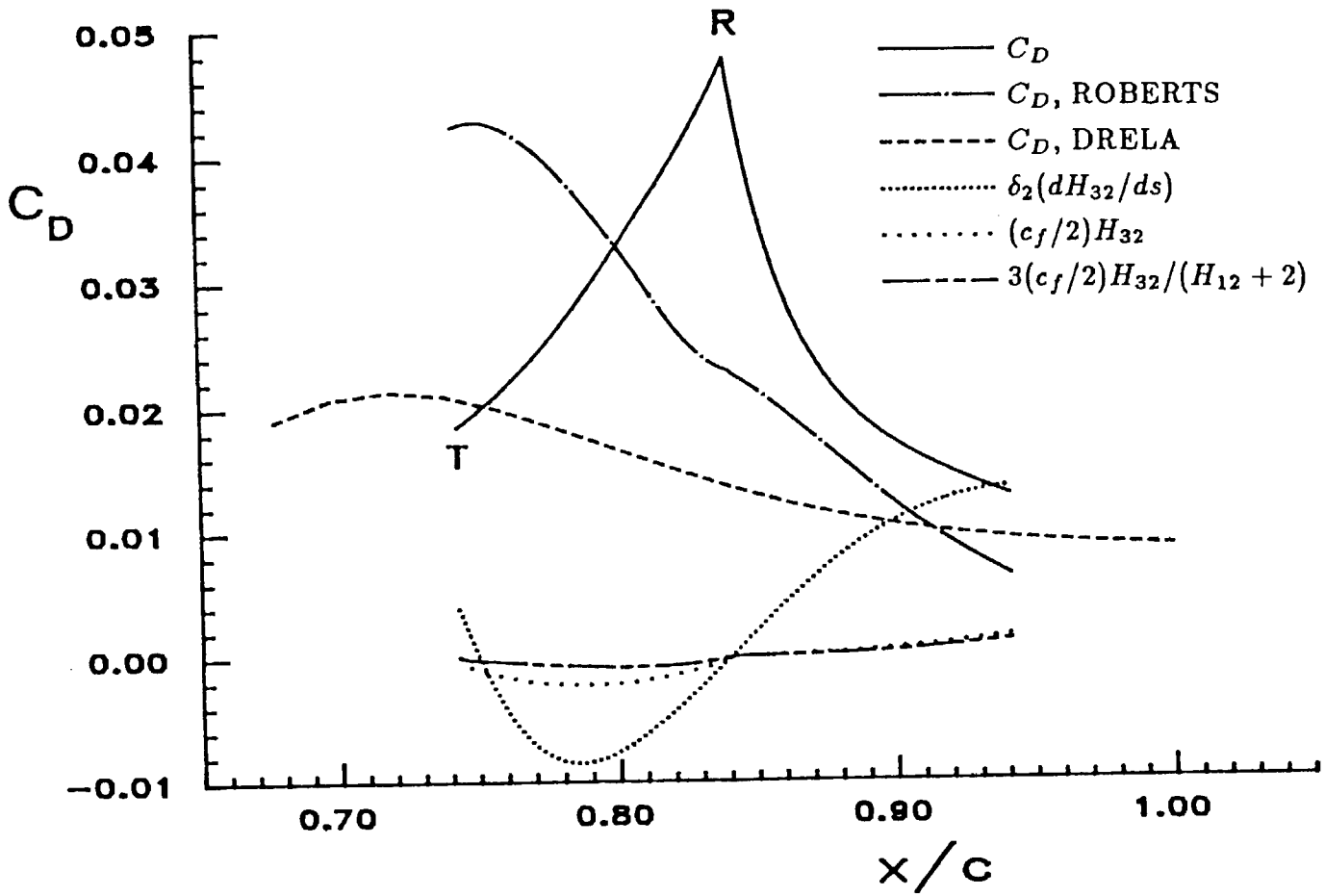

Fig. 5-6 Comparison of different terms in governing equations affecting the pressure recovery.

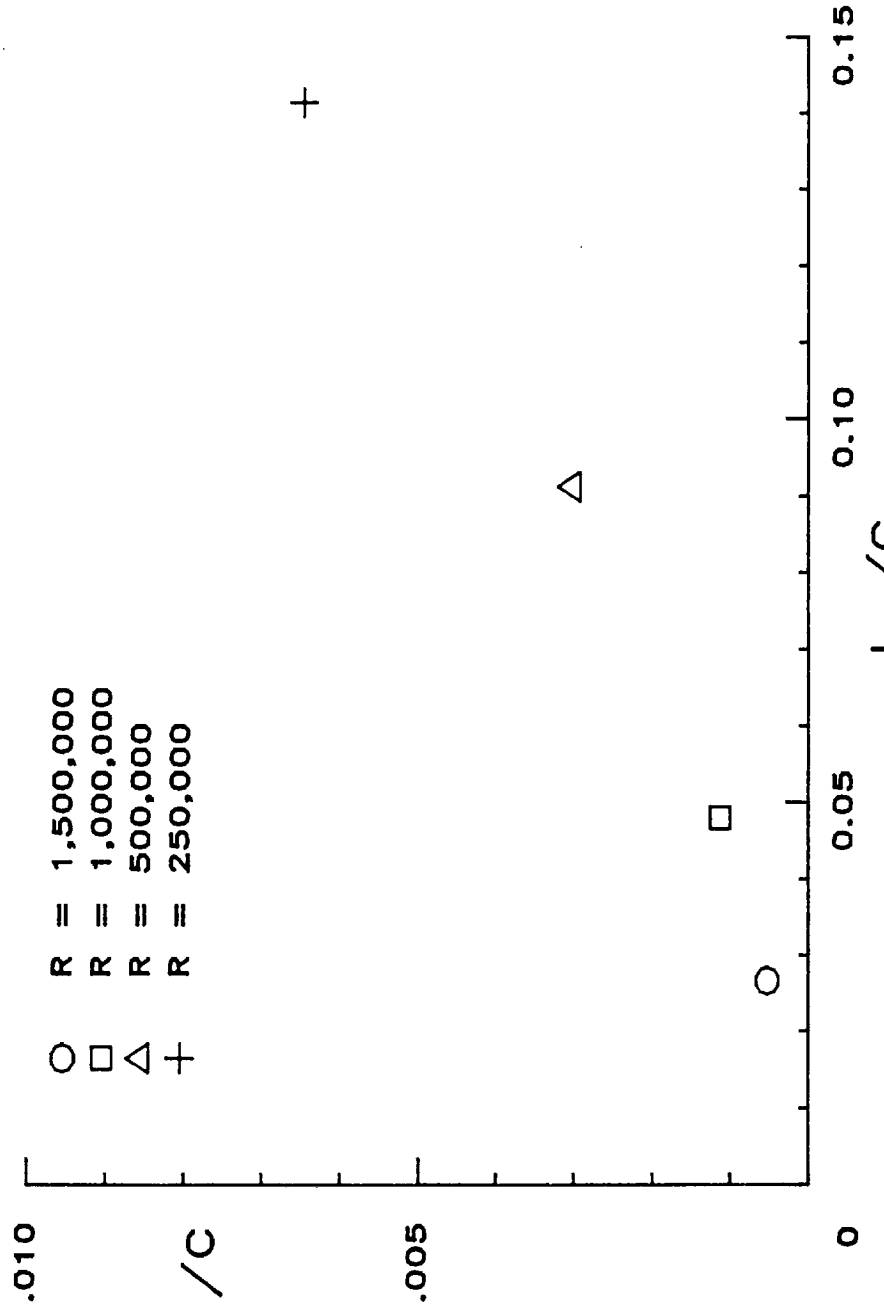

Fig. 5-7 Variation of bubble height at transition with laminar length.

in such a way that the height of the bubble at transition varies almost linearly with ℓ_1. This is shown in Fig. 5-7 for the bubble and the Reynolds numbers shown in Fig. 5-5. Finally, as the spreading angle of the turbulent shear layer is also nearly constant, the turbulent length of the bubble also increases linearly with transition length. Therefore, in order for the area under the C_D-distribution to increase linearly over this length, $C_{D_{max}}$ should remain constant.

Given the very approximate nature of the argument given above, it is not surprising that some variation in $C_{D_{max}}$ was found necessary. The function that has given the best agreement is

$$C_{D_{max}} = 1 + \sqrt{200\frac{h_T}{c}} \tag{5.40}$$

This modification has led to a much greater control on the amount of pressure recovery between transition and reattachment such that any experimental pressure distribution can now be reproduced simultaneously with the correct growth in δ_2. This function is shown in Fig. 5-8 together with the variations of A_1 and $c_{f_{min}}$.

Model Flowchart

Having described each part of the bubble separately, the scheme used by the present method of predicting the development of laminar separation bubbles is now summarized by the flow diagram shown in Fig. 5-9. Starting with the inviscid velocity distribution over an airfoil, the bubble model is invoked when laminar separation is predicted. After removal of the Goldstein singularity, $(R_{\delta_2})_S$ is determined and, based on the inviscid velocity gradient at the laminar separation point, an initial estimate of Gaster's parameter, P, is made. These two parameters are necessary to estimate the angle that the separating streamline makes with the surface. The velocity distribution in the plateau region is prescribed by means of the velocity plateau function which depends both on P and on the matching of its slope to that

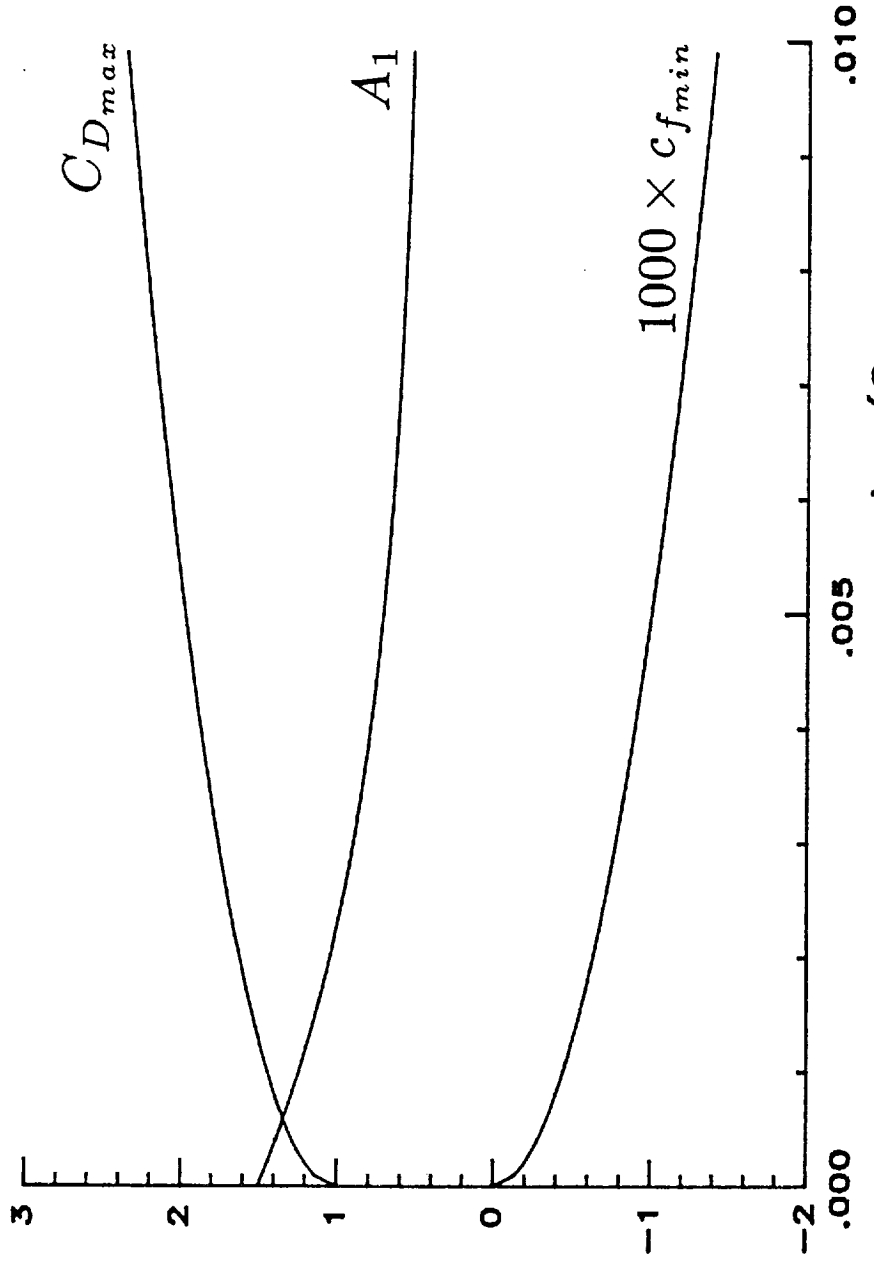

Fig. 5-8 Variation of supplemetary parameters with bubble height at transition.

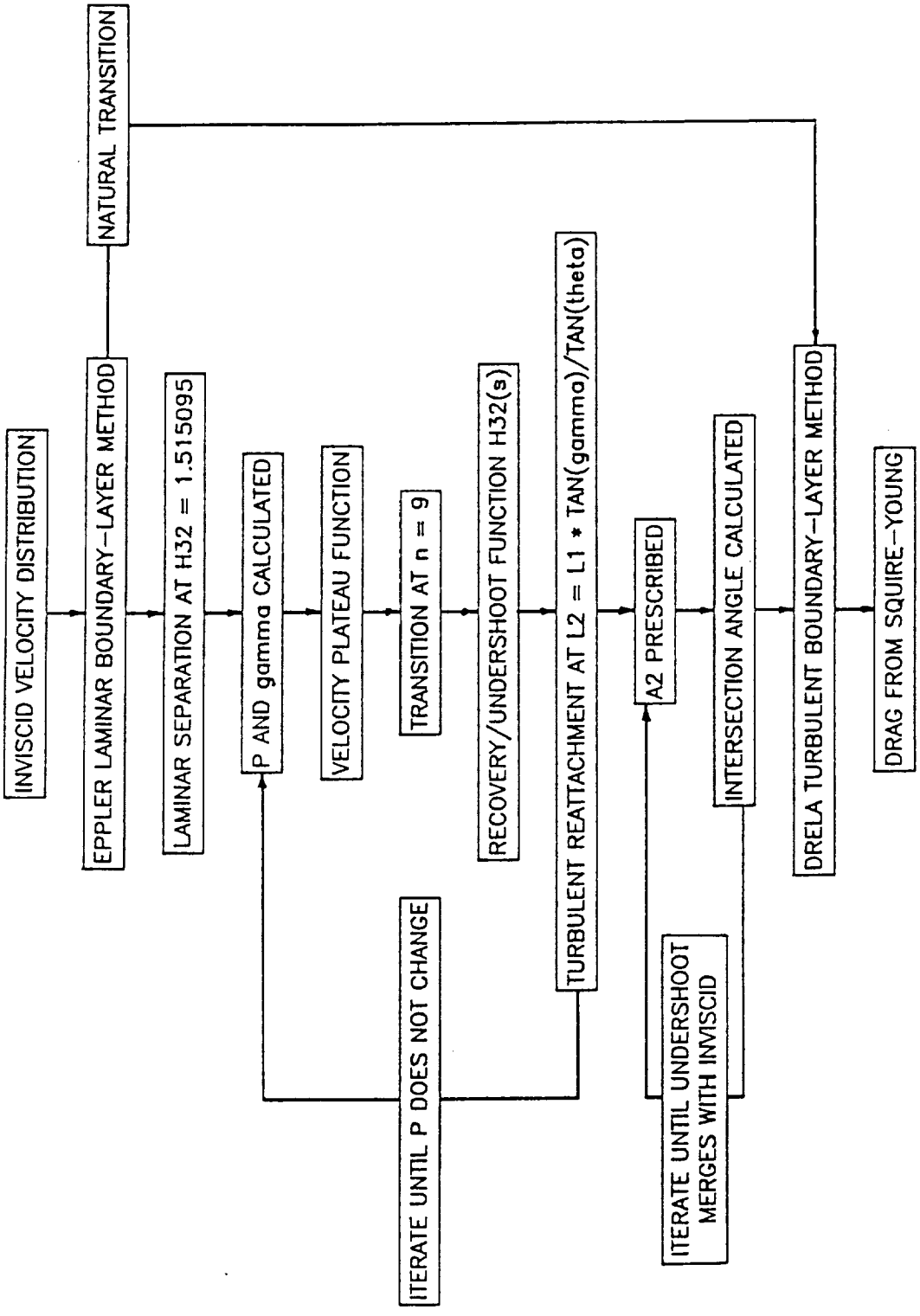

Fig. 5-9 Flowchart of procedure for modelling laminar separation bubbles.

of the inviscid velocity distribution at the laminar separation point. The separated shear layer development can thus be calculated in the direct mode using the momentum and energy integral equations. The laminar length of the bubble extends to the point where the amplification factor $n = 9$. This length times the tangent of the separation angle gives the thickness of the bubble at transition. From this height, knowledge of the spreading angle of the turbulent shear layer allows the calculation of the turbulent length of the bubble. The value of the inviscid velocity corresponding to this known reattachment location can be used to obtain a new value for P, such that the laminar calculations can be iterated until P reaches a fixed value. Upon convergence, the shear layer development in the turbulent part of the bubble is calculated by prescribing the distribution of H_{32} and solving the integral boundary-layer equations in the inverse mode together with turbulent closure relations based on Drela's but modified to model better the reattachment process. Upon the intersection of the undershoot with the inviscid distribution, the boundary-layer development is calculated in the direct mode using the inviscid pressure distribution to drive Drela's unmodified non-equilibrium turbulent to the trailing edge, where the drag is obtained with the Squire-Young [1937] formula.

The equations used in the different parts of the bubble model are summarized in the Appendix.

Chapter 6

RESULTS

In this chapter, the bubble model will be tested by comparing its predictions to available experimental measurements. These include mostly drag polars and pressure distributions for several airfoils but also two sets of Laser-Doppler Velocimetry measurements inside the bubble. The Reynolds number of these tests ranges from $2,000,000$ down to $100,000$.

NACA 66_3-018 Airfoil

The NACA 66_3-018 airfoil was one of the first to be tested for which the effect of the bubble on the pressure distribution could be clearly seen. Figs. 6-1 and 6-2 show a comparison between the predicted pressure distribution and boundary-layer developments and those measured by Gault [1955]. It can be seen that away from the bubble the inviscid pressure distribution is quite satisfactory. To the right of the plot is a blow-up of the bubble pressure distribution. The two asterisks represent the "viscous" separation and the reattachment points. The local inverse solution near separation with H_{12} prescribed employed to remove the separation singularity results in a rounding of the discontinuity in the velocity gradient upstream of separation and in some upstream influence of the bubble on the pressure distribution. Although this is achieved by purely numerical means, the correct local behavior seems well captured. The growth of the amplification factor is plotted along the airfoil surface itself in units of percentage chord. This curve is plotted as function of x/c rather than arc-length for consistency with the pressure distribution. Thus, the end of the curve, at $n = 9$, lies a distance equal to 9% of the airfoil chord above the airfoil's y-coordinate corresponding to the transition location. For this case, all

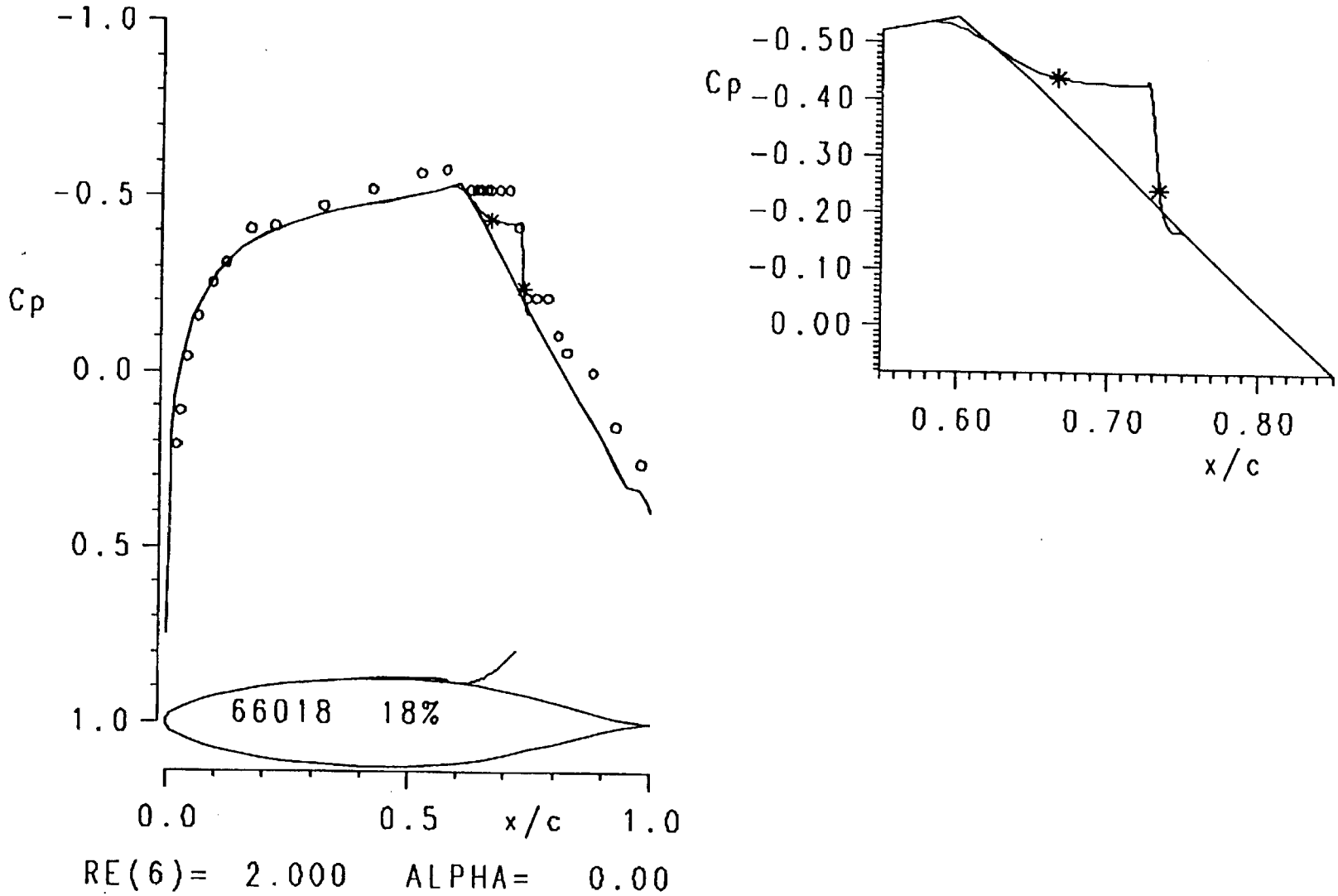

Fig. 6-1 (a) Comparison of predicted and measured pressure distribution for the NACA 66_3-018 airfoil, $\alpha = 0°$. Data are from Gault [1955].

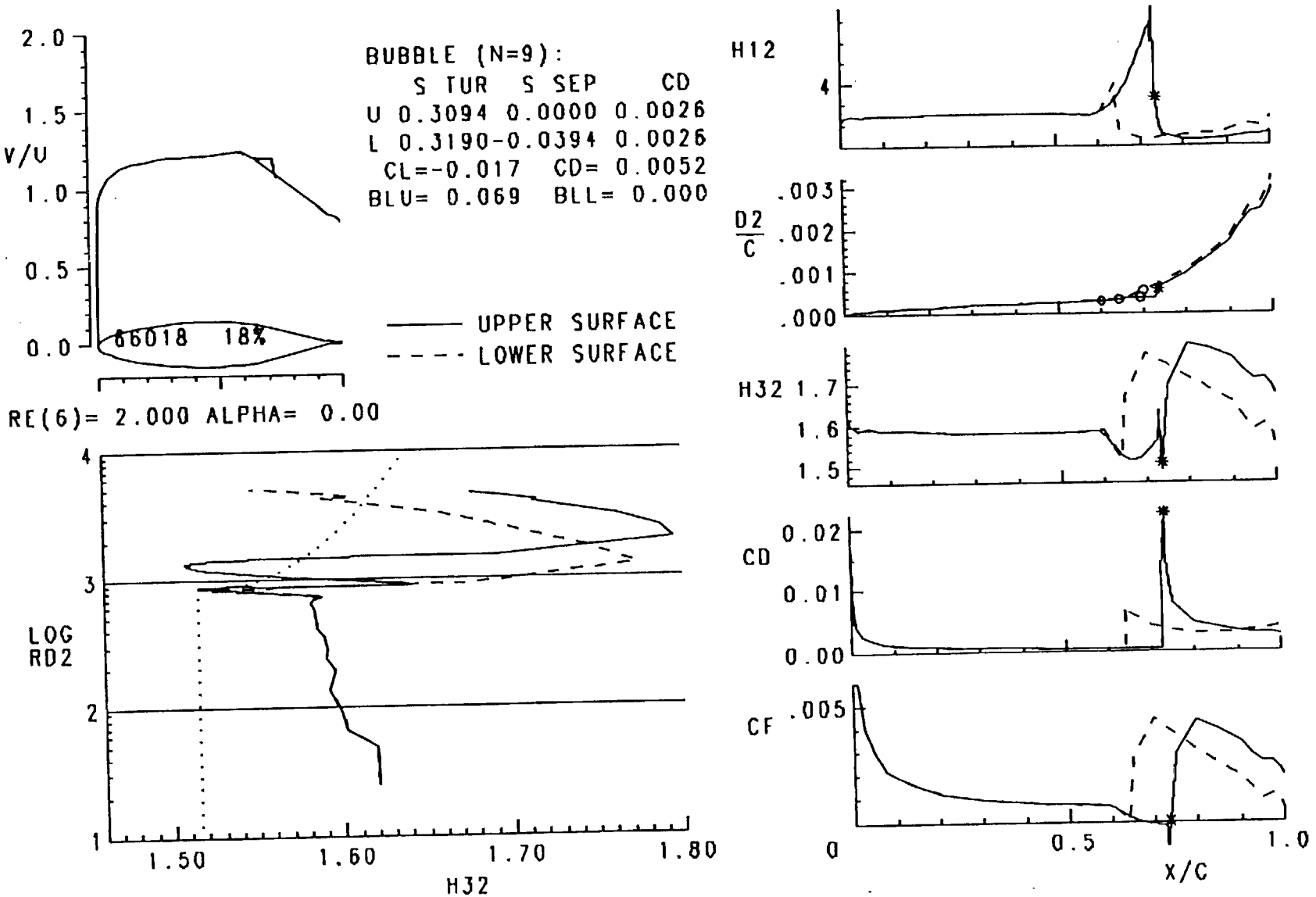

Fig. 6-1 Cont. (b) Viscous analysis summary and boundary-layer development for the NACA 66_3-018 airfoil, $\alpha = 0°$. Data are by Gault [1955].

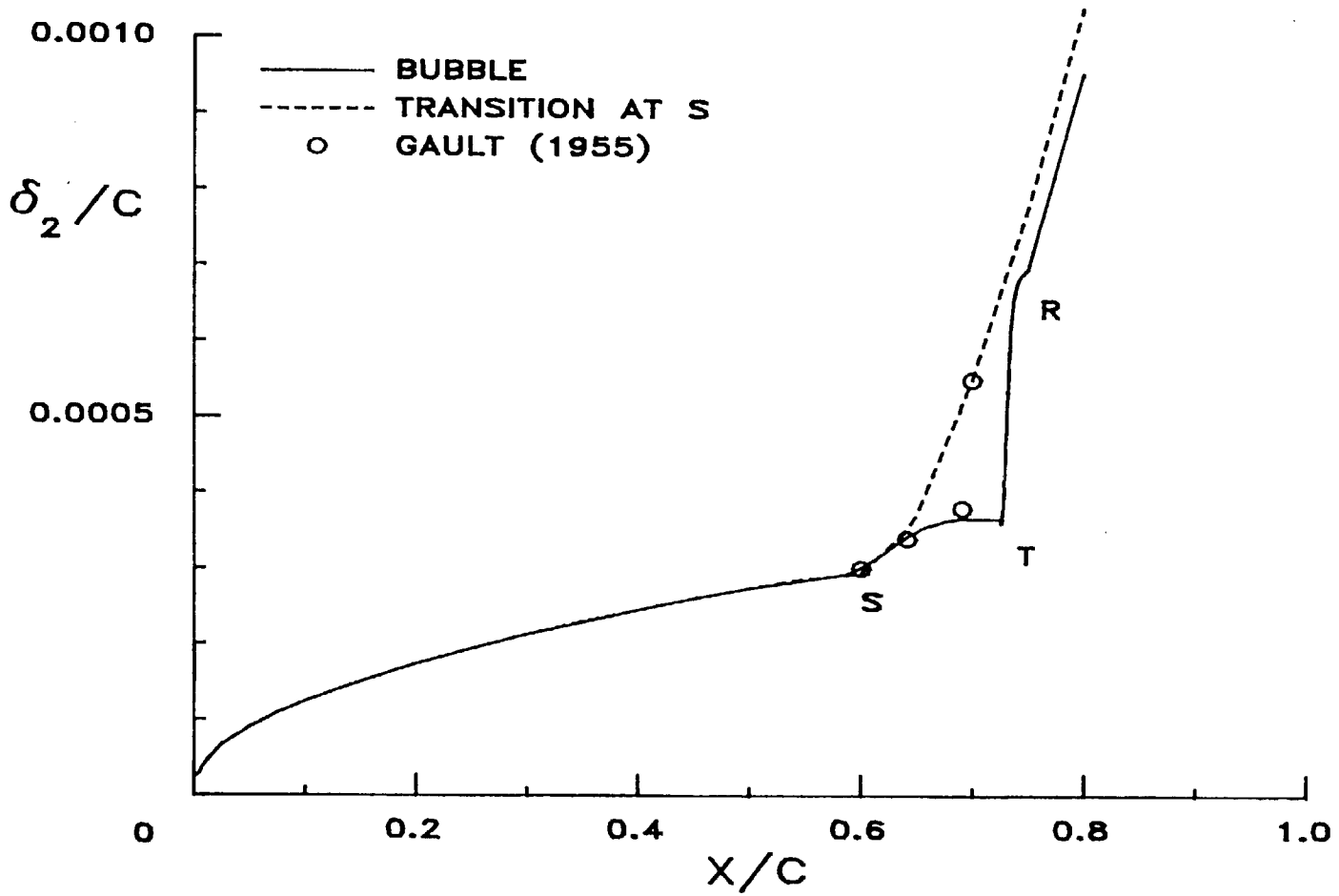

Fig. 6-2 Comparison of momentum thickness growth inside the bubble with that obtained by assuming transition at laminar separation. NACA 66_3-018 airfoil, $\alpha = 0°$. Data are by Gault [1955].

of the amplification occurs after laminar separation.

Fig. 6-1(b) contains all the relevant inputs and outputs of the boundary-layer analysis. The inviscid velocity distribution is provided for reference together with the Reynolds number and angle of attack. The calculated bubble is drawn on this plot. The summary of the viscous analysis as printed out by the Eppler and Somers program is printed to the right, below the label indicating that a bubble analysis has been performed with transition at $n = 9$. This includes the extents of turbulent and separated arc lengths normalized with respect to the chord, as well as the drag coefficients from the upper and lower surfaces. The lift and the total drag coefficients are printed next, and the bubble lengths on the upper and lower surfaces come last. The Eppler boundary-layer development plot is shown below. This plot is especially useful during the design process. Finally, all five boundary-layer variables are plotted as functions of x/c, with the asterisk denoting the reattachment point. The removal of the Goldstein singularity can be clearly seen in the smooth developments through the separation point.

This figure serves to illustrate several points. Since the airfoil is symmetrical and $\alpha = 0$, by suppressing the bubble model on the lower surface the present prediction using the model and Drela's turbulent boundary-layer method can be compared with the original Eppler turbulent boundary-layer analysis starting at the laminar separation point. With the exception of the bubble region, the two methods give very similar results, as expected. The difference in separation point locations with and without Goldstein's singularity can be seen from the plot of H_{12} *vs.* x/c. At the bottom left of the figure Eppler's boundary-layer development plot shows that laminar separation for this airfoil occurs at the boundary with natural transition according to the modified transition criterion Eq. (4.5). The e^n analysis, however, indicates that n at separation is still quite small. This apparent

inconsistency of Eppler's transition criterion may be resolved by realizing that it was calibrated using mainly drag data. For this case, the drag of the upper and lower surfaces is identical. Therefore, the bubble does not seem to cause any deterioration in airfoil performance. The experimental values of momentum thickness inside the bubble, derived from Gault's data by Roberts [1980], support this interpretation. As shown more clearly in Fig. 6-2, a bubble may not necessarily lead to an increase in momentum thickness greater than if transition had been assumed at laminar separation. In fact, as will be shown later, below a certain length a mid-chord bubble appears to reduce the airfoil drag. The growth in momentum thickness in the laminar part of the bubble is clearly evident. The calculated transition point is a few percent chord too far downstream. As the length of the plateau in the laminar part shown in Fig. 6-1(a) is quite close to the experimental, transition may indeed start before any change in the pressure is observed, as maintained by Russell [1978].

NASA NLF(1)-1015 Airfoil

This airfoil was recently tested in the NASA Langley Low-Turbulence Pressure Tunnel. Drag polars calculated from force measurements for lift, wake surveys for drag, and also detailed pressure distribution measurements were obtained at $R = 2,000,000$, $1,000,000$, $700,000$, and $500,000$. The profile was designed for use on a high-altitude long-endurance RPV and is therefore characterized by a large aft-loading to achieve the high c_ℓ requirement. It was also designed to minimize the effects of the bubbles at the design conditions of $R = 2,000,000$ for a high-speed dash (bottom of the low-drag bucket) and $R = 700,000$ for maximum endurance (top of low-drag bucket). The present predictions are compared with the $R = 500,000$ data since here the effects of the bubble are most clearly seen.

Fig. 6-3 shows the aerodynamic characteristics of this airfoil on the plot as generated by the original Eppler and Somers program. Shown is the original prediction

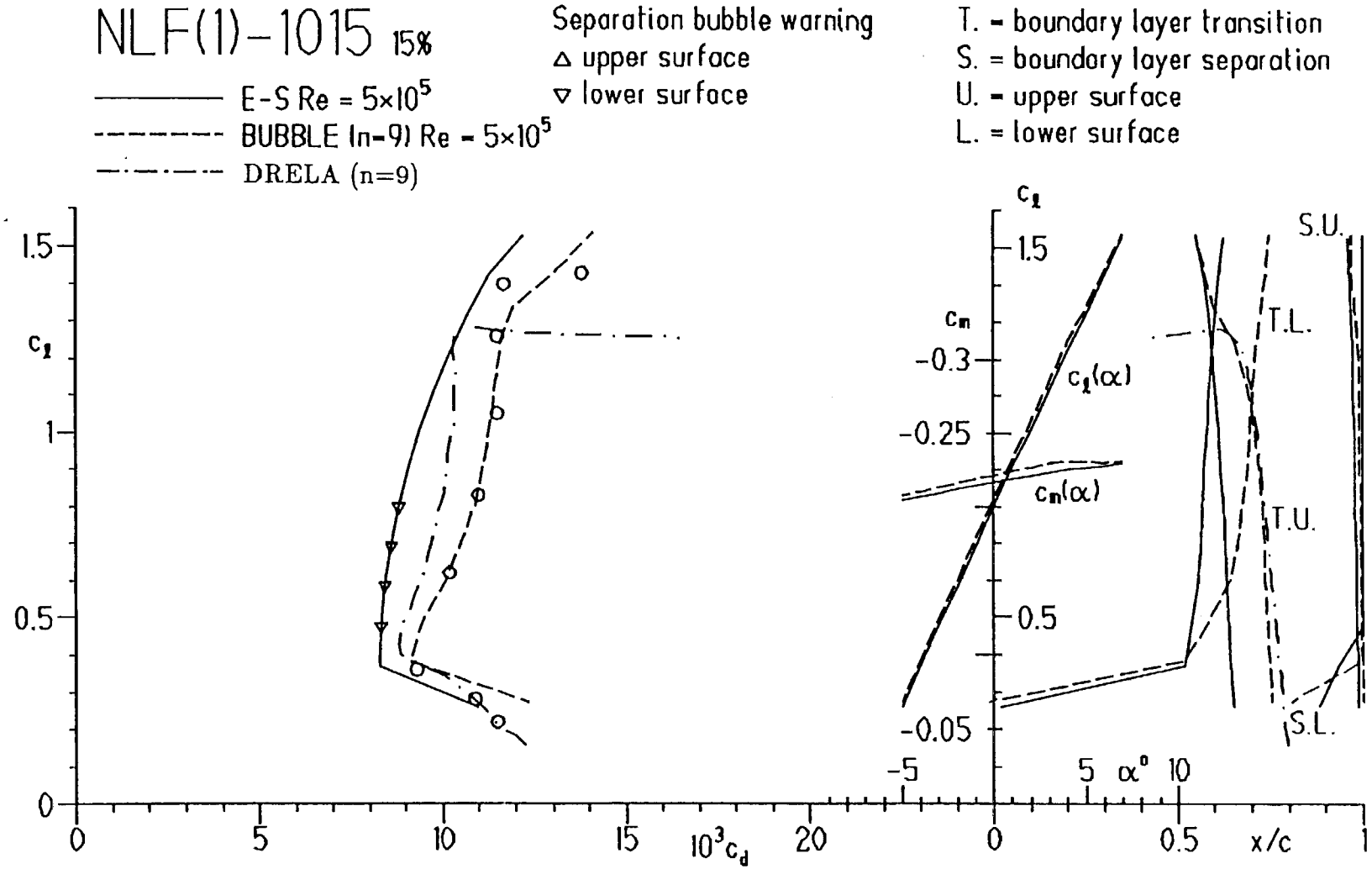

Fig. 6-3 Aerodynamic characteristics of the NASA NLF(1)-1015 airfoil obtained with the original Eppler and Somers program compared with those obtained with the present bubble model and with the interactive program XFOIL of Drela, $R = 500,000$. Data are from the Low-Turbulence Pressure Tunnel, NASA LaRC, 1987.

obtained by assuming transition at laminar separation, the prediction of the present model, Drela's XFOIL results, and the experimental data from LTPT. Part of the difference in drag prediction between the original program and the present version is due to the different turbulent boundary-layer methods employed, as shown in Fig. 2-4. In fact, comparing Figs. 2-4 and 6-3, it can be inferred how at the top of the bucket the bubble leads to a drag reduction over what is calculated by assuming transition at laminar separation. In any case, the present formulation is able to reproduce the measured data with excellent accuracy. At the upper and lower limits of the polar, the onset of strong global interaction cannot be neglected. At these conditions, the present lift and drag predictions are poorer. The plot also contains the lift and moment curves as functions of α as well as the transition and turbulent separation locations as functions of x/c. In actuality, although the program labels the axis as "x/c," the independent variable is really "$1 - s_{turb}/c$," a rather more cumbersome variable. Given that there is usually very little difference between the two variables, x/c is used for ease of presentation. Since the original version of the program assumes transition at the laminar separation point, the difference between the transition curves for the two analyses represents the laminar length of the bubble. It can be seen how the bubble decreases in size and eventually disappears as the pressure distribution upstream of laminar separation becomes increasingly adverse. This will be clearly shown in subsequent plots. Because the XFOIL transition locations are given in terms of actual x/c, they appear to occur downstream of transition as calculated by the present model. As will be shown below, however, they occur upstream.

Matching the experimental drag polar does not by itself guarantee an accurate prediction. The pressure distribution and the boundary-layer development should also be compared to experimental data. Unfortunately, it is much more difficult

to measure these quantities. Consequently, few data sets are available. For the NLF(1)-1015 airfoil, the details of the bubble flowfield can be checked only through the pressure distribution, since no boundary-layer data were taken. Figs. 6-4 to 6-6 show typical comparisons with the measured pressure distributions together with the corresponding calculated developments. Fig. 6-4(a) shows the pressure distribution corresponding to the lowest value of c_ℓ on the polar together with the XFOIL prediction. Two very different bubbles can be seen, one at the mid-chord on the upper surface and the other at the leading edge on the lower surface. Both bubbles are well approximated by the model. XFOIL gives a slightly shorter bubble on the upper surface and a very slight perturbation on the pressure distribution on the lower. Fig. 6-4(b) shows the boundary-layer development. It is interesting to see how large the values of the shape factors can become inside leading-edge bubbles. These, in any case, do not seem to contribute much to increasing the drag of the airfoil. The shape of the $\sin(1/x)$ function can be clearly recognized in the mid-chord bubble. The values for $C_{D_{max}}$ are very similar, the greater increase in δ_2 of the upper-surface bubble being largely due to the longer extent of its turbulent part. This bubble, in fact, is much thicker at the transition point than the leading-edge bubble. The distribution of c_f seems plausible. In any case, in this region this variable has little impact on the boundary-layer development or on the pressure distribution.

Fig. 6-5(a) shows the pressure distribution at an angle of attack corresponding to the middle of the airfoil polar. In an attempt at matching the pressure gradient along the bubble, the inviscid angle of attack is one degree less than the experimental. It can be seen, however, that the strong trailing-edge interaction induced by the large aft-loading prevents the matching of the gradients on both surfaces simultaneously. In any case, the model reproduces the measured pressure distribu-

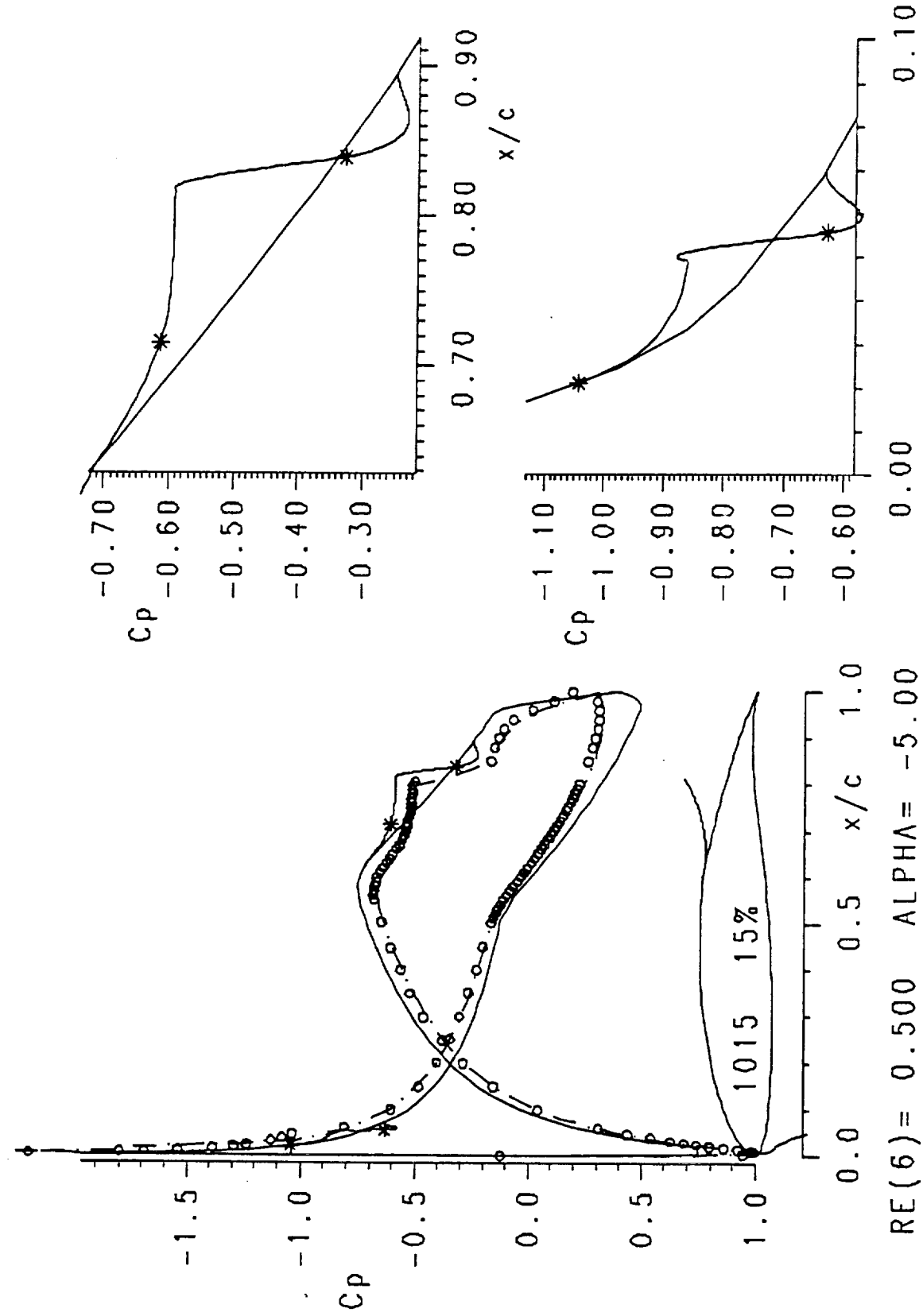

Fig. 6-4 (a) Comparison of predicted and measured pressure distribution for the NASA NLF(1)-1015 airfoil, $\alpha = -5°$. Dot-dashed line is XFOIL prediction. Data are from the Low-Turbulence Pressure Tunnel, NASA LaRC, 1987.

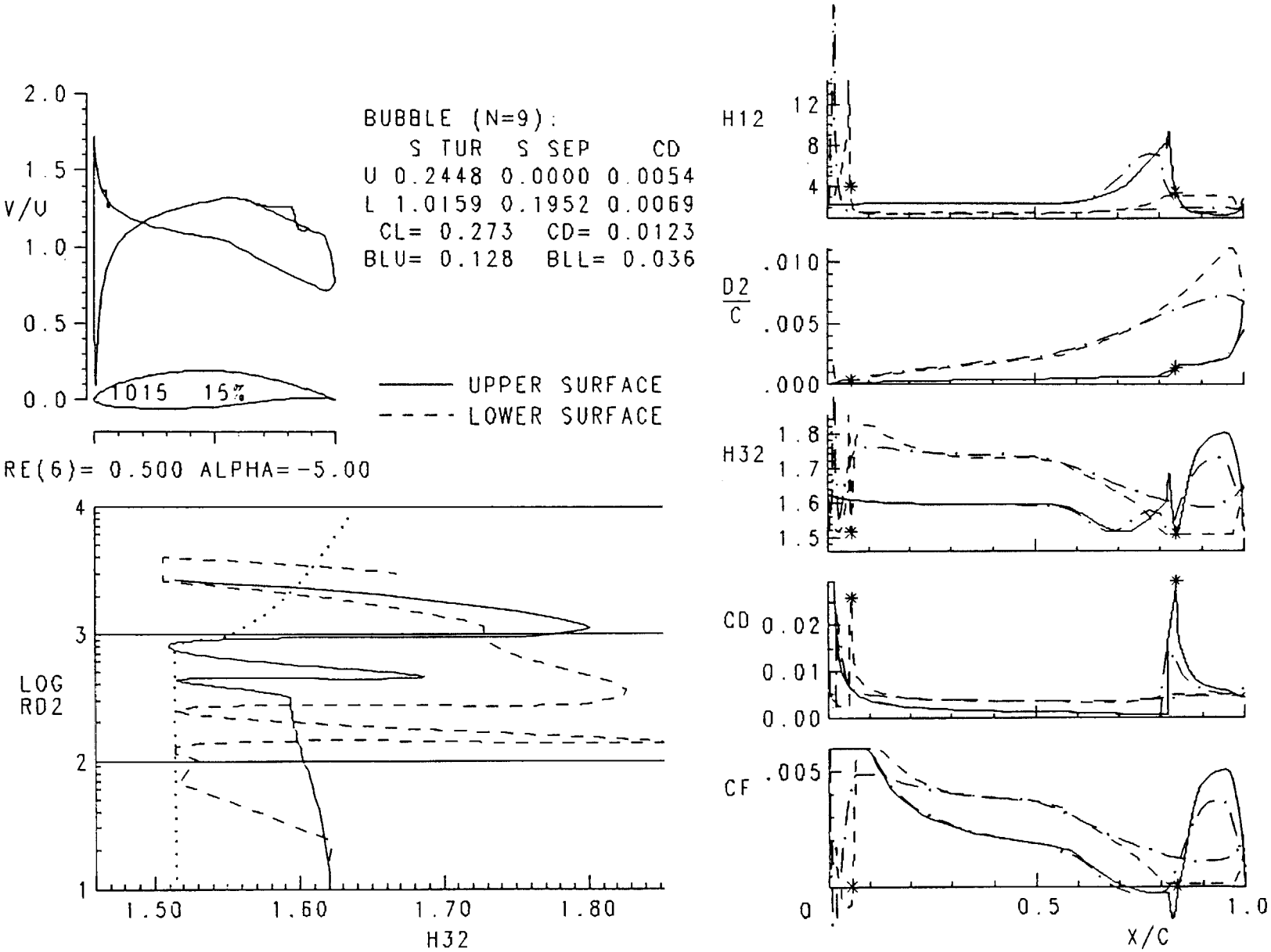

Fig. 6-4 Cont. (b) Viscous analysis summary and upper surface boundary-layer development compared with XFOIL prediction for the NASA NLF(1)-1015 airfoil, $\alpha = -5°$.

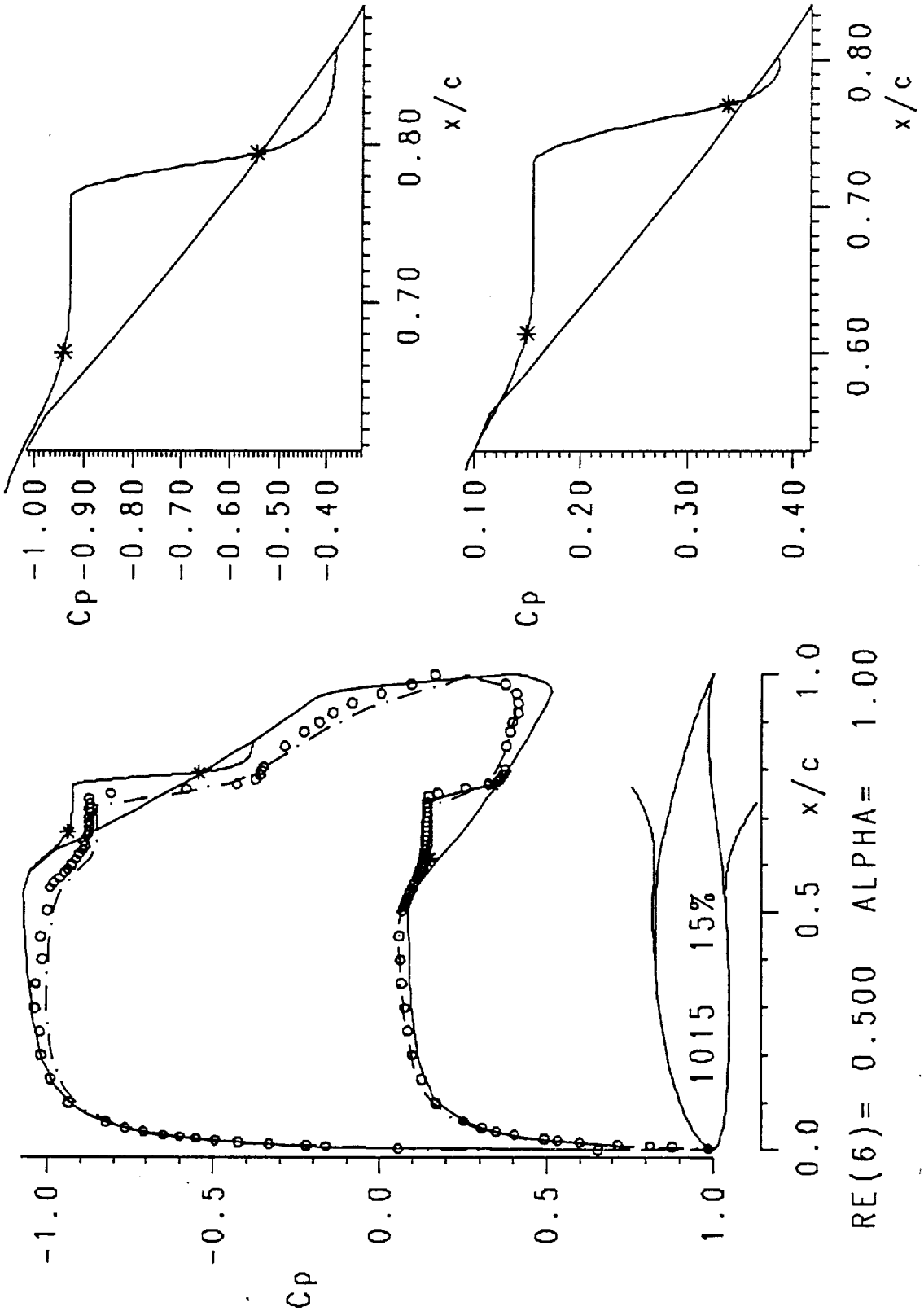

Fig. 6-5 (a) Comparison of predicted and measured pressure distribution for the NASA NLF(1)-1015 airfoil, experimental $\alpha = 2°$. Dot-dashed line is XFOIL prediction at $\alpha = 2°$. Data are from the Low-Turbulence Pressure Tunnel, NASA LaRC, 1987.

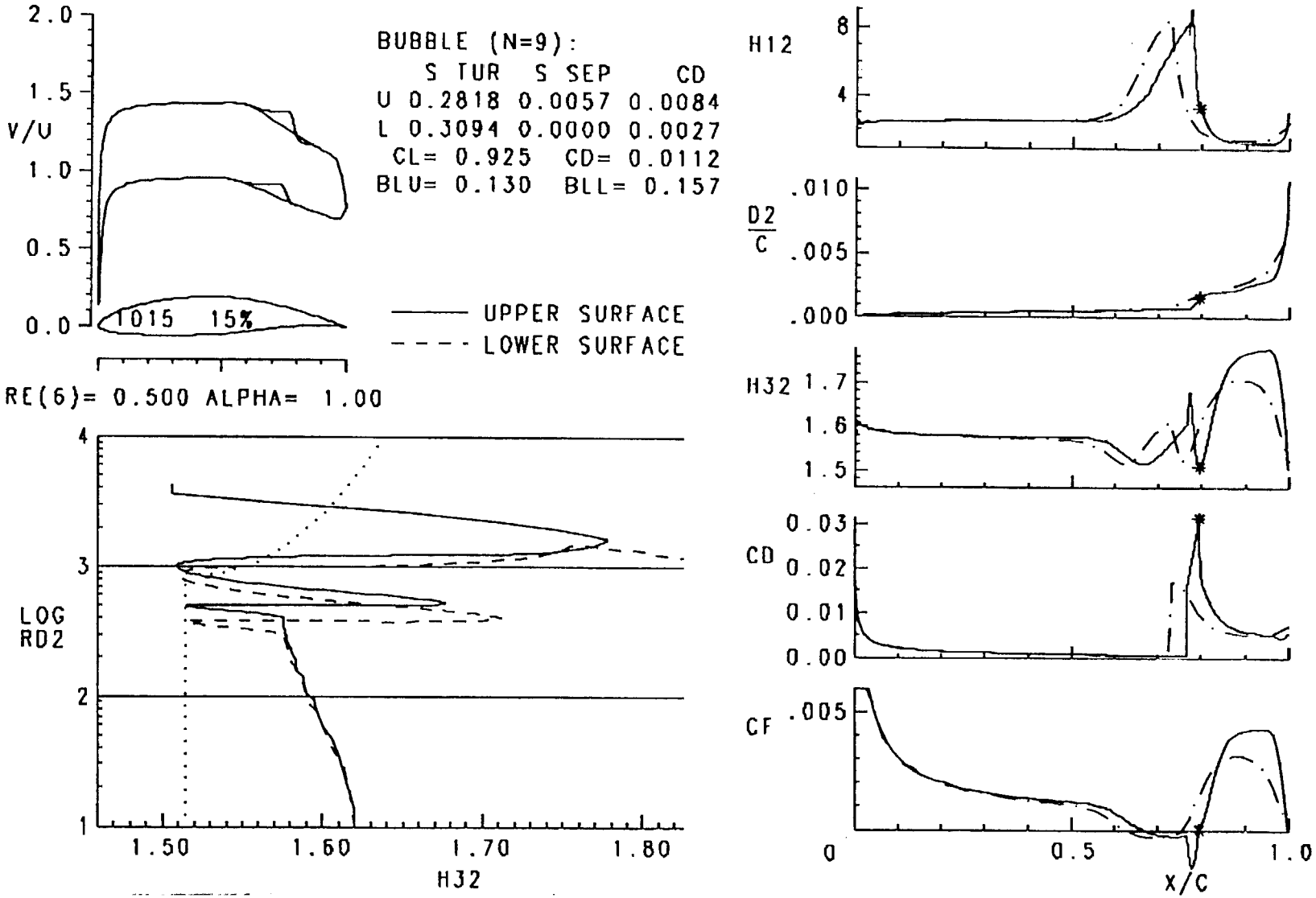

Fig. 6-5 Cont. (b) Viscous analysis summary and upper surface boundary-layer development at $\alpha = 1°$ compared with XFOIL prediction at $\alpha = 2°$ for the NASA NLF(1)-1015 airfoil.

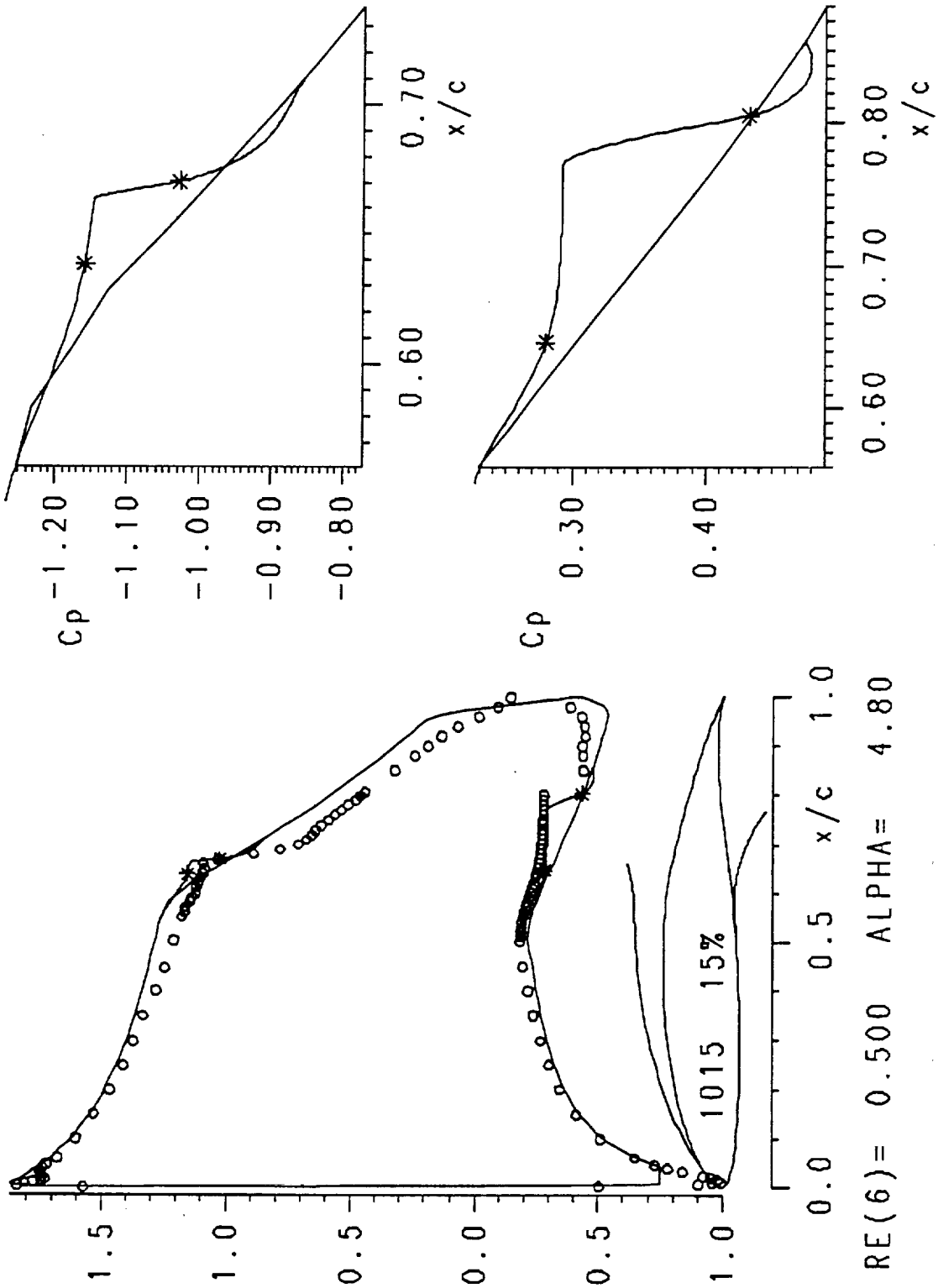

Fig. 6-6 (a) Comparison of predicted and measured pressure distribution for the NASA NLF(1)-1015 airfoil. Experimental $\alpha = 6°$. Data are from the Low-Turbulence Pressure Tunnel, NASA LaRC, 1987.

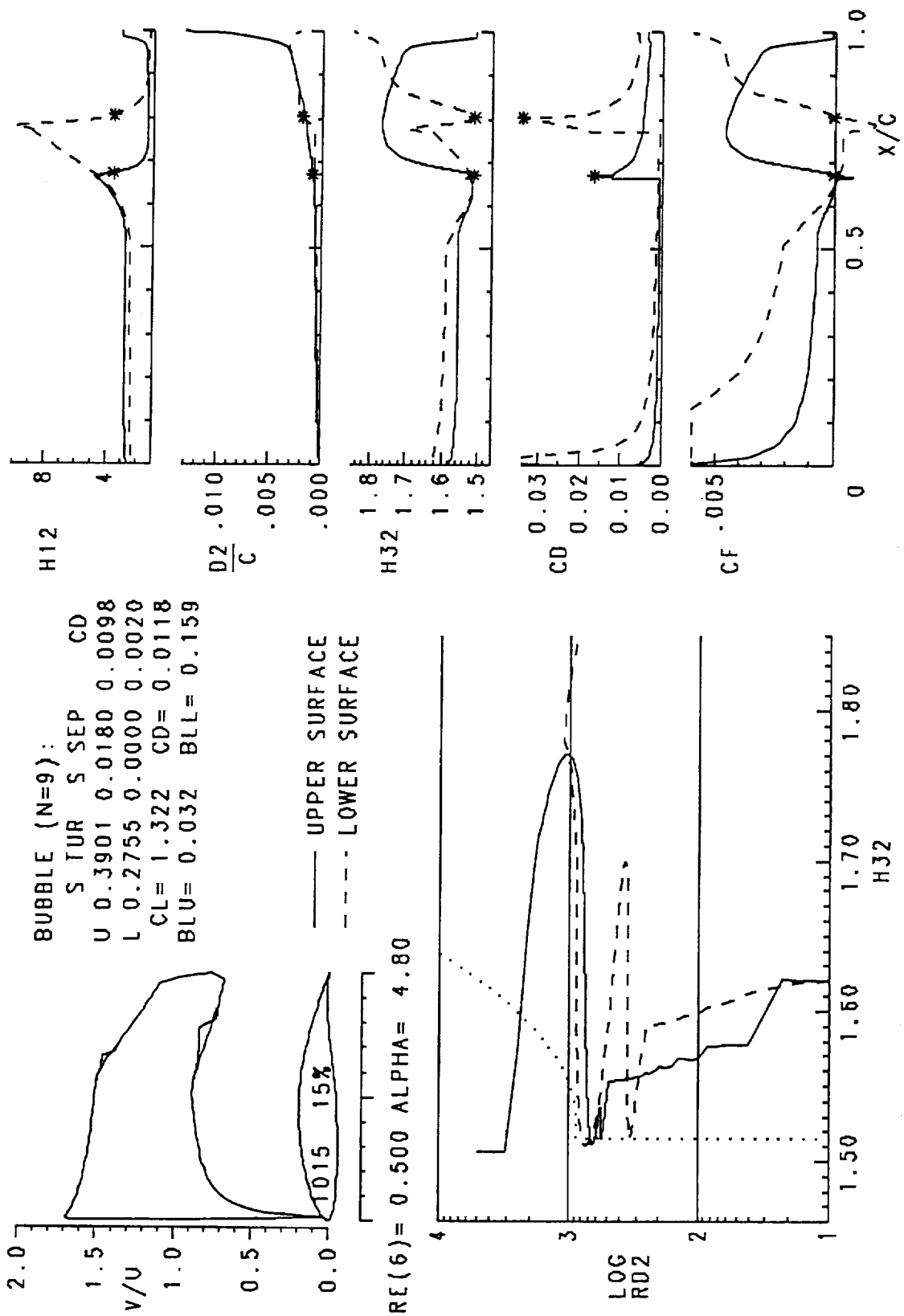

Fig. 6-6 Cont. (b) Viscous analysis summary and boundary-layer development for the NASA NLF(1)-1015 airfoil, $\alpha = 4.8°$.

tion remarkably well. Both the upper and lower surface bubbles are quite long and may be expected to be thick. In fact, as can be seen in Fig. 6-3, at this condition the drag due to the bubble is highest. The bubbles predicted by XFOIL are a little short although the same value of n was used. At this angle of attack, n is starting to be amplified upstream of laminar separation on the upper surface. The boundary-layer development is shown in Fig. 6-5(b), where the step in δ_2 in the turbulent part of the bubble is evident.

Fig. 6-6(a), finally, corresponds to the top of the bucket, where the upper surface bubble is about to disappear and the lower surface contributes little to the total drag. The short transition length in this case is believed to be a direct consequence of the destabilizing effect of the adverse pressure distribution upstream of separation. This is clearly shown by the distribution of n along the upper surface. In Fig. 6-6(b), the viscous analysis summary shows how the lower-surface drag is only a fifth of the upper-surface drag in spite of a 16%c long bubble. It is particularly interesting to observe how the upper-surface bubble is shrinking while preserving its proportions. This indicates that the correct scaling for the bubble has been identified. At a slightly higher angle of attack, the transition point corresponds to the laminar separation point. Beyond this condition, the transition point precedes the separation point and travels upstream until the rise of the suction peak again leads to laminar separation before transition and to the formation of a leading-edge bubble. As far as the effects on transition are concerned, therefore, it appears that the a destabilizing pressure distribution is entirely analogous to a rise in Reynolds number.

Eppler E387 Airfoil

This airfoil was designed more than twenty years ago and is intended for use on model gliders. It also was recently tested in the NASA Langley Low-Turbulence

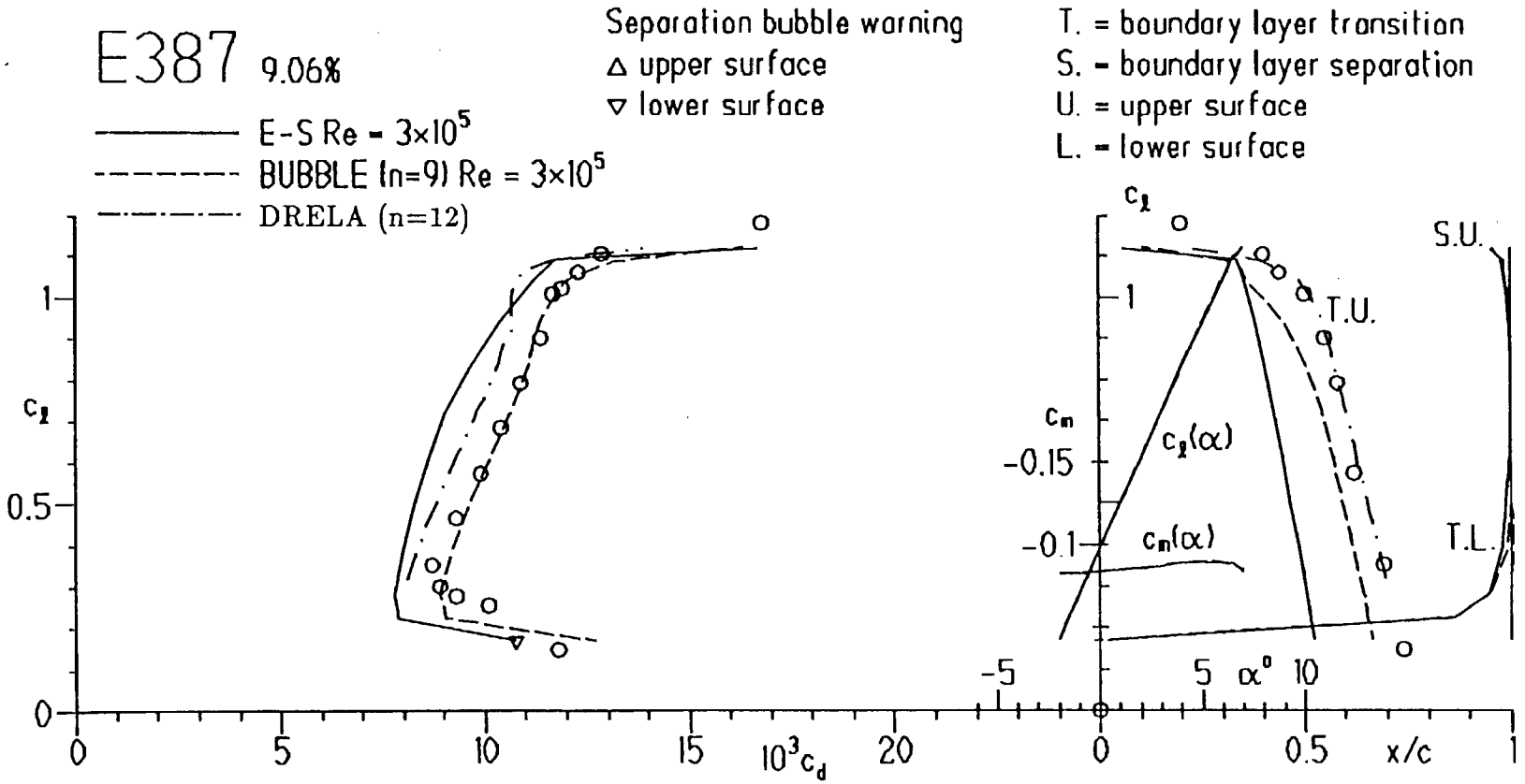

Fig. 6-7 Aerodynamic characteristics of the Eppler E387 airfoil obtained with the original Eppler and Somers program compared with those obtained with the present bubble model and with the interactive program XFOIL of Drela, $R = 300{,}000$. Data are from McGhee et al. [1988].

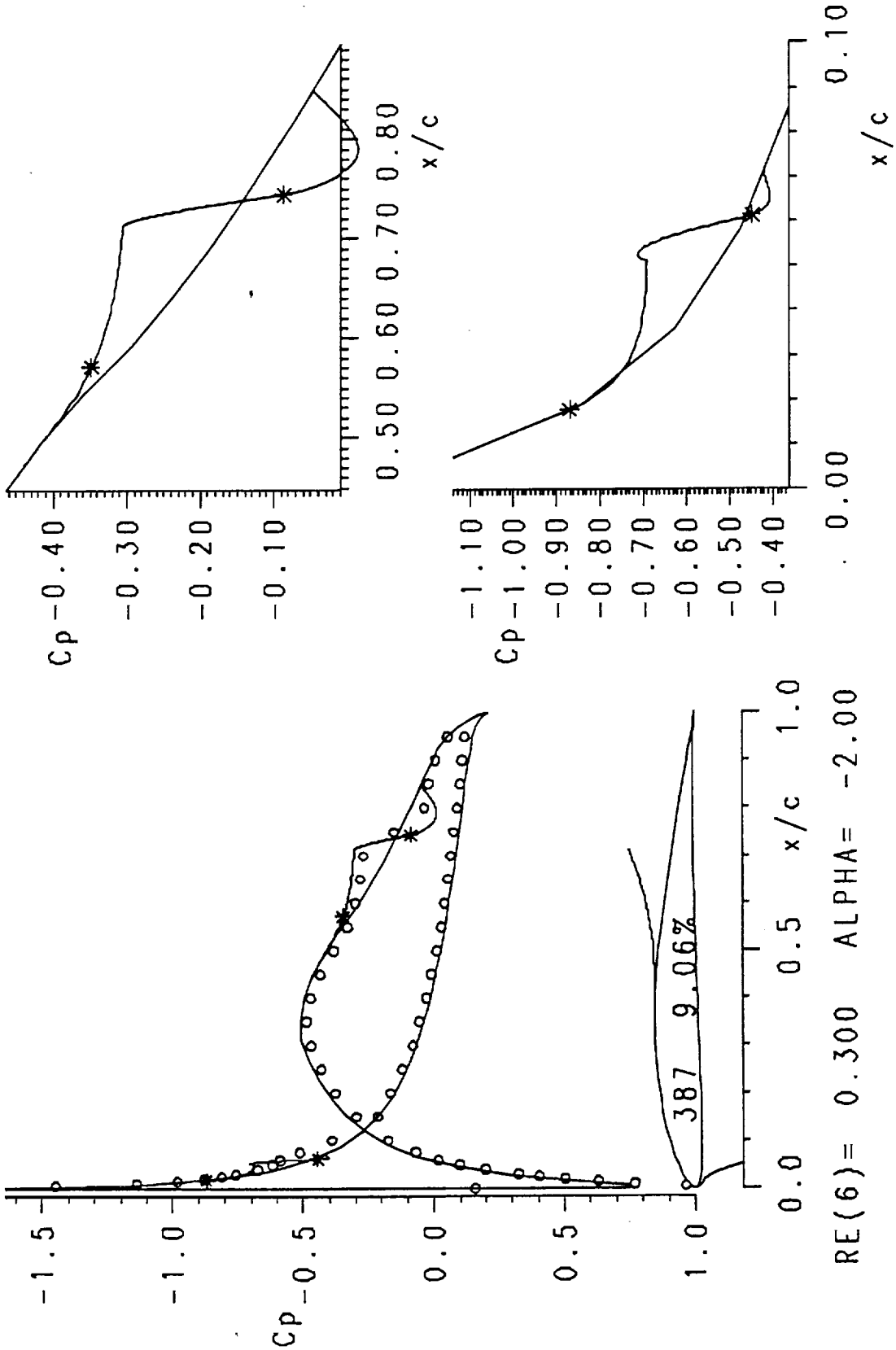

Fig. 6-8 (a) Comparison of predicted and measured pressure distribution for the Eppler E387 airfoil, $\alpha = -2°$. Data are from McGhee et al. [1988].

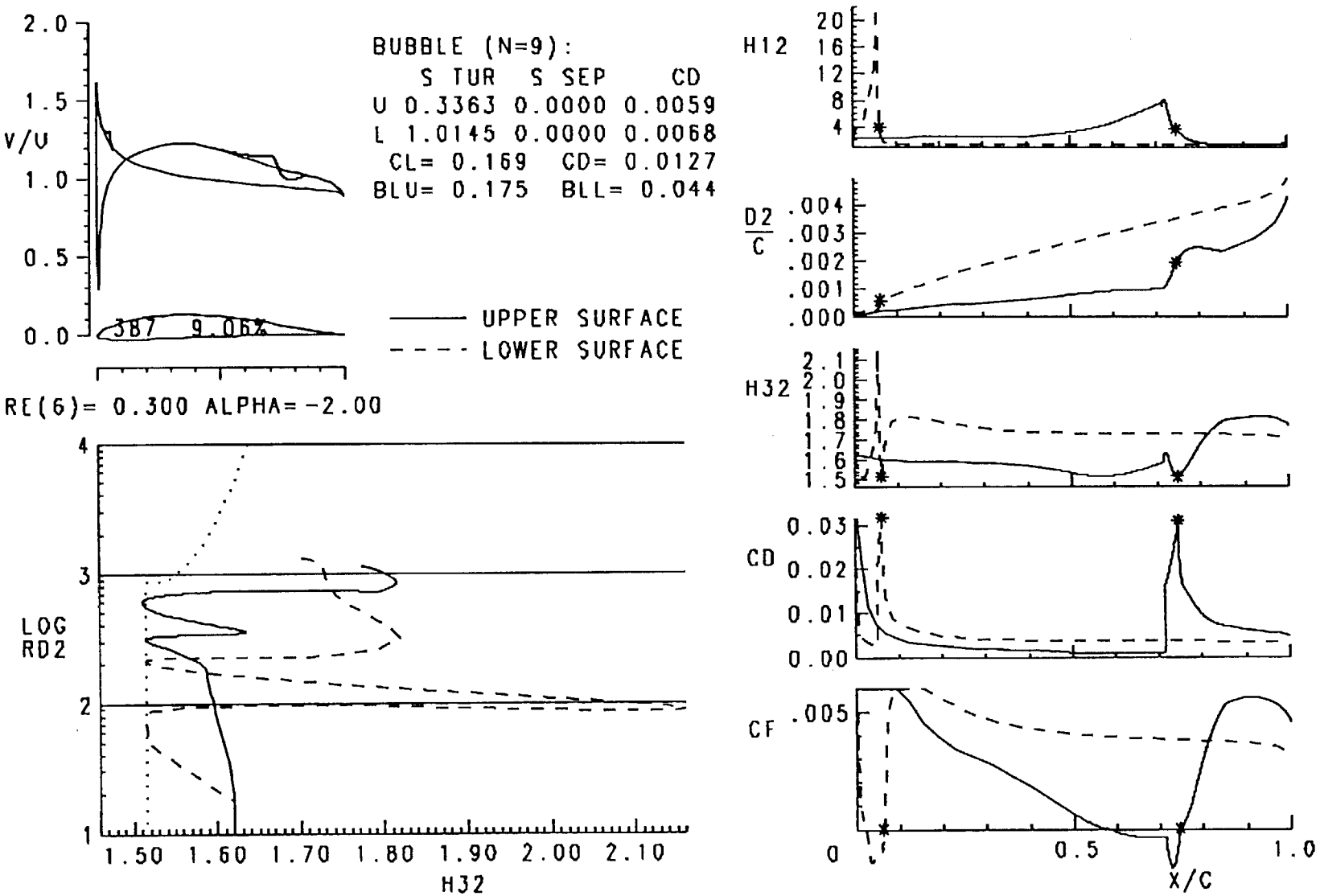

Fig. 6-8 Cont. (b) Viscous analysis summary and boundary-layer development for the Eppler E387 airfoil, $\alpha = -2°$.

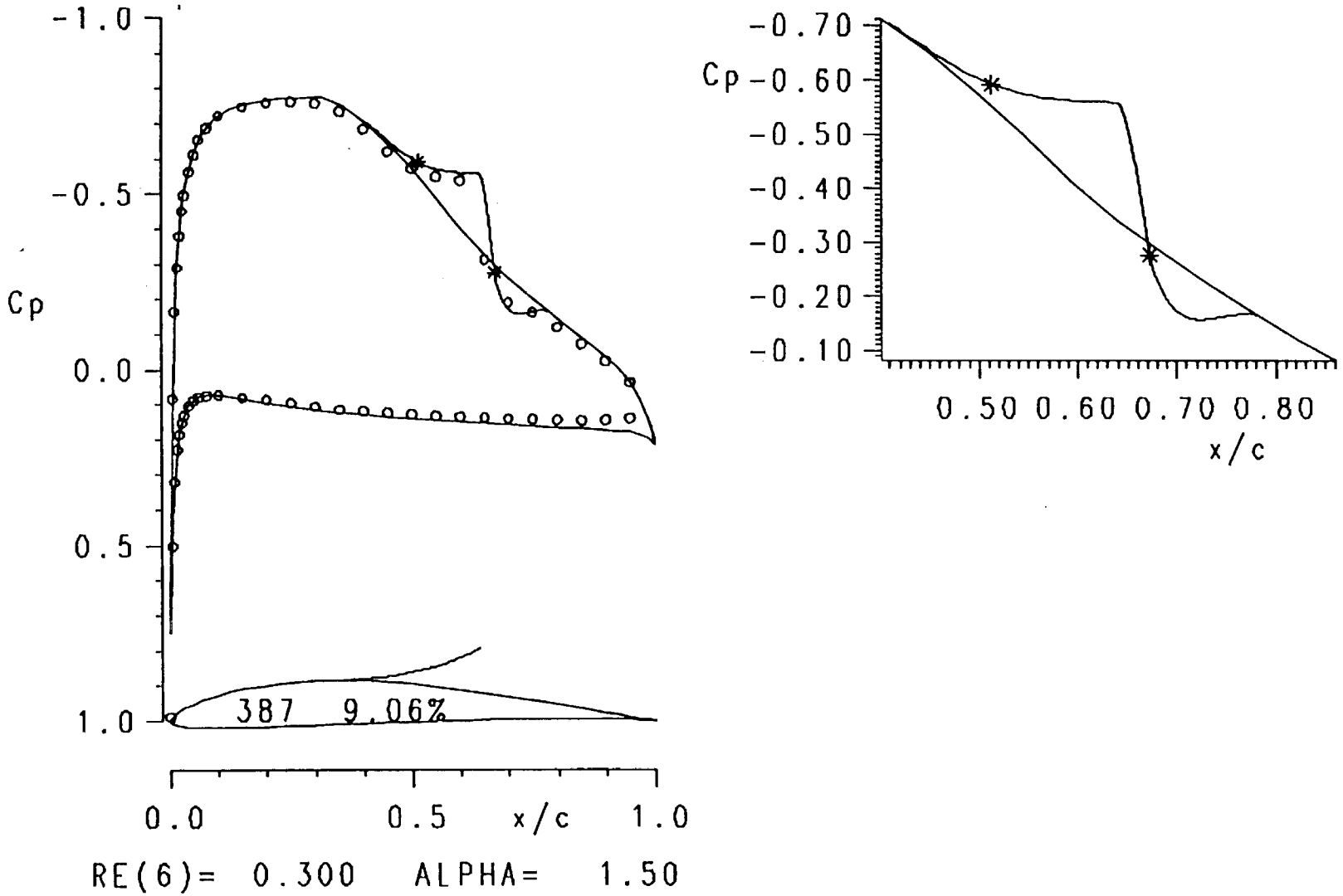

Fig. 6-9 (a) Comparison of predicted and measured pressure distribution for the Eppler E387 airfoil. Experimental $\alpha = 2°$. Data are from McGhee et al. [1988].

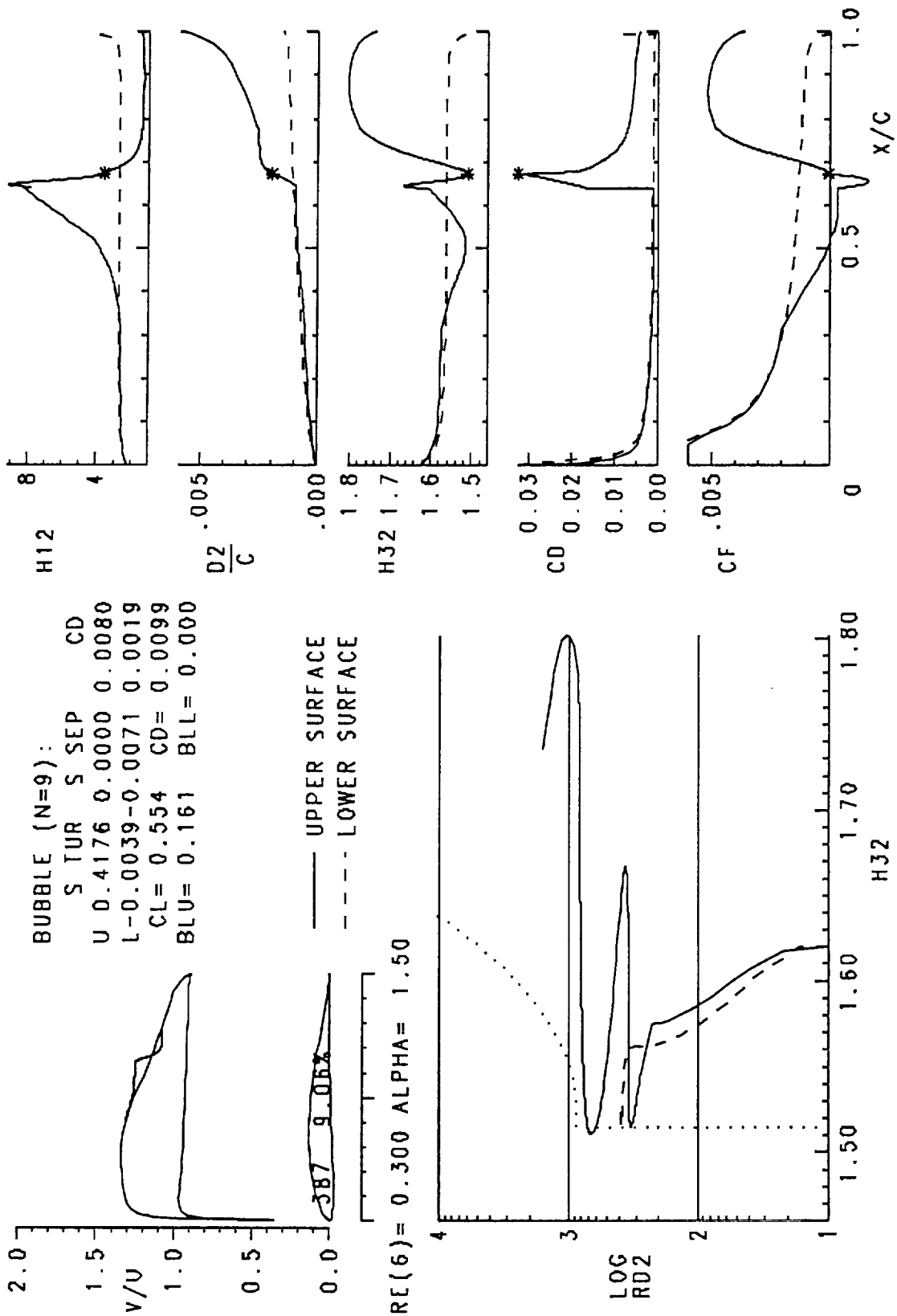

Fig. 6-9 Cont. (b) Viscous analysis summary and boundary-layer development for the Eppler E387 airfoil, $\alpha = 1.5°$.

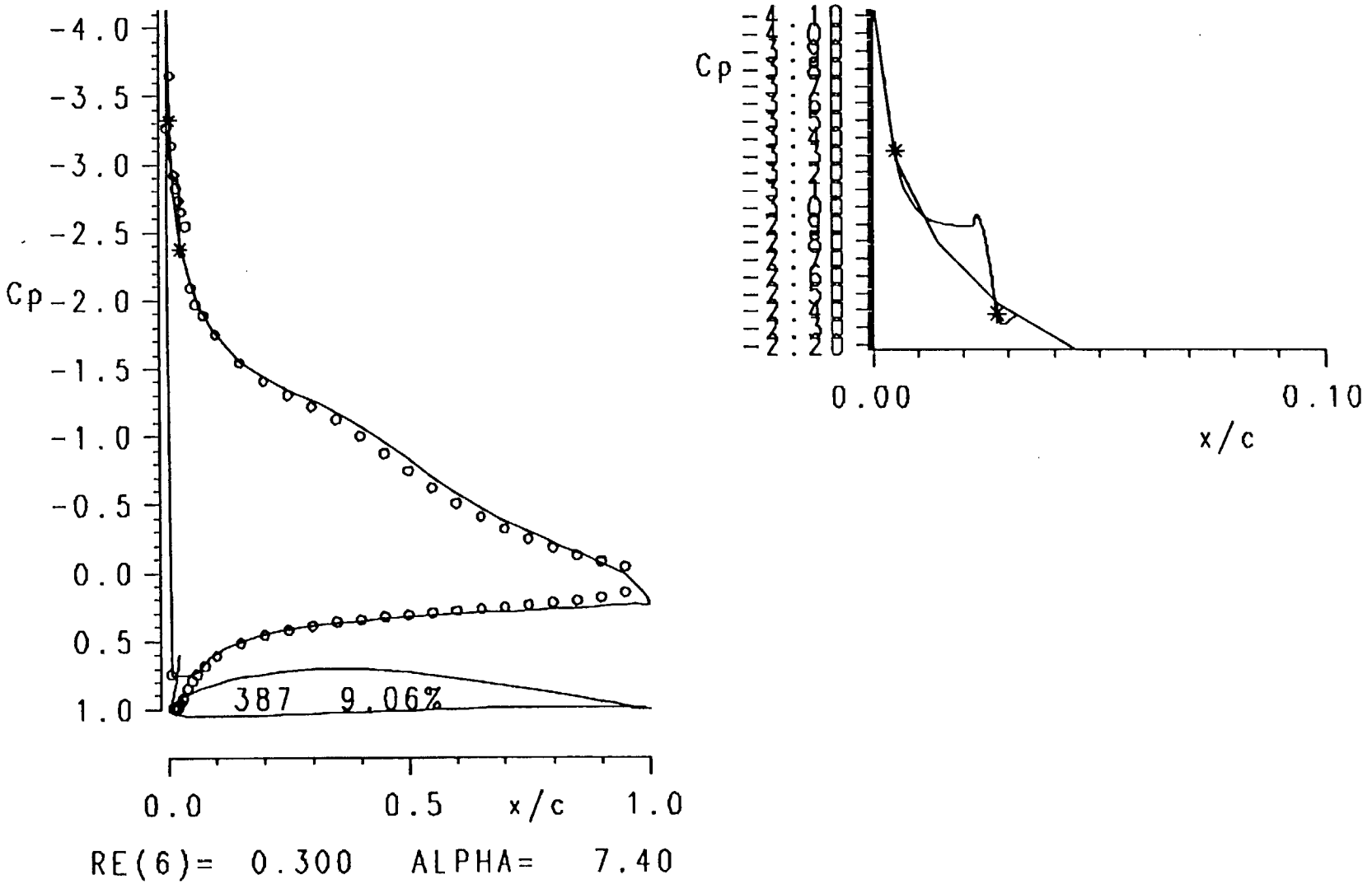

Fig. 6-10 (a) Comparison of predicted and measured pressure distribution for the Eppler E387 airfoil. Experimental $\alpha = 9°$. Data are from McGhee et al. [1988].

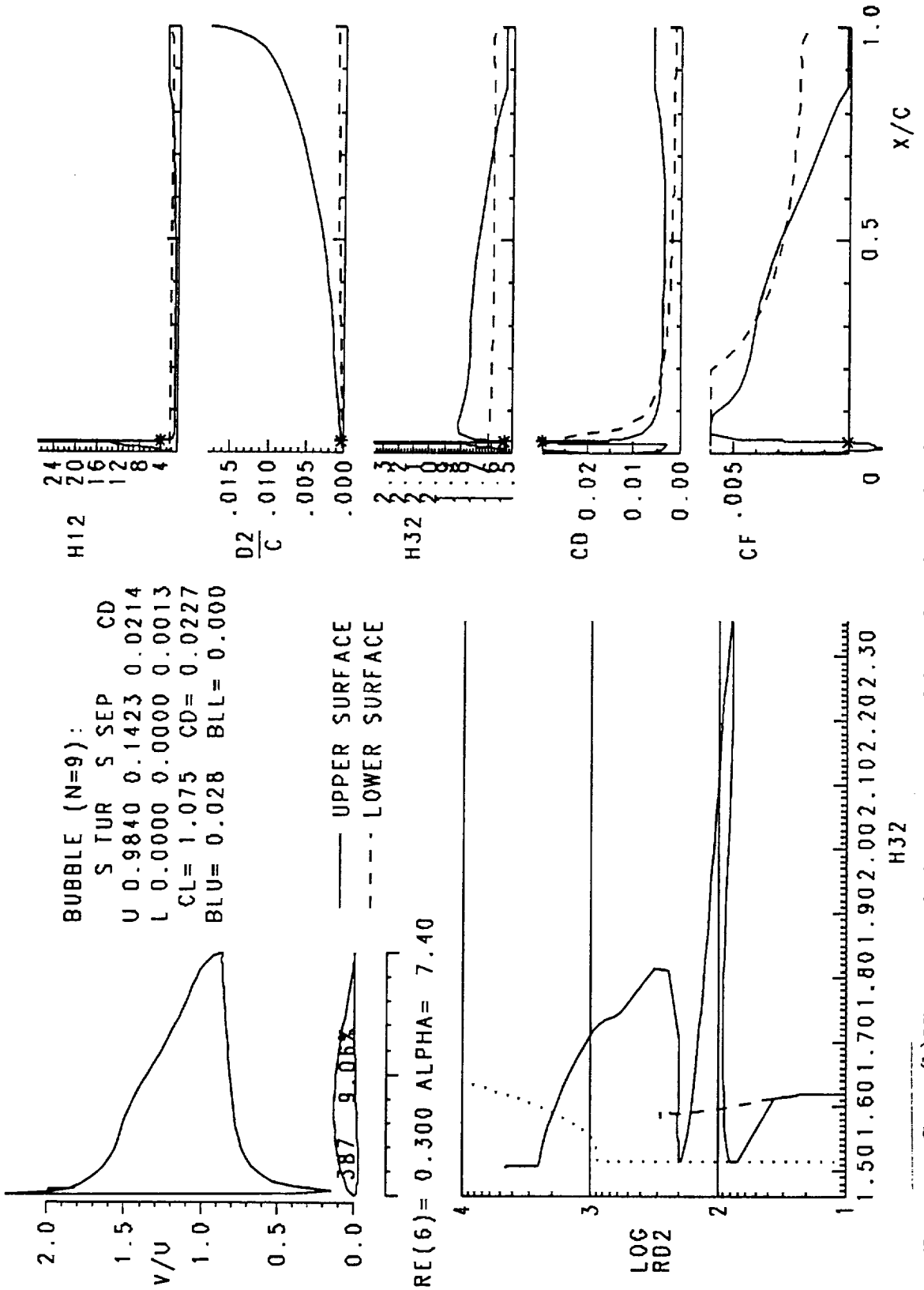

Fig. 6-10 Cont. (b) Viscous analysis summary and boundary-layer development for the Eppler E387 airfoil, $\alpha = 7.4°$.

Pressure Tunnel [McGhee et al., 1988]. Figs. 6-7 to 6-10 show comparisons between measurements and calculations at $R = 300,000$. Fig. 6-7 shows the aerodynamic characteristics. While the original program underpredicts the drag by 10 or 20 counts, the new version is quite accurate. Also shown is the prediction with Drela's XFOIL program. Even though XFOIL was run with $n = 12$, the drag is still underpredicted. As the bubble in this case is as long, if not longer, than the experimental, the small drag values can only be a consequence of a too small value for the dissipation coefficient in the turbulent part of the bubble.

Fig. 6-8(a) shows the pressure distribution for the lowest point on the polar. The slight drag overprediction at low c_ℓ in Fig. 6-7 is caused by the too steep bubble recovery that can be seen on the upper surface. Fig. 6-8(b) shows the boundary-layer development. Fig. 6-9 shows the results at $\alpha = 1.5^0$. Fig. 6-10(a) shows a leading-edge bubble at a high c_ℓ. It is quite similar in shape to the slight perturbation in the experimental pressure distribution, including the small undershoot. Better agreement might be obtained with slightly different profiles, for instance the Green profiles. In fact, the early transition is a consequence of the very high values for the shape factor, shown in Fig. 6-10(b), which seem unrealistic.

Fig. 6-11 shows the drag polar at $R = 200,000$. Again, the prediction is excellent. Figs. 6-12–6-14 are some characteristic analyses. Fig. 6-15 is a limiting case, very near the critical Reynolds number. Below $R = 100,000$, the model breaks down due to a transition length which extends beyond the trailing edge. At this Reynolds number the prediction is not as good, as shown in Figs. 6-16 to 6-20. The pressure distribution shown in Fig. 6-16(a) highlights some of the limitations of the model. The error due to the envelope method increases as the Reynolds number decreases. Thus it could explain the disagreement between the measured and predicted transition predictions for the upper surface bubble. The

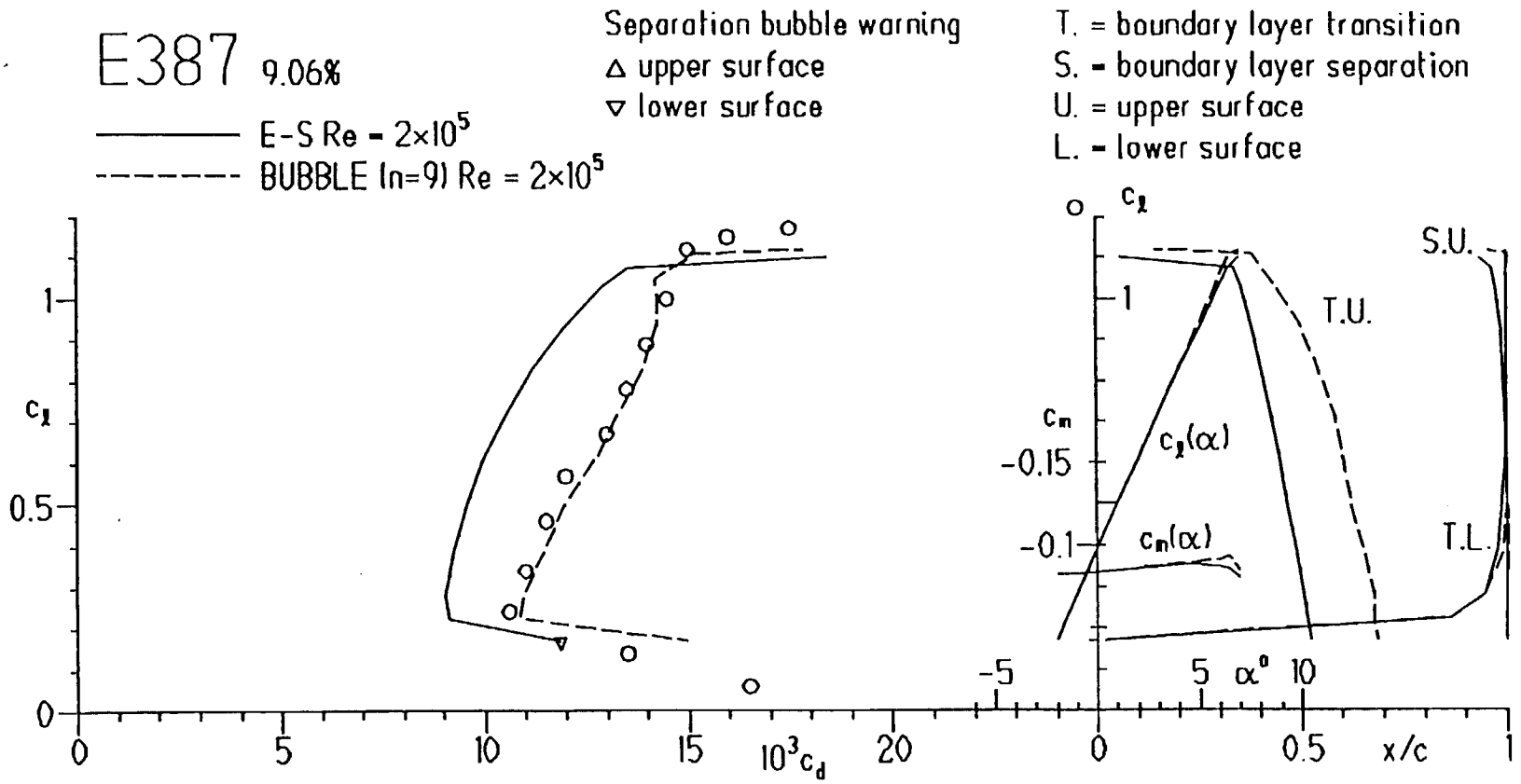

Fig. 6-11 Aerodynamic characteristics of the Eppler E387 airfoil obtained with the original Eppler and Somers program compared with those obtained with the present bubble model, $R = 200,000$. Data are from McGhee et al. [1988].

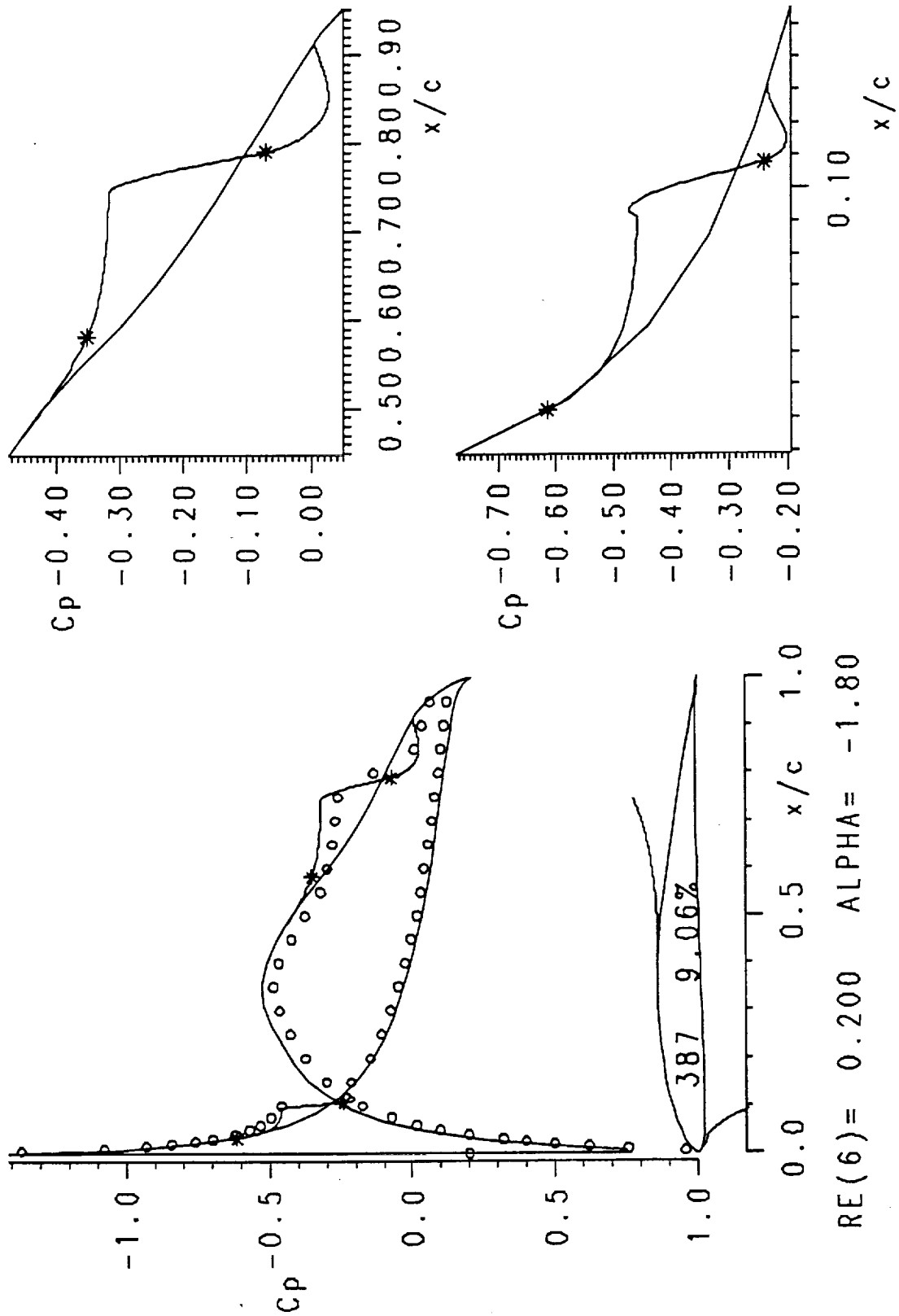

Fig. 6-12 (a) Comparison of predicted and measured pressure distribution for the Eppler E387 airfoil. Experimental $\alpha = -2°$. Data are from McGhee et al. [1988].

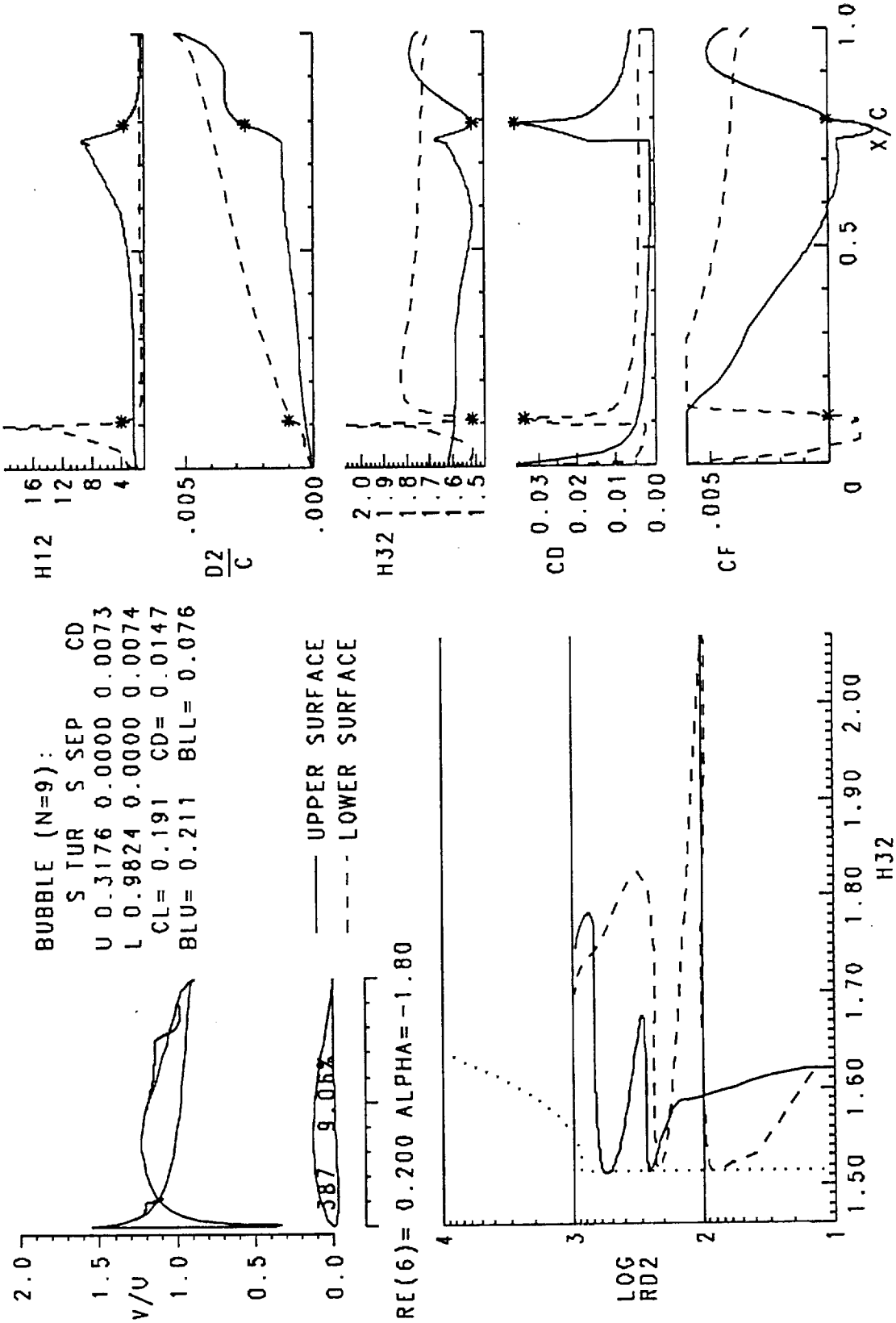

Fig. 6-12 Cont. (b) Viscous analysis summary and boundary-layer development for the Eppler E387 airfoil, $\alpha = -1.8°$.

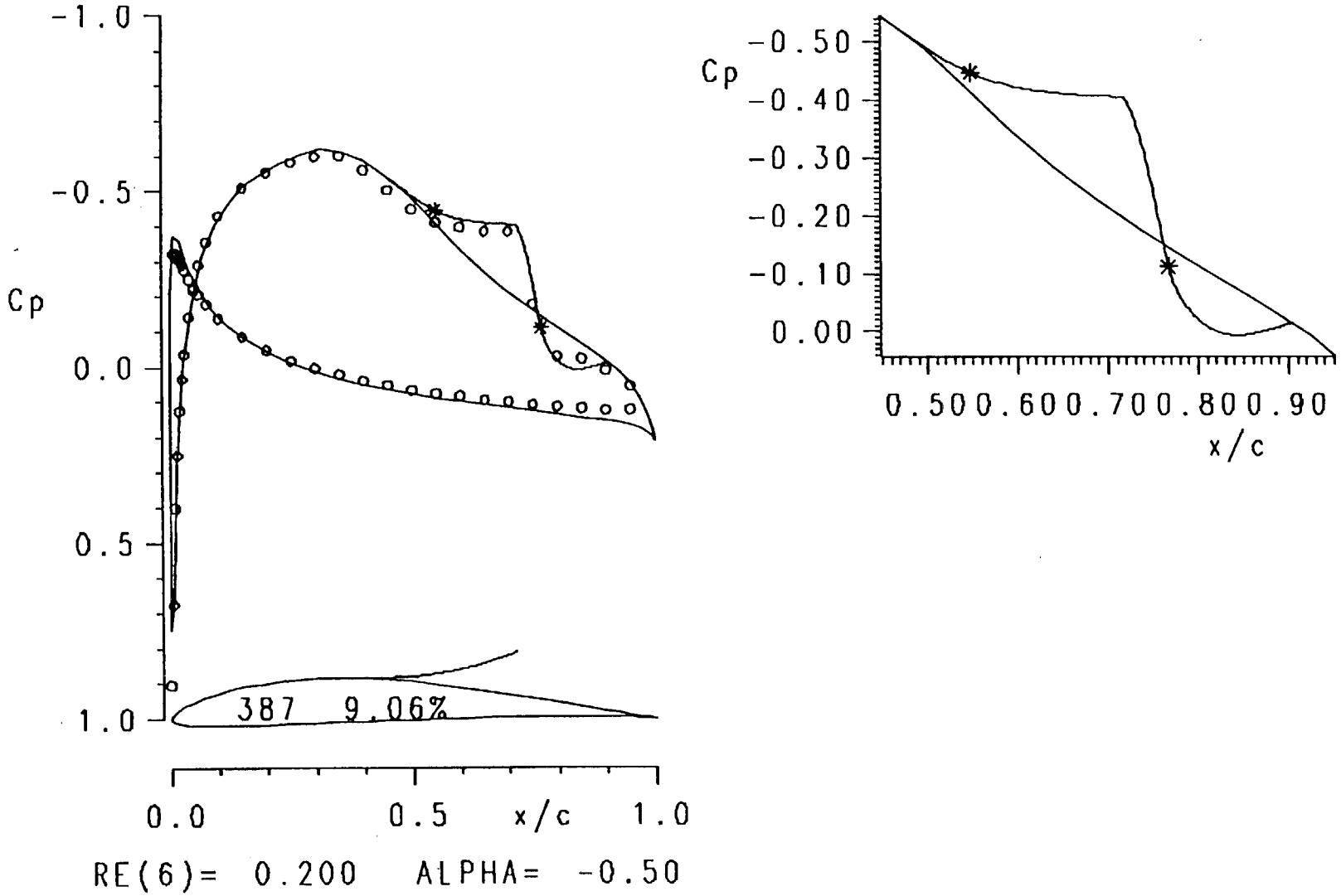

Fig. 6-13 (a) Comparison of predicted and measured pressure distribution for the Eppler E387 airfoil. Experimental $\alpha = 0°$. Data are from McGhee et al. [1988].

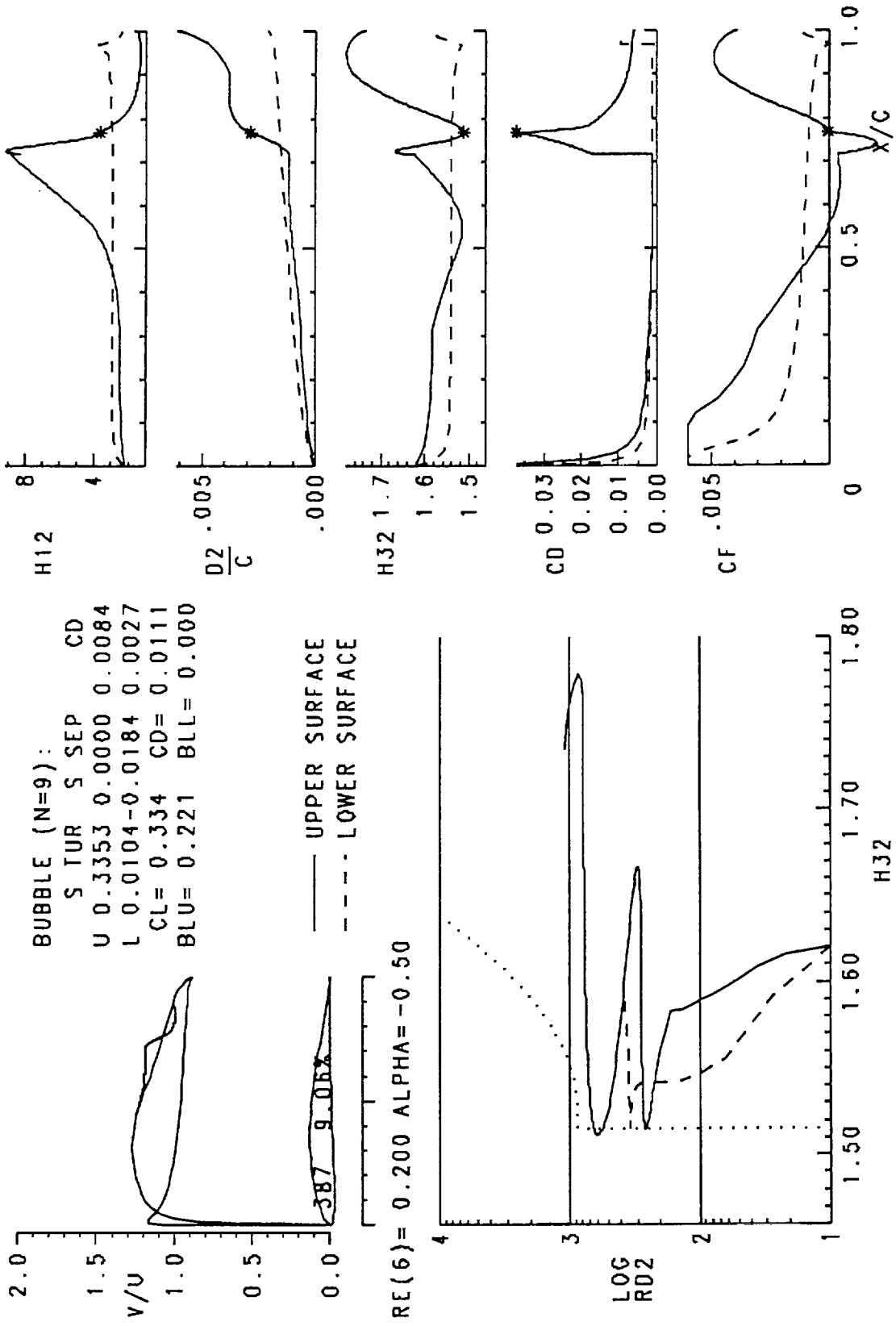

Fig. 6-13 Cont. (b) Viscous analysis summary and boundary-layer development for the Eppler E387 airfoil, $\alpha = -0.5°$.

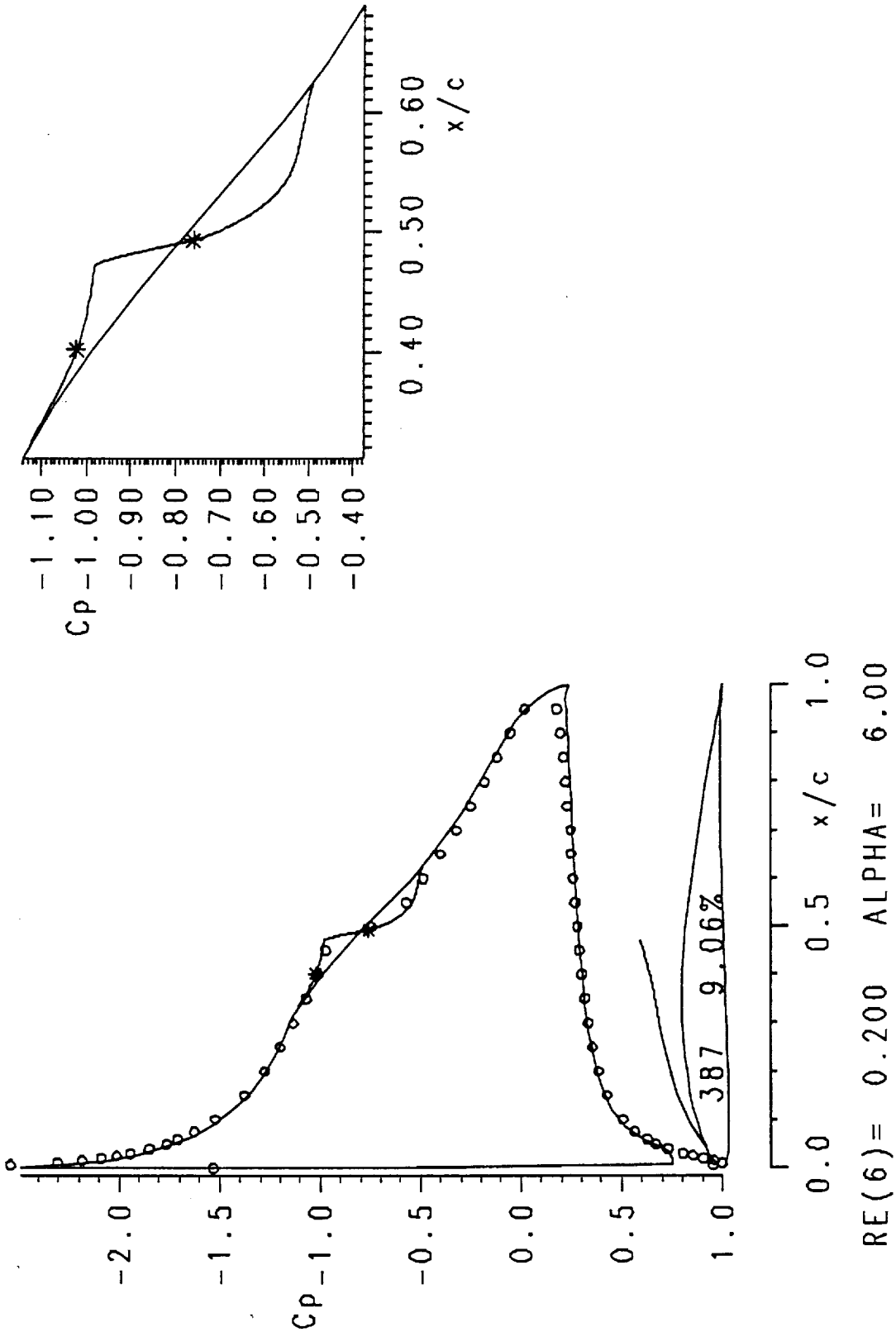

Fig. 6-14 (a) Comparison of predicted and measured pressure distribution for the Eppler E387 airfoil. Experimental $\alpha = 7°$. Data are from McGhee et al. [1988].

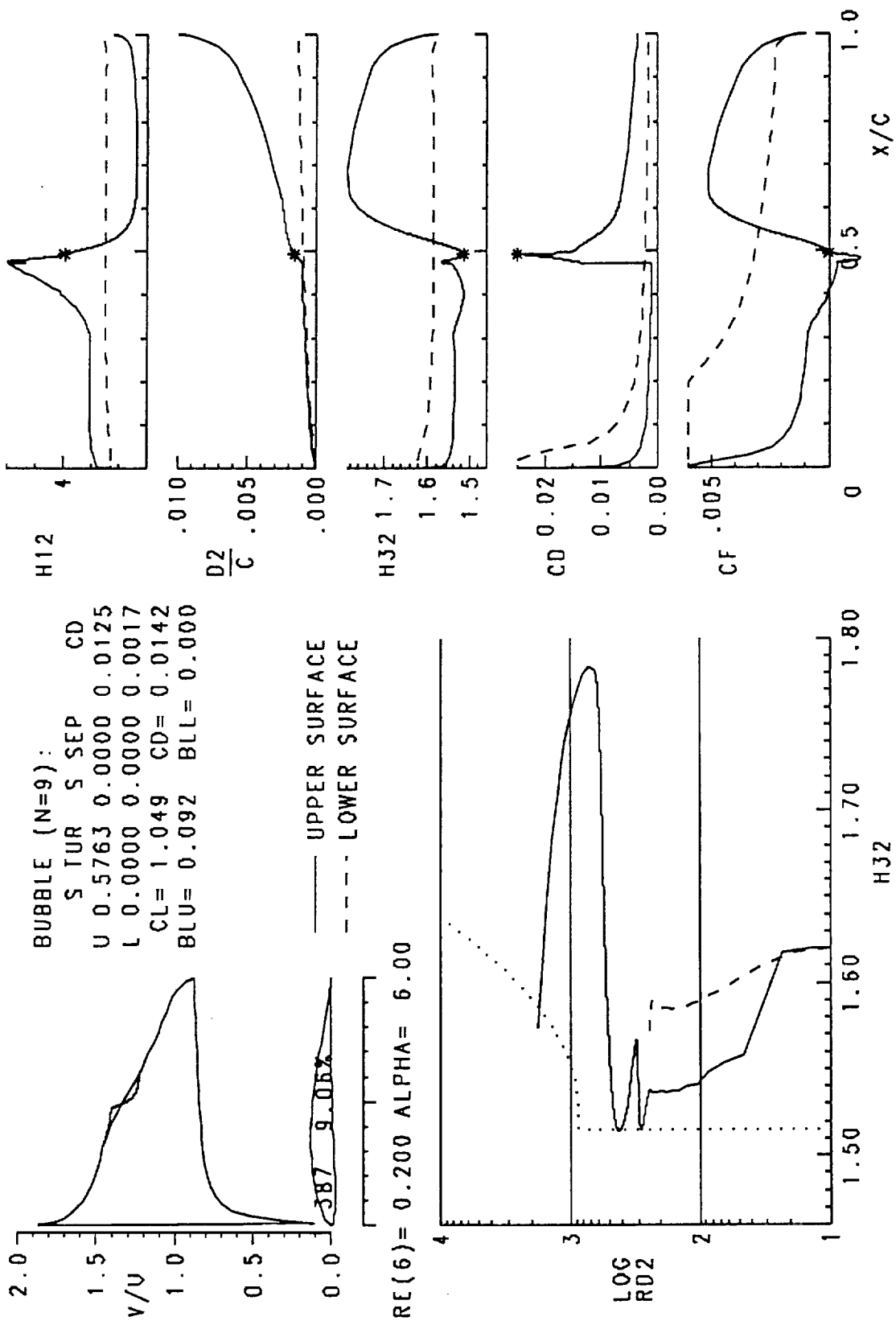

Fig. 6-14 Cont. (b) Viscous analysis summary and boundary-layer development for the Eppler E387 airfoil, $\alpha = 6°$.

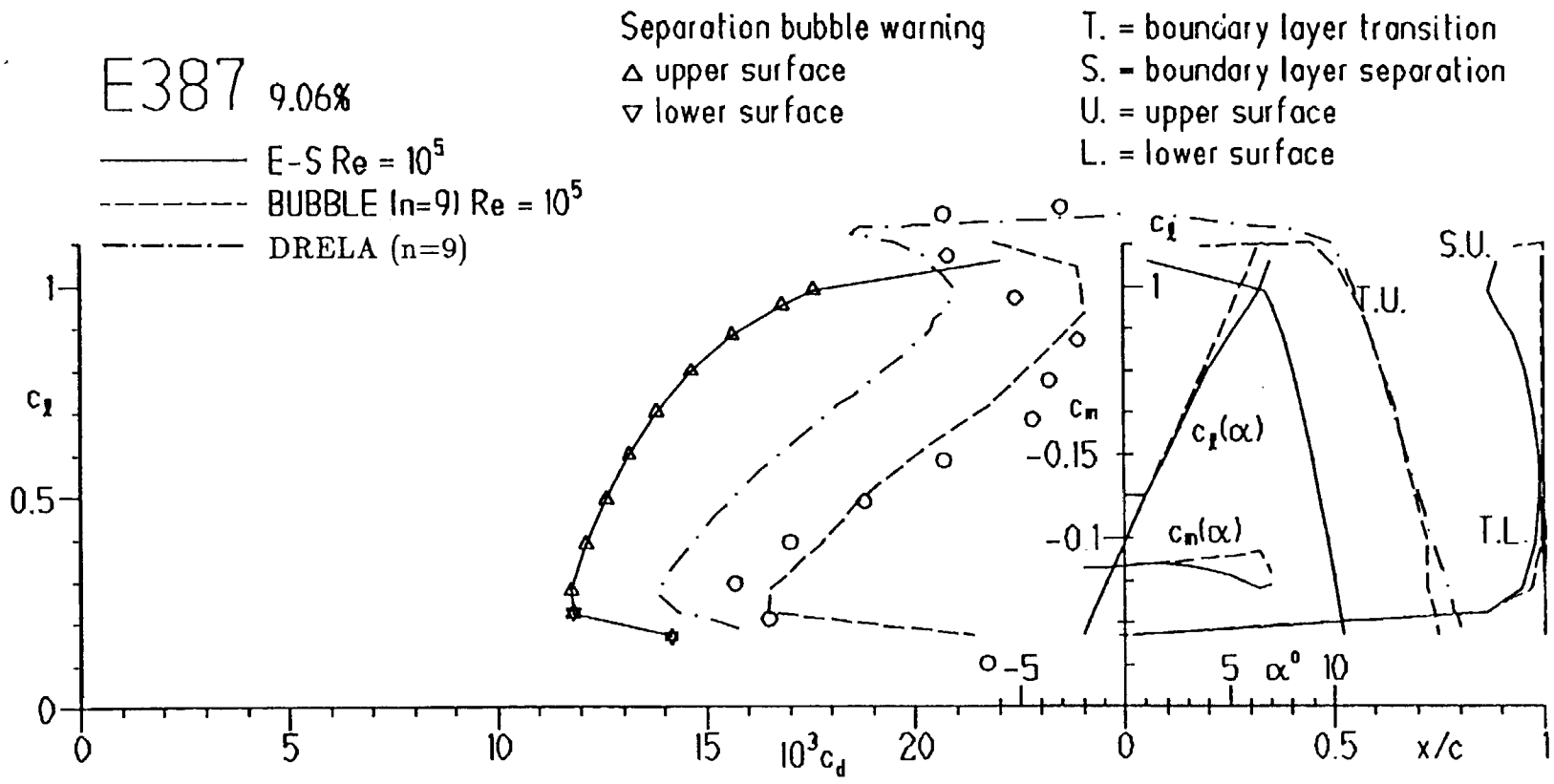

Fig. 6-15 Aerodynamic characteristics of the Eppler E387 airfoil obtained with the original Eppler and Somers program compared with those obtained with the present bubble model and with the interactive program XFOIL of Drela, $R = 100,000$. Data are from McGhee et al. [1988].

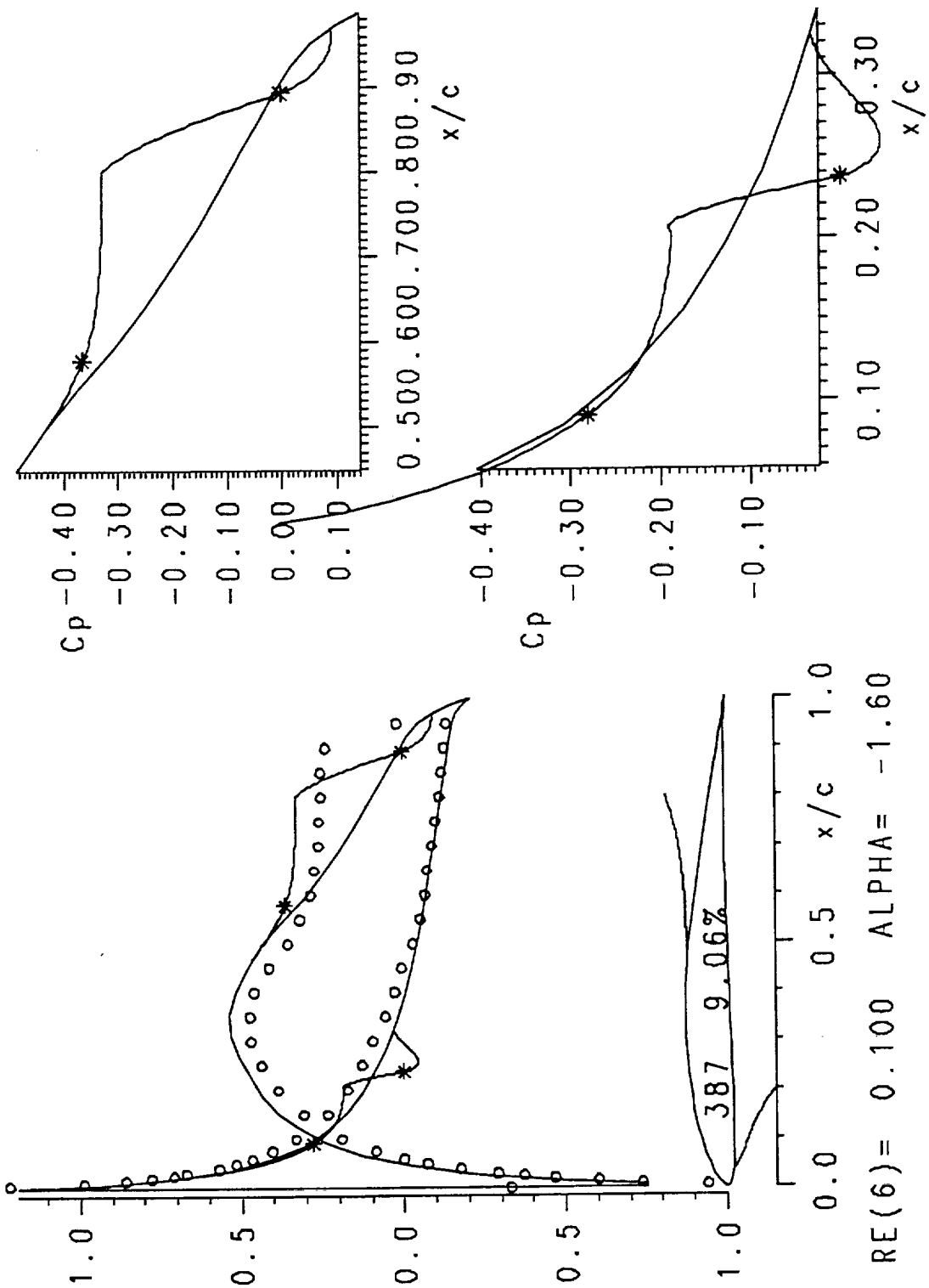

Fig. 6-16 (a) Comparison of predicted and measured pressure distribution for the Eppler E387 airfoil. Experimental $\alpha = -2°$. Data are from McGhee et al. [1988].

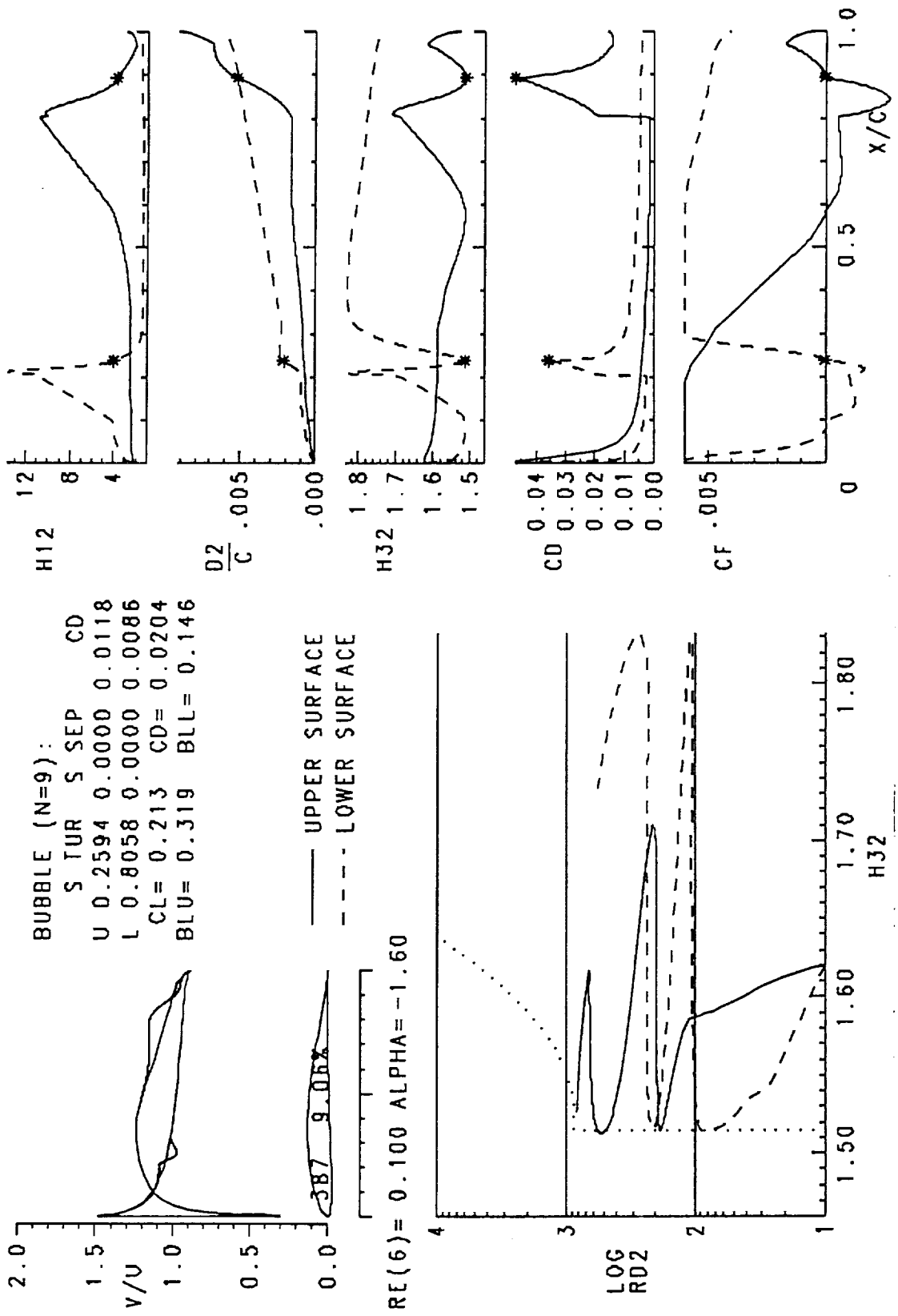

Fig. 6-16 Cont. (b) Viscous analysis summary and boundary-layer development for the Eppler E387 airfoil, $\alpha = -1.6°$.

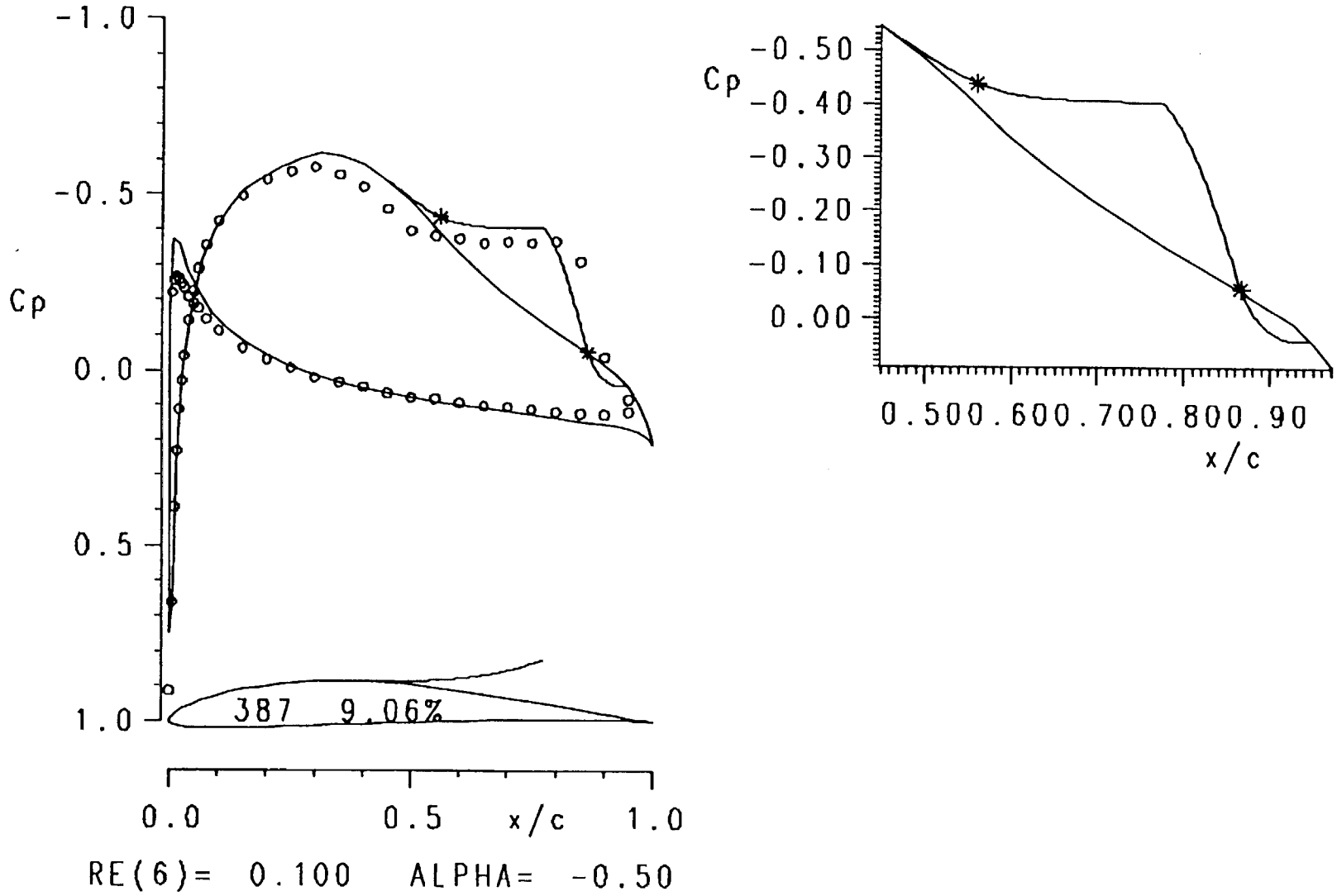

Fig. 6-17 (a) Comparison of predicted and measured pressure distribution for the Eppler E387 airfoil. Experimental $\alpha = 0°$. Data are from McGhee et al. [1988].

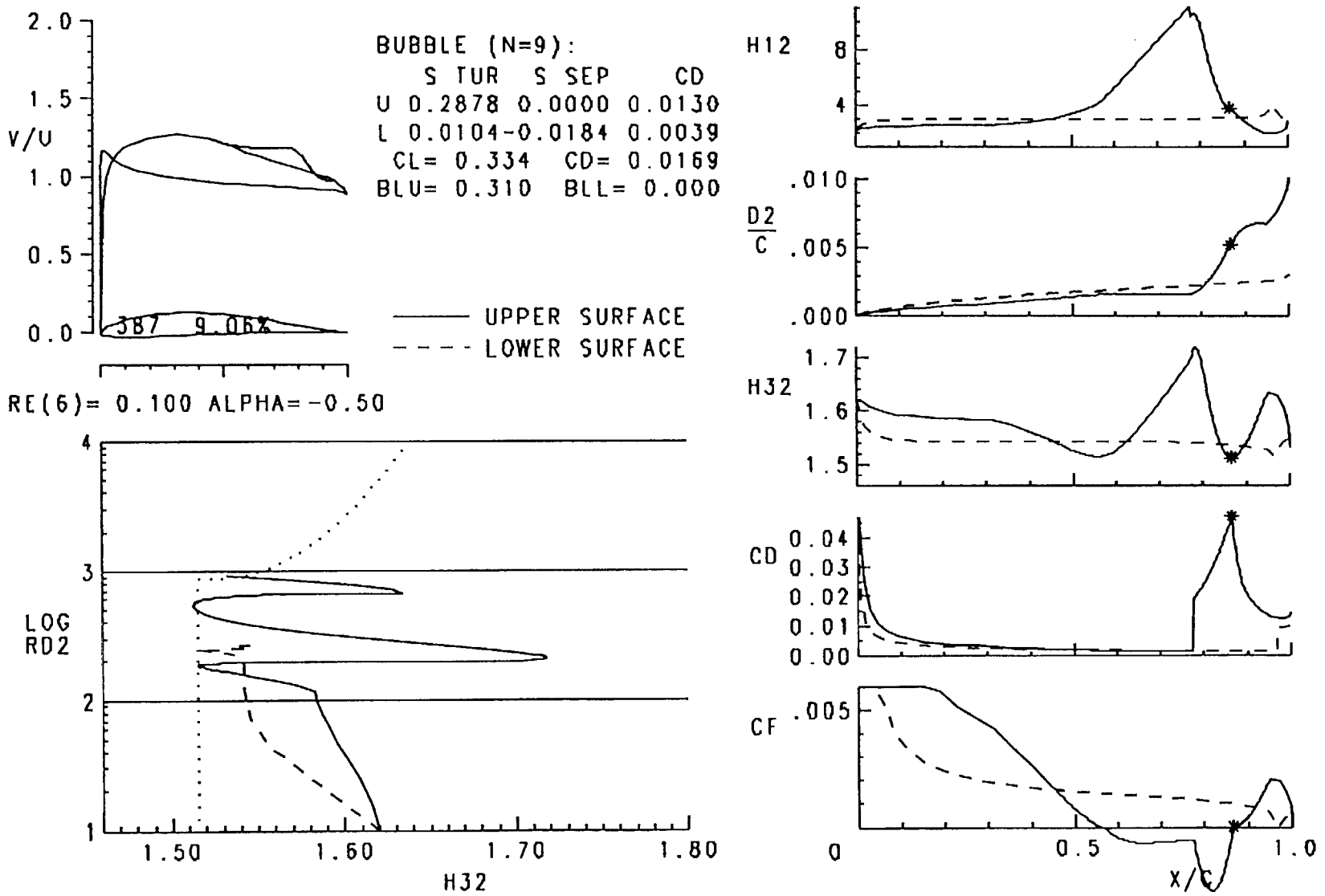

Fig. 6-17 Cont. (b) Viscous analysis summary and boundary-layer development for the Eppler E387 airfoil, $\alpha = -0.5°$.

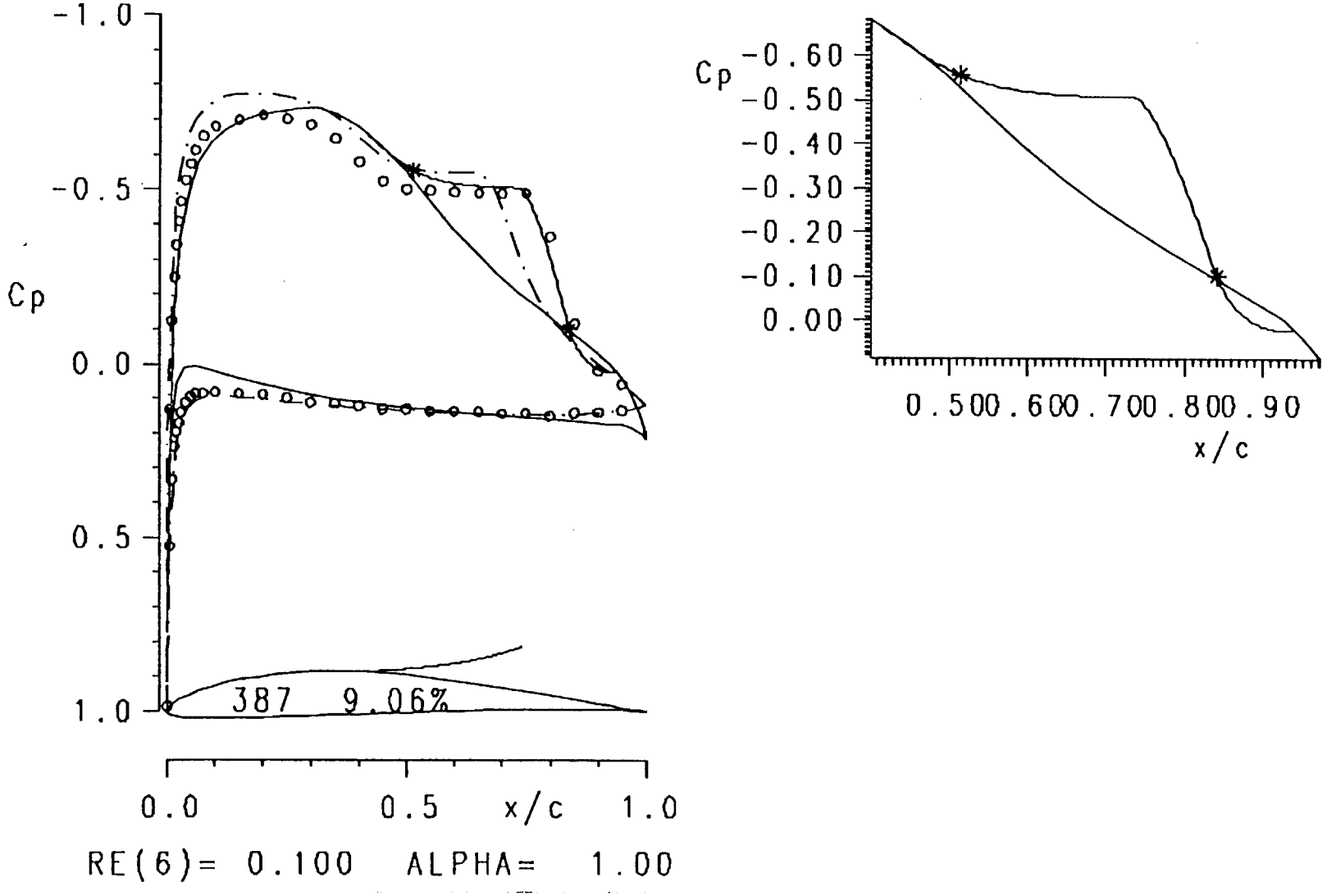

Fig. 6-18 (a) Comparison of predicted and measured pressure distribution for the Eppler E387 airfoil, $\alpha = -5°$. Dot-dashed line is XFOIL prediction at $\alpha = 2°$. Data are from McGhee et al. [1988].

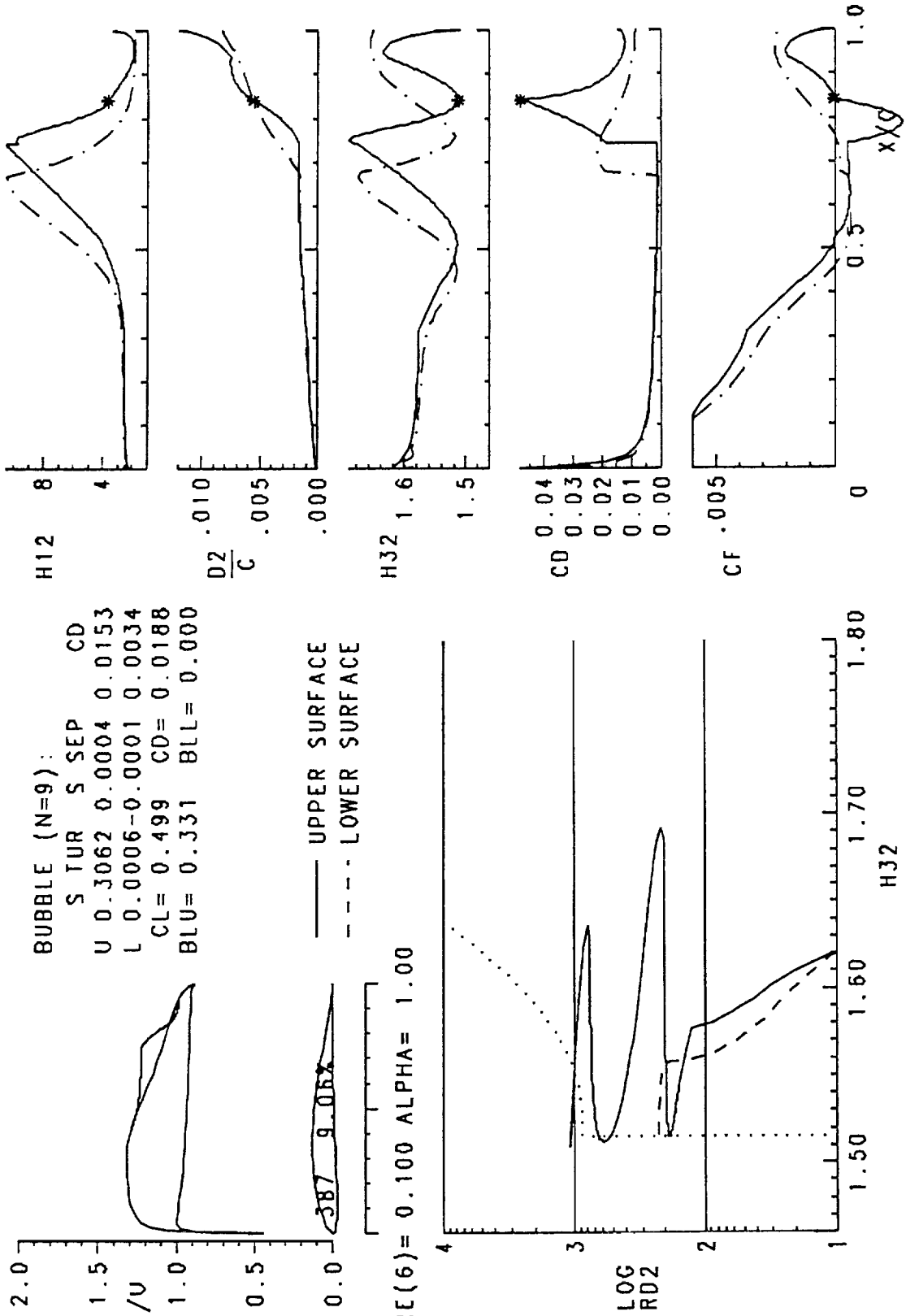

Fig. 6-18 Cont. (b) Viscous analysis summary and upper surface boundary-layer development at $\alpha = 1°$ compared with XFOIL prediction at $\alpha = 2°$ for the Eppler E387 airfoil.

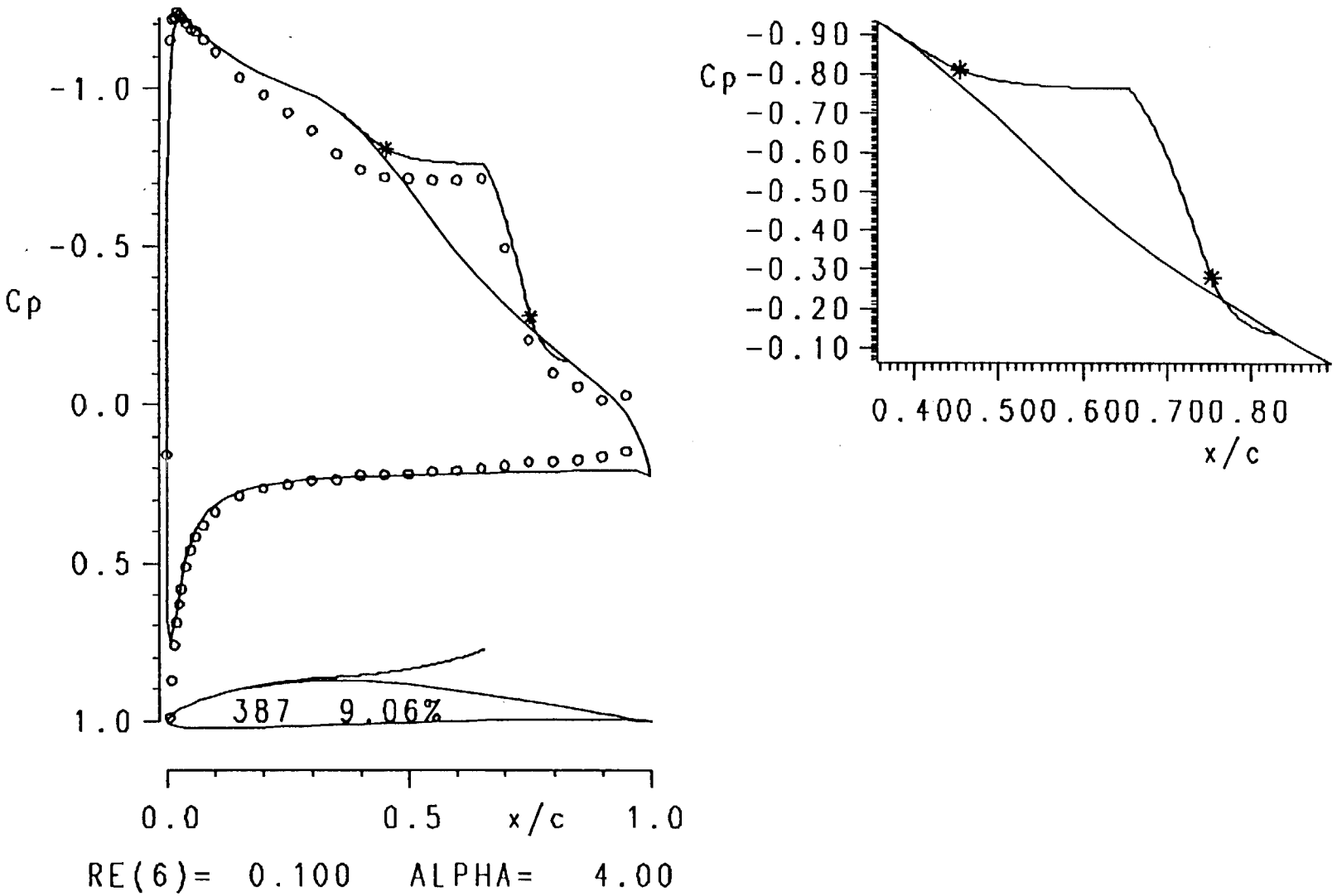

Fig. 6-19 (a) Comparison of predicted and measured pressure distribution for the Eppler E387 airfoil. Experimental $\alpha = 5°$. Data are from McGhee et al. [1988].

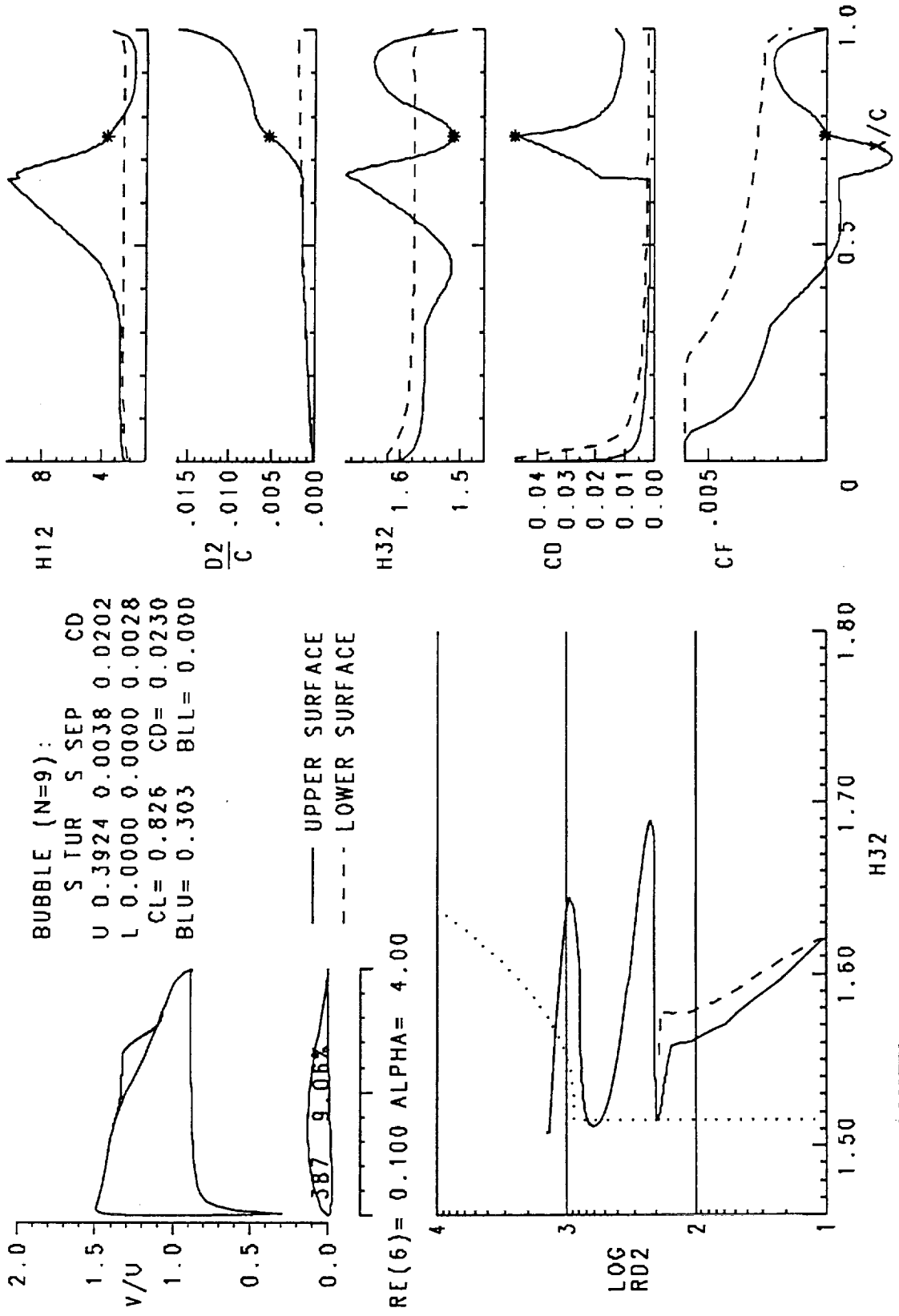

Fig. 6-19 Cont. (b) Viscous analysis summary and boundary-layer development for the Eppler E387 airfoil, $\alpha = 4°$.

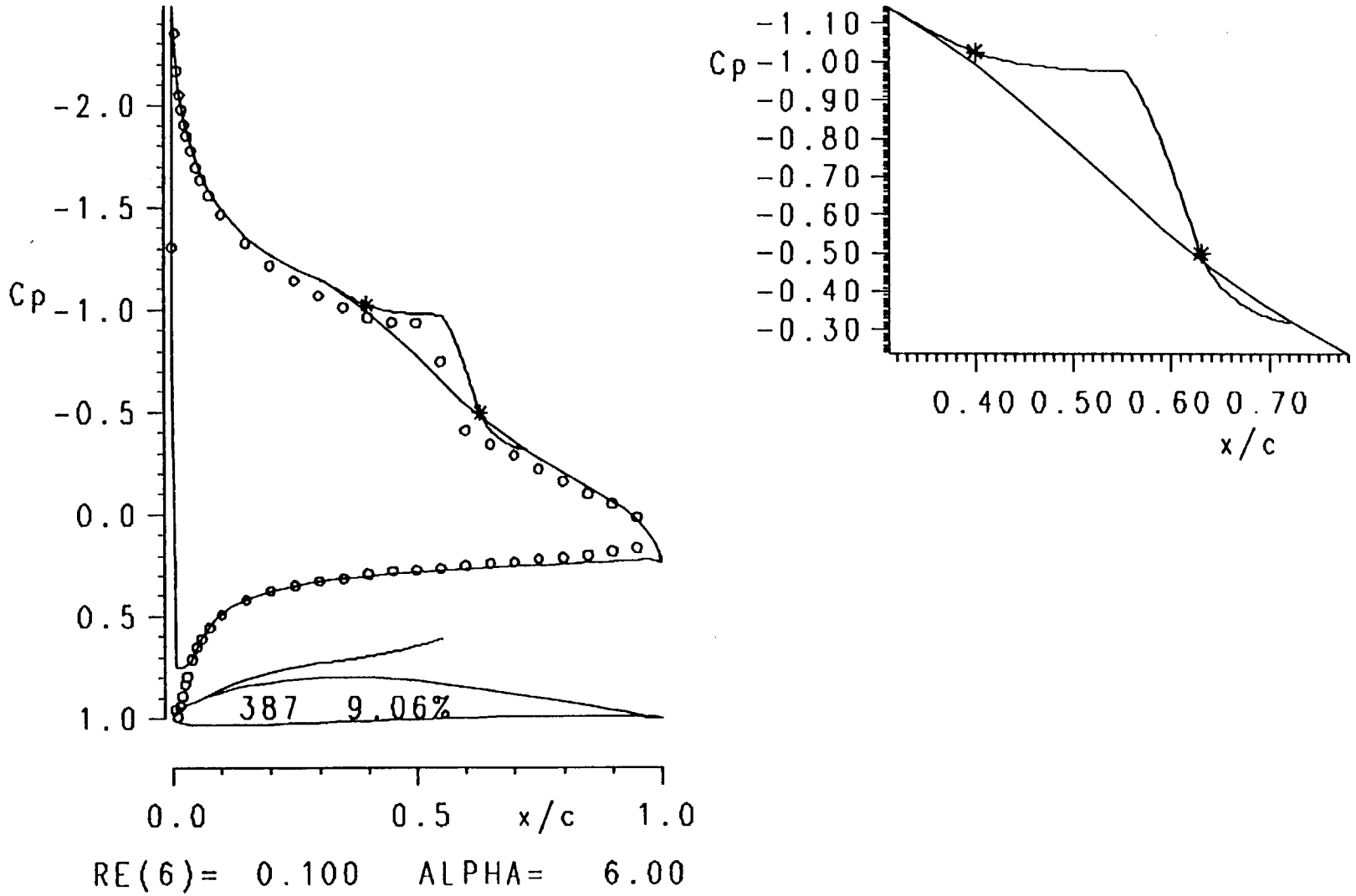

Fig. 6-20 (a) Comparison of predicted and measured pressure distribution for the Eppler E387 airfoil. Experimental $\alpha = 7°$. Data are from McGhee et al. [1988].

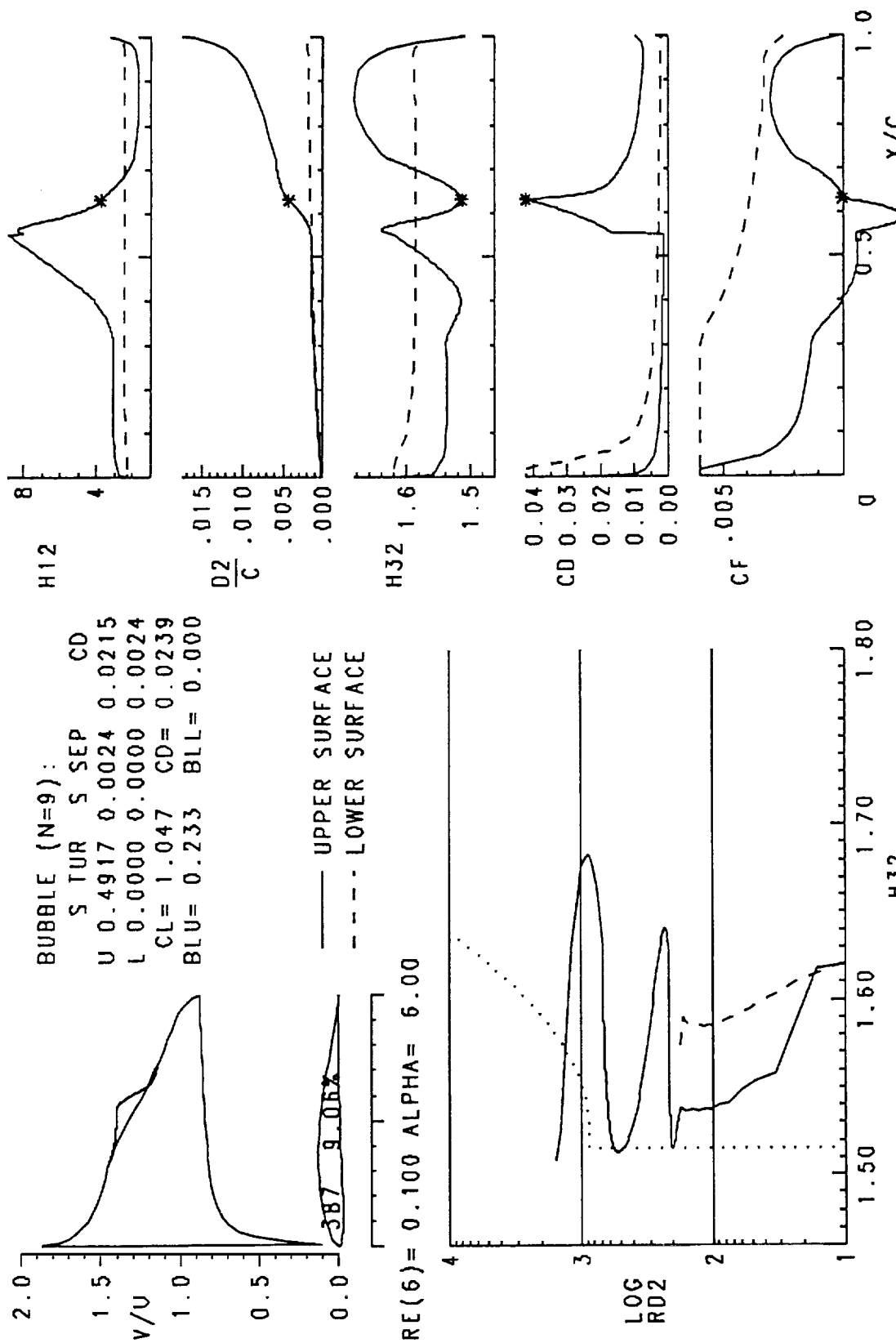

Fig. 6-20 Cont. (b) Viscous analysis summary and boundary-layer development for the Eppler E387 airfoil, $\alpha = 6°$.

lower surface bubble is of a very difficult type for the model. In fact, the velocity distribution along the bubble deviates significantly from a straight line, such that the height at the transition point is probably overestimated by Eq. (5.31). As a consequence, the predicted turbulent length is also too large leading to a too great pressure recovery. A higher-order dependence of h_T on the curvature of the velocity distribution should be developed. As discussed by Gaster, such deviation from a linear recovery may be well represented by a P^2-term in the correlations. As the pressure distribution upstream of laminar separation becomes increasingly adverse, as shown in Figs. 6-17(a)–6-20(a), the predicted transition point moves downstream relative to the experimental. This is consistent with the conclusions of Chapter 4 about Drela's e^n method. In Fig. 6-18(a), the effect of the interaction on the growth of n can be clearly seen in the XFOIL analysis. At this Reynolds number, in fact, the bubble is so large that its effect on the pressure distribution upstream of laminar separation cannot be neglected anymore. The steeper growth of n that results is responsible for the early transition. This effect is probably independent of the e^n method employed such that a correlation between n and R should be developed for use with interactive methods. In Figs. 6-16(b)–6-20(b) the details of the boundary-layer development inside the bubble are most clearly evident. To conclude the comparisons, the last two airfoils to be discussed, Figs. 6-21 and 6-22, were tested for pressure distributions and boundary-layer developments using Laser-Doppler Velocimeters.

NACA 65-213 Airfoil

An NACA 65-213 airfoil was tested by Hoheisel et al. [1984] at DLR, Germany. Pressure coefficients and boundary-layer developments obtained with a Laser-Doppler Velocimeter are given for the upper surface at zero angle of attack and $R = 240,000$. Fig. 6-21(a) shows the airfoil and the pressure distribution. Al-

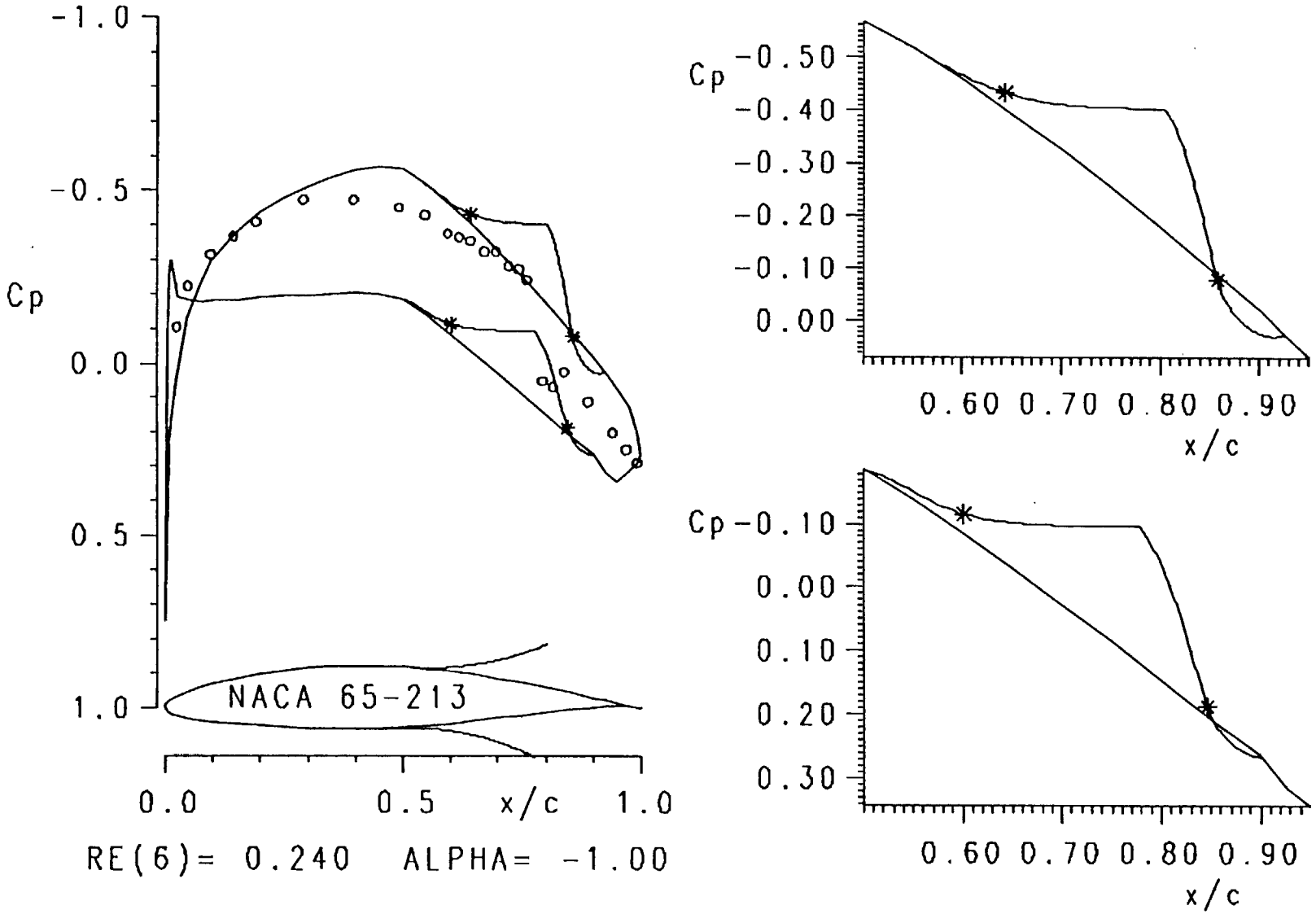

Fig. 6-21 (a) Comparison of predicted and measured pressure distribution for the NACA 65-213 airfoil. Experimental $\alpha = 0°$. Data are from Hoheisel et al. [1984].

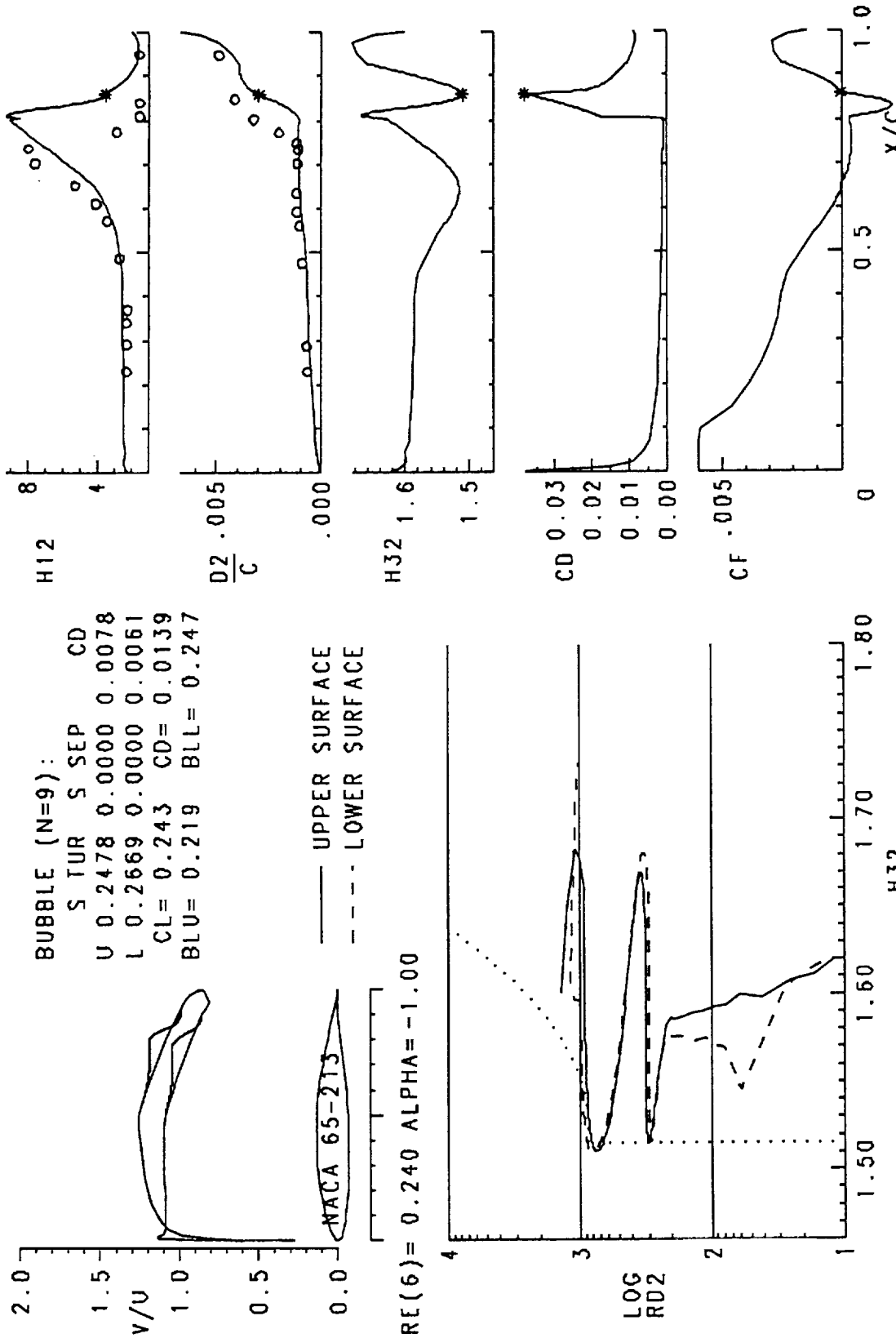

Fig. 6-21 Cont. (b) Viscous analysis summary and upper surface boundary-layer development for the NACA 65-213 airfoil, $\alpha = -1°$ compared to the Laser Doppler Velocimeter measurements of Hoheisel et al. [1984], $\alpha = 0°$.

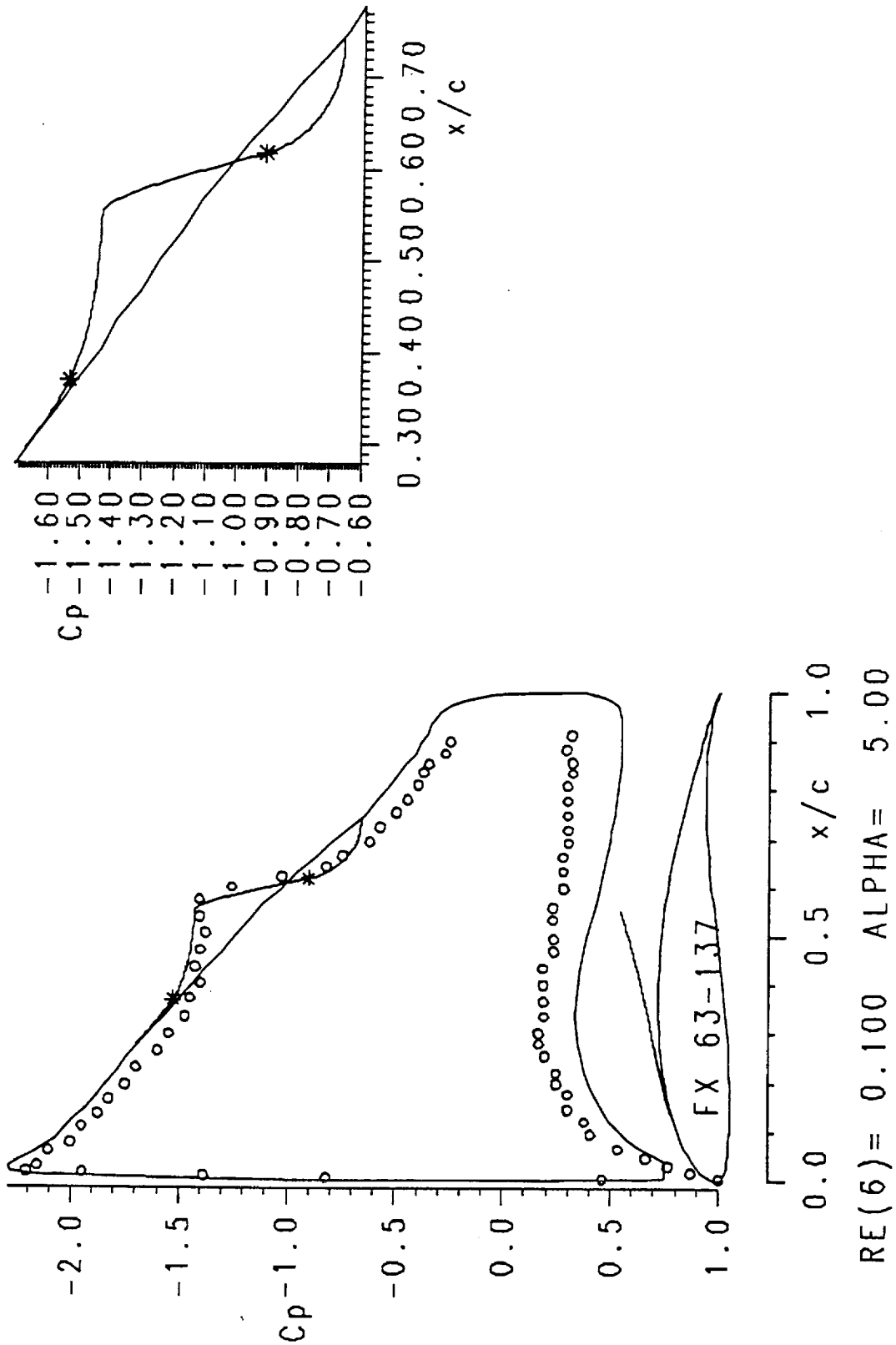

Fig. 6-22 (a) Comparison of predicted and measured pressure distribution for the Wortmann FX 63-137 airfoil. Experimental $\alpha = 7°$. Data are from Brendel and Mueller [1986].

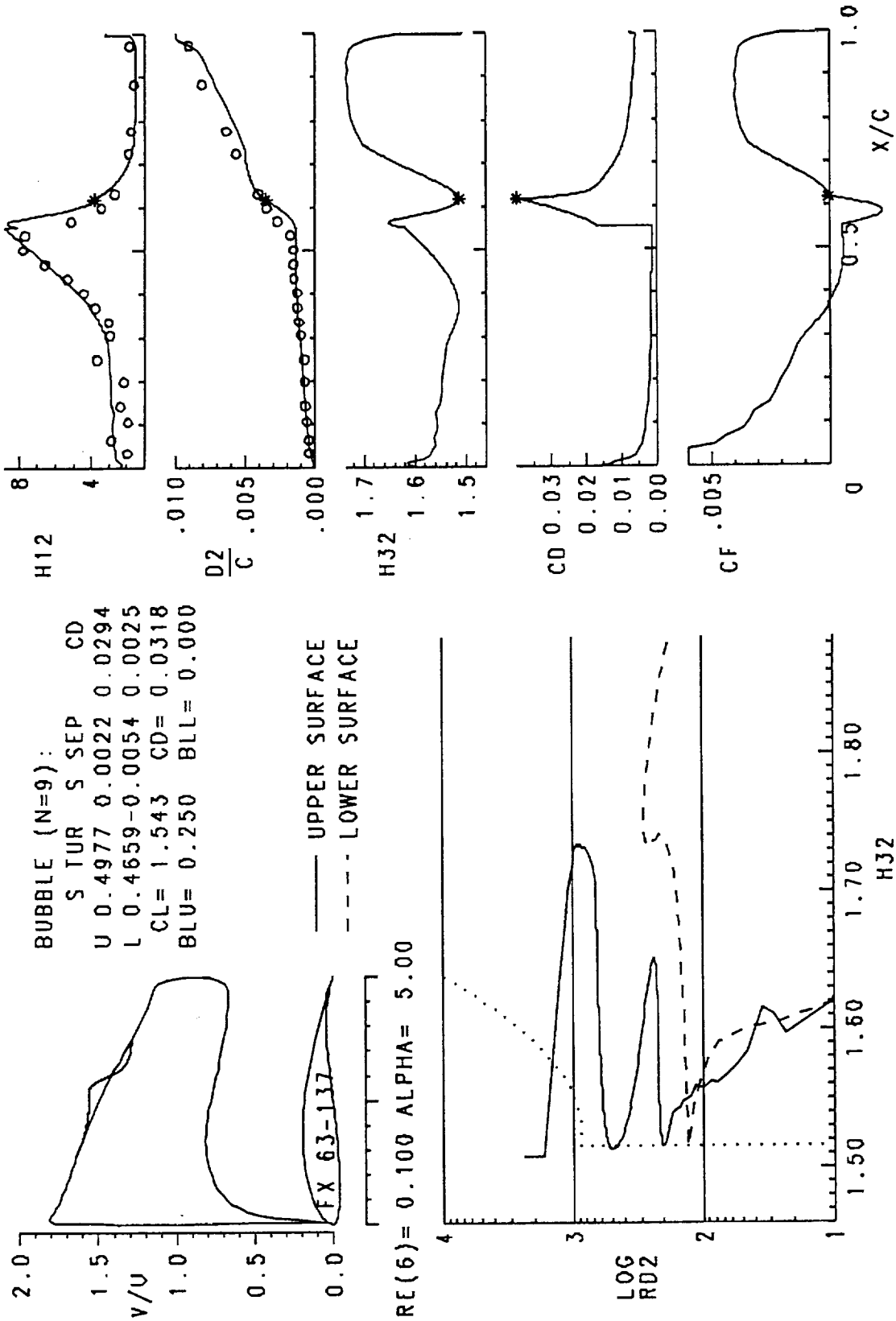

Fig. 6-22 Cont. (b) Viscous analysis summary and upper surface boundary-layer development for the Wortmann FX 63-137 airfoil, $\alpha = 5°$ compared to the Laser Doppler Velocimeter measurements of Brendel and Mueller [1986], $\alpha = 7°$.

though the inviscid analysis is performed at one degree less than the experimental, the pressures could not be matched since the coordinates used were not the experimental ones and, morcover, were generated by scaling those of an NACA 65-210 airfoil. As explained in Abbot and Von Doenhoff [1959], this is an approximate procedure which can be used in place of the exact method of Theodorsen if the change in thickness is small. Finally, the turbulence intensity of the wind tunnel used is $Tu_\infty = 0.2\%$. This is to be contrasted with that of LTPT, which is less than 0.02%. Both the shape of the bubble distribution and the transition location appear to be affected by such a high freestream turbulence intensity. In fact, the bubble recovers a significant amount of pressure in the laminar part, followed by a fairly gradual steepening into the fully turbulent recovery. As shown in Fig. 6-21(b), the experimental transition point occurs about 5%c upstream of the predicted. In any case, the shape factor and momentum thickness developments are reproduced very well.

Wortmann FX 63-137 Airfoil

The last of the comparisons is a prediction of the pressure distribution and boundary-layer development over a Wortmann FX 63-137 airfoil at $R = 100,000$. The data were taken by Brendel and Mueller [1988] with an LDV at $\alpha = 7^0$. Fig. 6-22(a) shows the pressure distribution and Fig. 6-22(b) the upper surface boundary-layer development. Although the calculated trailing-edge value of momentum thickness is 0.028, the plot is cut off as shown in order to view more clearly the bubble region. The comparison is very good.

Chapter 7

CONCLUSION

Summary and Conclusions

The correct scaling parameters for the bubble have been determined: P, $(R_{\delta_2})_S$, and h_T/c. The generality of the model relies on having understood and correctly approximated the dominant physical processes in the bubble flowfield. Having identified what the bubble depends on, parameters characteristic of this particular problem have been utilized to construct an algorithm that conforms to the flow development itself. Thus, the strong interaction leading to the pressure plateau in the laminar part is well represented by $DU(P)$, a relationship that reflects the dependent role of the pressure recovery. The e^n method coupled with Wortmann's correlation for the separation angle as a function of P and $(R_{\delta_2})_S$ allows the transition location and the height of the bubble at transition to be found. h_T/c, in turn, determines the length of the turbulent part such that even a rough estimate of the turbulence intensity in the reattachment region allows an accurate prediction of the pressure distribution and the momentum thickness growth.

The feasibility of a semi-empirical approach has finally been established. After fifty years of unsuccessful attempts at developing a general semi-empirical bubble model, the identification of the correct scaling parameters for the bubble has finally made such an approach possible. This has brought two main advantages: a method more efficient than any interactive boundary-layer of finite-difference algorithm and a deeper understanding of the bubble flowfield without which, in fact, the method could not have been developed.

A general, accurate, and computationally efficient laminar separation bubble

model has been developed. Although very simple, the model is able to reproduce the effects of vastly different bubbles over the whole Reynolds number range in which bubbles form. On a VAXstation 3100, the original version of the Eppler and Somers program takes approximately ten seconds to generate a drag polar, which typically is defined by fourteen angles of attack. The program with the bubble model takes approximately one minute for the same analysis. Drela's XFOIL takes approximately thirty minutes, partly because smaller steps in angle of attack must be taken to ensure convergence.

Suggestions for Future Work

The simplicity of the model brings a few drawbacks. While its response to large changes in the controlling flow conditions is correct to lowest order, its sensitivity to slight variations in pressure distribution is limited. More importantly, its performance near limiting conditions such as high angles of attack, very low Reynolds numbers, or very unusual pressure distributions is not reliable. These deficiencies can be traced to the "stiffness" of the model: by effectively integrating parts of the flowfield in an approximate way, the pointwise flexibility of the original governing equations is lost. Whereas it appears that the bubble flowfield itself has been properly "integrated," its effect on the airfoil pressure distribution has not. An interactive method should therefore be incorporated in the Eppler and Somers program in order to be able to analyze those limiting cases where the present model is likely to fail.

The principles of conservation of mechanical energy and momentum that are invoked to justify the pressure plateau in the laminar part might be used to deduce what the value of G should be in the Green profiles. Since the value of skin friction appears to have such a small impact on the bubble development, the correlations based on these profiles may lead to a more accurate calculation of the separated

laminar shear layer.

Another concern for future work on the improvement of the model is the transition prediction method. The method of Stock and Degenhart should be implemented in place of Drela's but its accuracy should nonetheless be tested against "exact" stability analyses of boundary-layer developments calculated by finite-difference methods. The influence of the interaction on the growth of n deserves particular attention. It appears from the XFOIL analyses that the correct transition location can be matched by a value of n that increases with decreasing Reynolds number. It should therefore be possible to develop an empirical function $n(R)$ that reflects this trend.

Finally, very detailed measurements of the reattachment process are necessary to understand it better and to provide a better estimate for C_D in the turbulent part of the bubble. Specifically, the mean flow and the turbulent stresses should be measured in order to deduce the actual distribution of dissipation coefficient in the turbulent part of the bubble.

APPENDIX

MODEL SUMMARY

In this appendix, all the equations used in the present version of the bubble model are summarized. This will facilitate both the understanding and the reproduction of the model.

Laminar Boundary-Layer

The inviscid velocity distribution is used to drive the laminar boundary-layer development, which is found by integrating the following system of equations.

Governing Equations:

$$\frac{d\delta_2}{ds} = \frac{c_f}{2} - (H_{12}+2)\frac{\delta_2}{U}\frac{dU}{ds} \tag{A.1}$$

$$\frac{d\delta_3}{ds} = C_D - 3\frac{\delta_3}{U}\frac{dU}{ds} \tag{A.2}$$

Closure correlations:

$$H_{12} = \begin{cases} (25.71578574H_{32} - 89.58214201)H_{32} \\ +79.87084472, & H_{32} \geq 1.7258 \\ \sqrt{H_{32} - 1.515095}[(-227.18220H_{32} \\ +724.55916)H_{32} - 583.60182], & H_{32} < 1.7258 \end{cases} \tag{A.3}$$

$$R_{\delta_2}\frac{c_f}{2} = \begin{cases} (2.2216872229H_{32} - 4.226252829)H_{32} \\ +1.3723907030, & H_{32} \geq 1.7258 \\ [(-0.03172850655H_{12} + 0.3915405523)H_{12} \\ -1.686094798]H_{12} + 2.512588652, & H_{32} < 1.7258 \end{cases} \tag{A.4}$$

$$R_{\delta_2}C_D = (6.8377961H_{32} - 20.521103)H_{32} + 15.707952 \tag{A.5}$$

Laminar Separation:

$$H_{32} = 1.515095 \tag{A.6}$$

Laminar Part of the Bubble

The development of the shear layer in the laminar part of the bubble is calculated by integrating Eqs. (A.1) and (A.2) along with the following expressions. The removal of the Goldstein singularity at laminar separation is discussed at the end of Chapter 3.

Separation angle:

$$\tan\gamma = -\frac{64P}{(R_{\delta_2})_S} \tag{A.7}$$

where

$$(R_{\delta_2})_S = R\frac{U_S}{U_\infty}\frac{(\delta_2)_S}{c} \tag{A.8}$$

$$P = R\left[\frac{(\delta_2)_S}{c}\right]^2 \frac{\Delta(U/U_\infty)}{\Delta(s/c)} \tag{A.9}$$

Laminar pressure recovery:

$$\frac{U}{U_S} = 1 - DU\left\{1 - \exp\left[\frac{1}{DU}\frac{U'_S}{U_S}(s - s_S)\right]\right\} \tag{A.10}$$

where

$$DU = \begin{cases} 0.0610 + 0.3048P + 0.5072P^2 & -P < .3 \\ 0.0152 & -P > .3 \end{cases} \tag{A.11}$$

Closure correlations:

$$H_{12} = \frac{H_{32} - 1.194068}{0.08} + \left[\left(\frac{H_{32} - 1.194068}{.04}\right)^2 - 64.4\right]^{\frac{1}{2}} \tag{A.12}$$

$$R_{\delta_2}\frac{c_f}{2} = \begin{cases} -0.067 + 0.01977\frac{(7.4 - H_{12})^2}{H_{12} - 1}, & H_{12} < 7.4 \\ -0.067 + 0.022\left[1 - \frac{1.4}{H_{12} - 6}\right]^2, & H_{12} \geq 7.4 \end{cases} \tag{A.13}$$

$$R_{\delta_2}\frac{C_D}{H_{32}} = 0.207 - 0.003(H_{12} - 4)^2 \tag{A.14}$$

Transition

Amplification factor:

$$n(s) = \int_{s_0}^{s} \left[\frac{dn}{dR_{\delta_2}}(H_{12})\right]^e \frac{m(H_{12})+1}{2} \frac{\ell(H_{12})}{\delta_2(s)} ds \tag{A.15}$$

where

$$\left[\frac{dn}{dR_{\delta_2}}(H_{12})\right]^e = 0.01[\{2.4H_{12} - 3.7 + 2.5\tanh[1.5(H_{12} - 3.1)]\}^2 + 0.25]^{\frac{1}{2}} \tag{A.16}$$

$$\ell(H_{12}) = \frac{6.54H_{12} - 14.07}{H_{12}^2} \tag{A.17}$$

$$m(H_{12}) = \frac{0.058(H_{12} - 4)^2}{(H_{12} - 1) - 0.068} \frac{1}{\ell} \tag{A.18}$$

s_0 is defined as the location where $R_{\delta_2} = R_{\delta_{2_0}}$, where

$$\log_{10}[R_{\delta_{2_0}}(H_{12})] = \left[\frac{1.415}{H_{12} - 1} - 0.489\right] \tanh\left[\frac{20}{H_{12} - 1} - 12.9\right] + \frac{3.295}{H_{12} - 1} + 0.440 \tag{A.19}$$

Laminar length of the bubble:

$$\ell_1 @ n = 9 \tag{A.20}$$

Bubble height at transition:

$$h_T = \frac{\ell_1}{\tan\gamma} \tag{A.21}$$

Turbulent Part of the Bubble

Spreading angle of turbulent shear layer:

$$\tan\theta = .0975 + 2.5 \times 10^{-8} R \tag{A.22}$$

Turbulent length of the bubble:

$$\ell_2 = \frac{h_T}{\tan\theta} \tag{A.23}$$

Shape factor distribution:

$$\overline{H}_{32}(\overline{y}) = \sin\left[\frac{\pi}{\overline{y}}\right] \tag{A.24}$$

where

$$\overline{H}_{32} = \frac{H_{32} - (H_{32})_R}{+A_i\left[(H_{32})_T - (H_{32})_R\right]} - 1 \tag{A.25}$$

$$\overline{y} = \left(\frac{2}{3} - \overline{y}_0\right)\sigma + \overline{y}_0 \tag{A.26}$$

$$\overline{y}_0 = \frac{\pi}{3\pi - \sin^{-1}(1/A_1 - 1)} \tag{A.27}$$

$$\sigma = \begin{cases} (s - s_T)/\ell_2 & s \le s_R \\ [(s - s_T)/\ell_2 - 1]SF + 1 & s > s_R \end{cases} \tag{A.28}$$

$$SF = \sqrt{A_1/A_2} \tag{A.29}$$

$$A_1 = 0.5 + e^{-300(h_T/c)} \tag{A.30}$$

and A_2 is iterated upon until the undershoot merges with the inviscid velocity distribution.

The above shape factor distribution is used to drive the integral boundary-layer equations in the inverse mode.

Governing equations:

$$\frac{dU}{ds} = \left[(c_f/2)H_{32} - C_D + \delta_2\frac{dH_{32}}{ds}\right]\frac{U}{\delta_2 H_{32}(H_{12} - 1)} \tag{A.31}$$

$$\frac{d\delta_2}{ds} = \left[-\frac{3(c_f/2)H_{32}}{H_{12} + 2} + C_D - \delta_2\frac{dH_{32}}{ds}\right]\frac{H_{12} + 2}{H_{32}(H_{12} - 1)} \tag{A.32}$$

$$\frac{\delta}{C_T}\frac{dC_T}{ds} = 4.2(C_{T_{eq}}^{\frac{1}{2}} - C_T^{\frac{1}{2}}) \tag{A.33}$$

where

$$C_{\tau_{eq}} = \frac{0.015 H_{32}}{1 - U_{slip}} \left[\frac{H_{12} - 1}{H_{12}} \right]^3 \tag{A.34}$$

$$\delta = \delta_2 \left(3.15 + \frac{1.72}{H_{12} - 1} \right) + \delta_1 \tag{A.35}$$

Closure correlations:

$$C_D = f \times [C_D]_{Drela} \tag{A.36}$$

where

$$f = \begin{cases} 1 + (C_{D_{max}} - 1) \left(\frac{s - s_{\mathcal{T}}}{l_2} \right)^2, & 0 \leq \frac{s - s_{\mathcal{T}}}{l_2} \leq 1 \\ 1 + (C_{D_{max}} - 1) e^{-r\left(\frac{s - s_{\mathcal{T}}}{l_2} - 1 \right)}, & \frac{s - s_{\mathcal{T}}}{l_2} > 1 \end{cases} \tag{A.37}$$

$$r = 15 - 1000 \frac{h_{\mathcal{T}}}{c} \tag{A.38}$$

$$C_{D_{max}} = 1. + \sqrt{200 \frac{h_{\mathcal{T}}}{c}} \tag{A.39}$$

$$[C_D]_{Drela} = c_f U_{slip} + 2 C_\tau (1 - U_{slip}) \tag{A.40}$$

$$U_{slip} = \frac{H_{32}}{6} \left[\frac{4}{H_{12}} - 1 \right] \tag{A.41}$$

$$H_{12} = \begin{cases} \frac{H_{12_0}}{1 + \left[\frac{H_{32} - H_{32_0}}{c_1} \right]^{\frac{1}{1.27}}}, & c_f > 0 \\ H_{12_0} + \left[\frac{H_{32} - H_{32_0}}{c_2} \right]^{\frac{1}{c_3}}, & c_f < 0 \end{cases} \tag{A.42}$$

where

$$H_{32_0} = 1.505 + \frac{4}{R_{\delta_2}} \tag{A.43}$$

$$H_{12_0} = 3 + \frac{400}{R_{\delta_2}} \tag{A.44}$$

$$c_1 = 0.081 (R_{\delta_2} - 300)^{0.1} \tag{A.45}$$

$$c_2 = 0.0158 (R_{\delta_2} - 300)^{0.08} \tag{A.46}$$

$$c_3 = 1.06 + \frac{3000}{(R_{\delta_2} + 600)^{1.5}} \tag{A.47}$$

$$c_{f_{min}} = -\sqrt{0.0002\frac{h_T}{c}} \tag{A.48}$$

The c_f distribution is obtained by fitting a parabola through c_{f_T}, $c_{f_{min}}$, and $c_f = 0$ at ℓ_2.

Turbulent Boundary Layer

The development of the turbulent boundary layer downstream of the intersection of the undershoot with the inviscid velocity distribution is calculated in the direct mode by prescribing the inviscid velocity distribution to drive Eqs. (A.1), (A.2), and (A.33). This system of equations is complemented by closure correlations (A.34), (A.35), and (A.40)-(A.47). The skin-friction coefficient is obtained from

$$c_f = \frac{0.3e^{-1.33H_{12}}}{(\log R_{\delta_2})^{1.74+0.31H_{12}}} + 0.00011\left[\tanh\left(4 - \frac{H_{12}}{0.875}\right) - 1\right] \tag{A.49}$$

Turbulent separation:

$$H_{32} = 1.505 + \frac{400}{R_{\delta_2}} \tag{A.50}$$

Drag Calculation

Squire-Young formula:

$$c_d = \frac{\delta_{2_{TE}}}{c}\left(\frac{U_{TE}}{U_\infty}\right)^{2.5+0.5H_{12_{TE}}} \tag{A.51}$$

REFERENCES

Arnal, D., "Description and Prediction of Transition in Two-Dimensional Incompressible Flow," *Special Course on Stability and Transition of Laminar Flow*, AGARD Report No. 709, March 1984.

Bell, W. A., and Cornelius, K. C., "An Experimental Investigation of a Laminar Separation Bubble on a Natural Laminar Flow Airfoil," AIAA Paper 87-0458, January 1987.

Birch, S. F., and Eggers, J. M., "A Critical Review of the Experimental Data for Developed Free Turbulent Shear Layers," NASA SP 321, 1973, pp. 943-949.

Bradshaw, P., Ferriss, D. H., and Atwell, N. P., "Calculation of Boundary-Layer Development Using the Turbulent Energy Equation," *Journal of Fluid Mechanics*, Vol. 28, part 3, 1967, pp. 593-616.

Brendel, M., and Mueller, T. J., "Boundary Layer Measurements on an Airfoil at Low Reynolds Numbers," *Journal of Aircraft*, Vol. 25, July 1988, pp. 612-617.

Briley, R. W., and McDonald, H, "Numerical prediction of incompressible separation bubbles," *Journal of Fluid Mechanics*, Vol. 69, part 4, 1975, pp. 631-656.

Cebeci, T, "Essential Ingredients of a Method for Low Reynolds-Number Airfoils," *AIAA Journal*, Vol. 27, No. 12, December 1989, pp. 1680-1688.

Cebeci, T, and Schimke, S. M., "The calculation of separation bubbles in interactive turbulent boundary layers," *Journal of Fluid Mechanics*, Vol. 131, 1983, pp. 305-317.

Clauser, F. H., "Turbulent Boundary Layers in Adverse Pressure Gradients," *Journal of Aeronautical Sciences*, Vol. 21, February 1954, pp. 91-108.

Crabtree, L. F., "Effects of Leading Edge Separation on Thin Wings in Two-Dimensional Incompressible Flow," *Journal of Aeronautical Sciences*, Vol. 24, No. 8, August 1957, pp. 597-604.

Crimi, P., and Reeves, B. L., "Analysis of Leading-Edge Separation Bubbles on Airfoils," *AIAA Journal*, Vol. 14, No. 11, November 1976, pp. 1548-1555.

Davis, R. L. and Carter, J. E., "Analysis of Airfoil Transitional Separation Bubbles," NASA CR-3791, 1984.

Drela, M., "Two-Dimensional Transonic Aerodynamic Design and Analysis Using the Euler Equations," Massachusetts Institute of Technology, Gas Turbine Laboratory Report 187, February, 1986.

Drela, M., "XFOIL: An Analysis and Design System for Low Reynolds Number Airfoils," *Low Reynolds Number Aerodynamics, Proceedings of the Conference Notre Dame, Indiana, June 5-7, 1989*, T. J. Mueller, Editor, Lecture Notes in Engineering No. 54, Springer-Verlag, pp. 1-12.

Drela, M., and Giles, M. B., "Viscous-Inviscid Analysis of Transonic and Low-Reynolds Number Airfoils," *AIAA Journal*, Vol. 25, No. 10, October 1987, pp. 1347-1355.

Eppler, R. "Practical Calculation of Laminar and Turbulent Bled-Off Boundary Layers," NASA TM-75328, 1978. (Translated from *Ingenieur Archiv*, Vol. 32, 1963, pp. 221-245.)

Eppler, R. "Recent Developments in Boundary Layer Computation," *International Conference on Aerodynamics at Low Reynolds Numbers* $10^4 < R < 10^6$, Vol. II, Royal Aeronautical Society, London, October 1986, pp. 12.1-12.18.

Eppler, R., private communication, 1989.

Eppler, R. and Somers, D. M., "A Computer Program for the Design and Analysis of Low-Speed Airfoils," NASA TM-80210, 1980.

Evangelista, R., and Vemuru, C. S., "Evaluation of an Analysis Method for Low-Speed Airfoils by Comparison with Wind Tunnel Results," AIAA Paper 89-0266, January 1989.

Fitzgerald, E. J. and Mueller, T. J., "Measurements in a Separation Bubble on an Airfoil Using Laser Velocimetry," *AIAA Journal*, Vol. 28, No. 4, April 1990, pp. 584-592.

Gaster, M., "The Structure and Behaviour of Separation Bubbles," Aeronautical Research Council R. & M. No. 3595, March 1967.

Gault, D. E., "An Experimental Investigation of Regions of Separated Laminar Flow," NACA Technical Note 3505, September 1955.

Gleyzes, C., Cousteix, J., and Bonnet, J. L., "A Calculation Method of Leading Edge Separation Bubbles," *Numerical and Physical Aspects of Aerodynamic Flows II*, Springer-Verlag, 1983.

Green, J. E., "Two-Dimensional Turbulent Reattachment as a Boundary-Layer Problem," *Separated Flows*, AGARD Conference Proceedings No. 4, Part 1, May 1966.

Green, J. E., Weeks, D. J., and Brooman, J. W. F., "Prediction of Turbulent Boundary Layers and Wakes in Compressible Flow by a Lag-Entrainment Method," Aeronautical Research Council R. & M. 3791, January 1973.

Hoheisel, H., Hoeger, M., Meyer, P., and Koerber, G., "A Comparison of Laser-Doppler Anemometry and Probe Measurements within the Boundary Layer of an Airfoil at Subsonic Flow," *Laser Anemometry in Fluid Mechanics - II, Selected Papers from the Second International Symposium on Applications of Laser Anemometry to Fluid Mechanics*, Lisbon, Portugal, July 1984, LADOAN, pp. 143-157.

Horstmann, K. H., Quast, A., and Redeker, G., "Flight and Wind-Tunnel Investigations on Boundary-Layer Transition," *Journal of Aircraft*, Vol. 27, No. 2, February 1990, pp. 146-150.

Horton, H. P., "A Semi-empirical Theory for the Growth and Bursting of Laminar Separation Bubbles," Aeronautical Research Council C. P. 1073, June 1967.

Ingen, J. L. van, "A Suggested Semi-Empirical Method for the Calculation of the Boundary Layer Transition Region," Delft University of Technology, Department of Aerospace Engineering report VTH-74, 1956.

Ingen, J. L. van, "On the Calculation of Laminar Separation Bubbles in Two-Dimensional Incompressible Flow," *Flow Separation*, AGARD Conference Proceedings No. 168, 1975.

Ingen, J. L. van, private communication, 1989.

Ingen, J. L. van, Boermans, L. M. M., and Blom, J. J. H., "Low-Speed Airfoil Section Research at Delft University of Technology," *Proceedings of the 12th Congress of the International Council of Aeronautical Sciences*, Munich, 1980.

Ingen, J. L. van and Boermans, L. M. M., "Aerodynamics at Low Reynolds Numbers: A Review of Theoretical and Experimental Research at Delft University of Technology," *International Conference on Aerodynamics at Low Reynolds Numbers* $10^4 < R < 10^6$, vol. I, Royal Aeronautical Society, London, October 1986, pp. 1.1-1.40.

Jones, B. M., "An Experimental Study of the Stalling of Wings," Aeronautical Research Council R. & M. 1588, December 1933.

Kline, S. J., Morkovin, M. V., Sovran, G., Cockrell, D. J., Coles, D. E., and Hirst, E. A., Editors, *Computation of Turbulent Boundary Layers-1968 AFOSR-IFP-Stanford Conference*, Vols. I and II, Stanford University, Stanford, CA.

Kwon, O. K., and Pletcher, R. H., "Prediction of Incompressible Separated Boundary Layers Including Viscous-Inviscid Interaction," *Journal of Fluids Engineering*, Vol. 101, December 1979, pp. 466-472.

Mack, L. M., "Transition and Laminar Instability," Jet Propulsion Laboratory Publication 77-15, Pasadena, CA, 1977.

Maughmer, M. D. and Somers, D. M., "Design and Experimental Results for a High-Altitude, Long-Endurance Airfoil," *Journal of Aircraft*, Vol. 26, No. 2, February 1989, pp. 148-153.

McGhee, R. J., Walker, B. S., and Millard, B. F., "Experimental Results for the Eppler 387 Airfoil at Low Reynolds Numbers in the Langley Low-Turbulence Pressure Tunnel," NASA TM-4062, October 1988.

Mueller, T. J., "Low Reynolds Number Vehicles," AGARDograph No. 288, Feb. 1985.

O'Meara, M. M., and Mueller, T. J., "Experimental Determination of the Laminar Separation Bubble Characteristics of an Airfoil at Low Reynolds Numbers," AIAA Paper 86-1065, May 1986.

Pauley, L. L., Moin, P., and Reynolds, W. C., "A Numerical Study of Unsteady Laminar Boundary Layer Separation," Report No. TF-34, Department of Mechanical Engineering, Stanford University, Stanford, CA, 1988.

Pauley, L. L., Moin, P., and Reynolds, W. C., "On the Structure of Two- and Three-Dimensional Separation," AIAA Paper No. 89-0287, January, 1989.

Pucher, P., and Göhl, R., "Experimental Investigation of Boundary Layer Separation With Heated Thin-Film Sensors," *Journal of Turbomachinery*, Vol. 109, April 1987, pp. 303-309.

Roberts, W. B., "Calculation of Laminar Separation Bubbles and Their Effect on Airfoil Performance," *AIAA Journal*, Vol. 18, No. 1, January 1980, pp. 25-31.

Russell, J., "Length and Bursting of Separation Bubbles: a Physical Interpretation," NASA CP-2085, Part I, 1978, pp. 177-201.

Schlichting, H., *Boundary Layer Theory*, 7th edition, McGraw-Hill, New York, 1979.

Schmidt, G. S., and Mueller, T. J., "Analysis of Low Reynolds Number Separation Bubbles Using Semiempirical Methods," *AIAA Journal*, Vol. 27, No. 8, August 1989, pp. 993-1001.

Selig, M. S., private communication, 1990.

Smith, A. M. O., and Gamberoni, N., "Transition, Pressure Gradient, and Stability Theory," Douglas Aircraft Co. Report ES 26338, 1956.

Squire, H. B. and Young, A. D., "The Calculation of the Profile Drag of Aerofoils," Aeronautical Research Council R & M 1838, 1937.

Stewartson, K., "Further Solutions of the Falkner-Skan Equation," *Proceedings of the Cambridge Philosophical Society*, vol. 50, 1954, pp. 454-465.

Stock, H. W., and Degenhart, E., "A Simplified e^n Method for Transition Prediction in Two-Dimensional, Incompressible Boundary Layers," to be published in Z. Flugwiss, Weltraumforsch.

Swafford, T. W., "Analytical Approximation of Two-Dimensional Separated Turbulent Boundary-Layer Velocity Profiles," *AIAA Journal*, Vol. 21, No. 6, June 1983, pp. 923-926.

Tani, I., "Low-Speed Flows Involving Bubble Separations," *Progress in Aeronautical Sciences*, Vol. 5, 1964, pp. 70-103.

Thwaites, B., "Approximate Calculation of the Laminar Boundary Layer," *Aeronautical Quarterly*, Vol. 1, 1949, pp. 245-280.

Vincent de Paul, M., "Prevision du Decrochage d'un Profil d'Aile en Ecoulement Incompressible," AGARD Conference Proceedings No. 102.

Von Doenhoff, A. E., "A Preliminary Investigation of Boundary-Layer Transition Along a Flat Plate with Adverse Pressure Gradient," NACA Technical Note No. 693, 1938.

Walker, G. J., "Modeling of Transitional Flow in Laminar Separation Bubbles," Ninth International Symposium on Air Breathing Engines, Athens, Greece, Sept. 3-8, 1989.

Wallis, R. A., "Boundary Layer Transition at the Leading Edge of Thin Wings and Its Effect on General Nose Separation," *Advances in Aeronautical Sciences*, Vol. 3, 1962, pp. 161-184.

Ward, J. W., "The Behaviour and Effects of Laminar Separation Bubbles on Aerofoils in Incompressible Flow," *Journal of the Royal Aeronautical Society*, Vol. 67, December 1963, pp. 783-790.

Whitfield, D. L., "Analytical Description of the Complete Turbulent Boundary-Layer Velocity Profile," *AIAA Journal*, Vol. 17, October 1979, pp. 1145-1147.

Wortmann, F. X., "Uber den Ablosewinkel laminarer Abloseblasen," Deutsche Luft- und Raumfarht Forschungsbericht 74-62, 1974.